MASTER

Modelling the light distribution in tissue phantoms for photodynamic therapy

Moes, C.J.M.

Award date:
1988

University of Technology
Eindhoven, The Netherlands.

Technische Universiteit Eindhoven
Faculteit der Technische Natuurkunde
Vakgroep: Analyse van Fysische Meetmethoden

MODELLING THE LIGHT DISTRIBUTION IN TISSUE PHANTOMS FOR PHOTODYNAMIC THERAPY.

C.J.M. Moes.

Afstudeerwerk verricht aan het Sint Joseph Ziekenhuis te Eindhoven.

datum:	maart 1988
afstudeerdocent:	Prof.dr. J.A. Poulis
kontaktpersoon:	dr.ir. C.H. Massen
begeleider St. Joseph ziekenhuis:	dr.ir. M.J.C. van Gemert

Laser . . . inter eximia naturae dona numeratum
plurimis compositionibus inseritur
The Laser is numbered among the most miraculous gifts
of nature and lends itself to a variety of applications
Plinius, *Naturalis Historia*, *XXII*, 49 (*1st century A.D.*)

An Elaboration of the Quotation from Pliny the Elder: The Laser during the Graeco-Roman Civilization

During the Graeco-Roman civilization (roughly from the 6th century B.C. to the 2nd century A.D.) the Laser was well known and much celebrated. It was in fact a plant (perhaps belonging to the *Umbelliferae*) which grew wild over a large area around Cyrene (in present-day Libya). Sometimes also called *Laserpitium*, it was considered to be a gift of God due to its almost miraculous properties. It was used to cure a variety of diseases, from pleurisy to various epidemic infections. It was an effective antidote against the poison of snakes, scorpions, and enemy arrows. Its delicate flavor led to its use as an exquisite dressing in the best cuisine. It was so valuable as to be the main source of Cyrenaean prosperity and it was exported to both Greeks and Romans. During the period of Roman domination, it was the only tribute paid by the Cyrenaeans to the Romans, who kept the Laser in their coffers together with their golden ingots. What is perhaps the best testimony to the Laser of those days is to be found on the celebrated Arcesilao cup (now in the Cyrene Museum), where porters can be seen loading the Laser onto a ship under the supervision of King Arcesilao. Both Greeks and Romans tried hard, but without success, to grow the Laser in various parts of *Apulia* and *Ionia* (in the south of Italy). Consequently the Laser became more and more rare and seems to have disappeared around the 2nd century A.D. Ever since then, despite several efforts, no one has been able to find the Laser in the deserts south of Cyrene, and so it remains the lost treasure of the Graeco-Roman civilization.

From O.Svelto, Principles of lasers
Plenum Press, New York, 1982 .

ACKNOWLEDGEMENT.

After a year of research I want to thank many people for their support.

First of all I like to thank Dr.ir. Martin J.C. van Gemert for his help during last year. Also I would like to thank Prof. Poulis for advising me several times during this period. Further I would like to thank Robert Splinter, Dick Sterenborg and Saskia Bosman for the many discussions we had and for their valuable advises, Jolanda de Klein and Henriette v.d. Griendt for the many, many papers and publications they had to look for, and very much I would like to thank Rian Becker, who spent much time in typing this report.
And last but not least I would like to thank Caroline Schellekens for her help during many, many moments of doubts.

CONTENTS

SAMENVATTING.

In het laatste decennium kunnen we een sterke groei in het gebruik van lasers voor medische doeleinden waarnemen. De optica van het gedrag van licht in weefsel is echter nog in ontwikkeling; een vergelijking tussen de theorie van de lichtverdeling in verstrooiende en absorberende media is daarom noodzakelijk.

Voor dit doel is het van belang de beschikking te hebben over goed-gedefinieerde verstrooiende en absorberende stoffen (fantomen).

Ook is het belangrijk inzicht te hebben in de indringdiepte van het licht in het medium, en in de mogelijkheid de indringdiepte te vergroten; dit is vooral van belang bij de behandeling van tumoren m.b.v. lasers.

In hoofdstuk I zullen we een overzicht geven van de optica van verstrooiende en absorberende media en van de resulterende lichtverdelingen in het medium voor verschillende lichtbronnen.

In hoofdstuk II zullen we de optische parameters van de verstrooiende stof Intralipid 10%, en van de absorberende stof Evans Blue onderzoeken, en vergelijken met de resultaten van andere onderzoekers. De uiteindelijke resultaten zijn gegeven in par. II.5.

In hoofdstuk III zullen we de mogelijkheid onderzoeken om de indringdiepte van licht in hersenweefsel te vergroten door het gebruik van een spiegel-systeem. Metingen werden verricht in verstrooiende en absorberende media, welke onderzocht werden in hoofdstuk II. Het blijkt dat bij gebruik van een spiegel-systeem de indringdiepte van het licht in het medium niet wezenlijk wordt vergroot.

In hoofdstuk IV zullen we de invloed van de bundeldiameter op de indringdiepte van het licht in het medium onderzoeken, waarbij experimentele resultaten vergeleken zullen worden met een theoretische oplossing. Het blijkt dat er goede overeenkomst bestaat tussen theorie en experiment, en dat de invloed van de bundeldiameter op de indringdiepte van het licht aanzienlijk is. Tevens is het mogelijk met deze resultaten de lichtverdeling tengevolge van het spiegel-systeem, zoals beschreven in het vorige hoofdstuk, te verklaren.

Tenslotte zullen we in hoofdstuk V een voorstel presenteren om de optische parameters van weefsel invasief te bepalen.

SUMMARY.

During the last decennium we can notice a strong expansion in the use of lasers for medical applications. The optics of the interaction of light tissue, however, is still under development; a comparison between the theory of light propagation in scattering and absorbing media and experimental results is therefore necessary.

For this purpose it is important to have the availability of well-defined scattering and absorbing substances (phantoms). It is also important to have knowledge about the penetration depth of light inside the tissue, and about possibilities to increase this penetration depth; this is particularly important in the treatment of cancer by laser light.

In chapter I we will present an overview of the optics of scattering and absorbing media and the solutions for several light source geometries.

In chapter II we will investigate the optical parameters of the scattering substance Intralipid 10%, and absorbing substance Evans Blue, and compare them with the results found by other investigators.

The final results are given in par. II.5.

In chapter III we will present an attempt to increase the penetration depth of light in brain tissue by using a mirror system. Measurements were carried out in a phantom using the well-defined substances described in ch. II.

It appears that the mirror system does not substantially increase the penetration depth of the light.

In chapter IV we will investigate the influence of the beam diameter on the penetration depth of the light inside the medium, and the experimental results will be compared with a theoretical solution. It appears that there is good agreement between theory and experiment, and that the influence of the beam diameter on the penetration depth is substantial.

Also it is possible with these results to explain the observed behaviour of the light shown in the previous chapter.

Finally we will present in chapter V a proposal to determine the optical parameters in tissue under in vivo conditions.

0 Introduction

Photodynamic therapy (PDT) is an experimental method for treating tumours by means of laser light and a photosensitizer. The basic concept of PDT is injecting the patient with a photosensitizer, e.g. Haematoporphyrin derivative (HpD) which has the property that it has a greater affinity for tumour tissue than for normal tissue, [Profio, 1984 and Bown, 1986].
Some time after administration the concentration of HpD in tumour tissue will be greater than in normal tissue [Profio, 1984 and Berns, 1983].
Exposing this tumour tissue to laser light with a wavelength matched to an absorption peak of HpD (e.g. 630 nm) and on condition that the light-dose exceeds a threshold value, this induces a photochemical reaction with a toxic product, singlet oxygen. As a result the affected tumour cells will die [Berns, 1983 and Weishaupt, 1976].
In this way, photodynamic therapy is a very efficient and selective method for cancer treatment.

One of the problems, however, which occur in this therapy is the prediction of the light distribution in the tissue. Knowledge of this light distribution is important because it is necessary for the light to penetrate deep enough to kill all tumour cells. If not, the non-damaged tumour cells will grow again [see fig. 0.1).

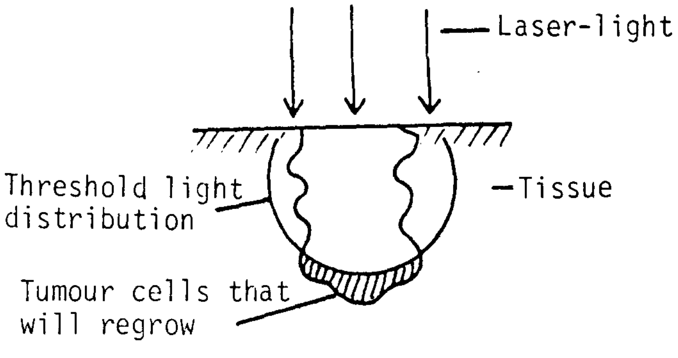

Fig. 0.1

The light distribution in tissue depends on several factors, such as absorption, and the angular distribution of scattering in the tissue, which in turn depend on the density of the particles, their shape and size relative to the wavelength, the index of refraction of the tissue etc.

To describe multiple-scattering and absorption of light in a turbid medium the main theory is: the transport theory [Ishimaru, 1978]. This theory is based on the "equation of radiative transport", an integro-differential equation which uses the medium parameters, such as the absorption coefficient μ_a, scattering coefficient μ_s and scattering phase function $S(\cos\theta)$.
Together with boundary condition this equation describes the light distribution in a scattering and absorbing medium.

This report falls into four parts.
In chapter 1 the transport theory will be presented as well as the solutions for three different light source geometries, based on the work of several authors. These solutions will be used lateron for a comparison with experimental results.
In chapter 2 a method will be presented to determine μ_a, μ_s and g using a scattering and absorbing tissue phantom. The experimental values will be compared with the values found by other authors.
In chapter 3 an attempt will be presented to improve the penetration depth of light in a brain tissue phantom. This part was presented at the Symposium of the N.M.L.G. (Nederlands Medisch Laser Genootschap) Rotterdam, The Netherlands, at the Daniel den Hoedkliniek, September 1987.
In chapter 4 the influence of the beam diameter on the penetration depth will be investigated.
Experimental values will be compared with theoretical results.

In chapter 5 we will present a proposal for a (semi-)invasive in-vivo determination of the optical parameters.

The work was done in a research project for the St. Joseph Hospital in Eindhoven, the Netherlands under supervision of Dr. M.J.C. van Gemert as a graduation project for the Eindhoven University of Technology, the Netherlands, under supervision of Prof. Dr. J.A. Poulis.

I. Theory.

I.1 Introduction.

The main theory to describe the propagation of light in a turbid medium is the transport theory, which is based on the "equation of radiative transport", [Ishimaru, 1987], an integro-differential equation. Together with boundary conditions this equation can be solved in principle, if scattering and absorption properties of the medium are known. In the case that scattering dominates over absorption, however, which is true in all cases discussed in this report, this "equation of transport" can be treated in the so called diffusion approximation, which is much more easy to handle.

In this chapter the theory will be presented only briefly; a more detailed version can be found in appendix B.

I.2.1. Transport theory [Ishimaru, 1978].

To describe this theory, we will use the notation recommended by Star, Wilson, Jacques and van Gemert which can be found in Appendix A. Before proceeding, some assumptions will have to be made made, namely:

- the model is time independent
- the medium is homogeneous and isotropic
- the scattering particles are randomly distributed over the tissue volume
- the scattered photons retain their frequency
- there are no other sources but the incident beam
- the scattering particles are sufficiently far away that interference effects between phantoms can be neglected.

The transport theory is based on the "equation of transport":

$$(\hat{s}\cdot\nabla)L(\hat{r},\hat{s}) = -\mu_t L(\hat{r},\hat{s}) + \frac{\mu_t}{4\pi}\int_{4\pi} S(\hat{s}\cdot\hat{s}')L(r,s')dw' \qquad \text{(I.2.1)}$$

where

$L(\hat{r},\hat{s})$ = energy radiance in $\hat{r}$ in direction $\hat{s}$ ($Wm^{-2}sr^{-1}$)

μ_a = absorption coefficient (m^{-1})

μ_s = scattering coefficient (m^{-1})

μ_t = $\mu_a+\mu_s$ = total attenuation coefficient (m^{-1})

dw' = element of solid angle (sr)

$\cos\theta$ = $\hat{s}.\hat{s}'$ = cosine of the angle between $\hat{s}$ and $\hat{s}'$.

$S(\hat{s}.\hat{s}')$= phase function representing the part of the photon flux which is scattered from direction $\hat{s}'$ in direction $\hat{s}$ (sr^{-1}).

Because the scattering particles are randomly distributed, we may substitute $S(\hat{s}.\hat{s}')$ by $S(\cos\theta)$.

In eq. (I.2.1.) the left part is the net rate of change of L at $\hat{r}$ in the direction $\hat{s}$:

$$\frac{dL(\hat{r},\hat{s})}{ds} = (\hat{s}.\hat{\nabla})L(\hat{r},\hat{s}) \qquad (I.2.2)$$

This rate of change is due to losses by scattering and absorption, represented by the first term on the right side, and the gain through scattering from all directions $\hat{s}'$ into $\hat{s}$, represented by the second term on the right side.

The relation between the energy fluence rate $\Psi(Wm^{-2})$ and the energy radiance L is:

$$\Psi(\hat{r}) = \frac{1}{4\pi} \int_{4\pi} L(\hat{r},\hat{s})dw \qquad (I.2.3)$$

I.2.2. Phase functions.

Scattering of light in a medium is described not only by the scattering coefficient μ_s , but also by the "phase function" S(cosθ), which is the relative probability for scattering of a photon from direction $\hat{s}'$ into direction $\hat{s}$, where $\hat{s}'.\hat{s} = \cos\theta$.
Examples of phase functions are shown in fig. I.2.1.

The phase function S(cosθ) can be expanded as a series of Legendre polynomials $P_n(\cos\theta)$ [Davison, 1957 ch. 17]:

$$S(\cos\theta) = \sum_{n=0}^{\infty} \frac{(2n+1)}{2} b_n P_n(\cos\theta) \qquad (I.2.4)$$

Conversely, we obtain b_n from the fact that the functions P_n form a complete orthogonal set:

$$b_n = \int_{-1}^{1} S(\cos\theta)P_n(\cos\theta)d(\cos\theta) \tag{I.2.5}$$

Normalisation requires that the integral of $S(\cos\theta)$ over all directions equals 1, so

$$b_o = \int_{-1}^{1} S(\cos\theta)d(\cos\theta) = 1 \tag{I.2.6}$$

because $P_o = 1$, and because $P_1(\cos\theta) = \cos\theta$ we obtain for b_1:

$$b_1 = \int_{-1}^{1} S(\cos\theta)\ \cos\theta d(\cos\theta) = g \tag{I.2.7}$$

Thus b_1, usually referred to as g and called the asymmetry parameter [v.d. Hulst, 1980], is the mean cosine of the scattering angle.

However, there exist many phase functions describing the scattering of light in a medium [v.d. Hulst, 1980, vol. 2, p. 306-307].

Slightly forward scattering, for example, can be represented by the first two terms of the phase function, thus

$$S(\cos\theta) = a(1 + 3\ g\ \cos\theta)\ ,\ g \leq \frac{1}{3} \tag{I.2.8}$$

where $a = \mu_s / \mu_t$ is called the albedo.

Another phase function often used in light optics is the Henyey-Greenstein function:

$$S(\cos\theta) = a \cdot \frac{(1-g^2)}{(1+g^2-2g\cos\theta)^{3/2}} \qquad (I.2.9)$$

However, this phase function is not easy to handle, so we will adopt a simpler phase function, namely "isotropic scattering combined with a forward peak" [v.d. Hulst, 1980]:

$$S(\cos\theta) = a \ \ [(1-g)+2g\ \delta(1-\cos\theta)] \qquad (I.2.10)$$

According to v.d. Hulst all three phase functions are the same in the first two terms of their Legendre polynomial expansion.
A plot of these phase functions for several values of g is given in fig. I.2.1.

There are two possibilities to continue now; one way is to write both radiant energy L and phase function $S(\cos\theta)$ as a series of Legendre polynomials, insert them in eq. I.2.1 and truncate after the first two terms. This method is called the P_1-approximation and is e.g. described by [Star et al., 1987].

We will use another approach which is described by [Reynolds, 1975] and, [Groenhuis, 1983] and by [Prahl, 1986], using the phase function "isotropic scattering combined with forward peak". The reason is that with this approach it is possible to obtain an analytical solution. We have to realize, however, that this choice may affect the valid of the measured optical parameters, because an indirect method will be applied that utelises the inverse solution of the transport equation for a slab geometry. Substituting eq. (I.2.10) into eq. (I.2.1) we find after some calculations:

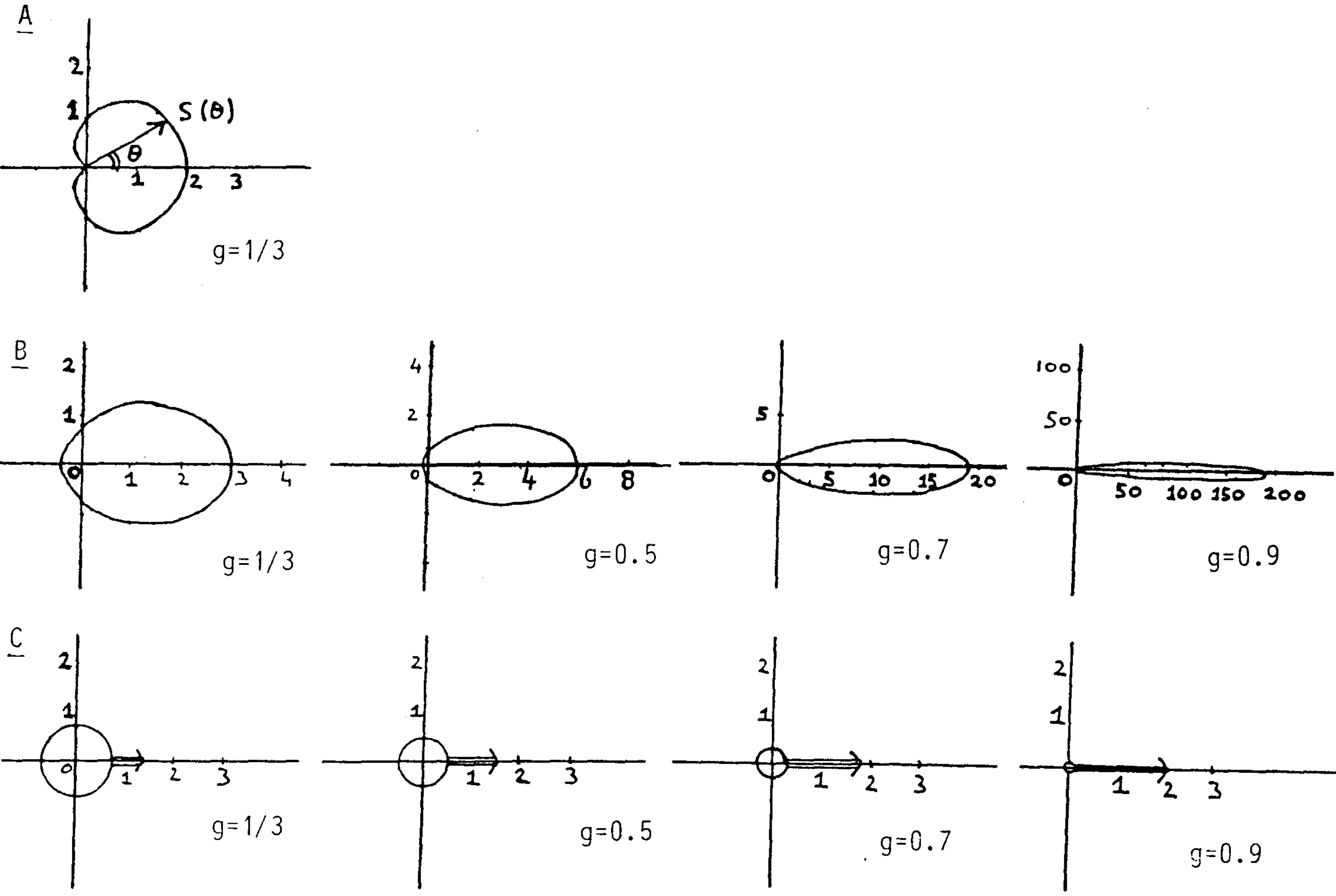

Fig. I.2.1: Pase functions for several values of g.

A: Slightly forward scattering (eq. I.2.8).

B: Henyey-Greenstein function (eq. I.2.9).

C: Isotropic scattering with forward peak (eq. I.2.10).

$$(\hat{s}.\hat{\nabla})L(\hat{r},\hat{s}) = -\mu_{tr}L(\hat{r},\hat{s}) + \frac{\mu_s'}{4\pi}\int_{4\pi} L(\hat{r},\hat{s}')dw' \qquad (I.2.11)$$

where

$\mu'_s = \mu_s(1-g)$ = reduced scattering coefficient

$\mu_{tr} = \mu_a + \mu'_s$ = transport coefficient

I.2.3 Diffusion approximation.

To describe the propagation of light in a scattering medium it is often convenient to devide the energy radiance $L(\hat{r},\hat{s})$ into two parts, the redcued incident or non-scattered energy radiance $L_{ri}(\hat{r},\hat{z})$ and the so called diffuse energy radiance $L_d(\hat{r},\hat{s})$ [Reynolds, 1975], [Groenhuis, 1983] and [Prahl, 1986], which is the part of the energy radiance that is scattered at least once. Thus,

$$L(\hat{r},\hat{s}) = L_{ri}(\hat{r},\hat{z}) + L_d(\hat{r},\hat{s}) \qquad (I.2.12)$$

$L_{ri}(\hat{r},\hat{z})$ has the same direction ($\hat{z}$) as the incident beam and contains the unscattered plus forward scattered beam. Substituting this eq. (I.2.12) into eq. (I.2.11) we find two equations, one for L_{ri} and one for L_d, see Appendix .

The diffuse energy fluence rate $\Psi_d(\hat{r})$ and the reduced incident energy fluence rate $\Psi_{ri}(\hat{r})$ are defined as

$$\Psi_d(\hat{r}) = \frac{1}{4\pi}\int_{4\pi} L_d dw \qquad (I.2.13a)$$

and

$$\Psi_{ri}(\hat{r}) = \frac{1}{4\pi}\int_{4\pi} L_{ri} dw \qquad (I.2.13b)$$

Expanding the diffuse energy radiance L_d in a Taylor series we find after some calculations (see appendix B) the so-called "time-independent diffusion equation":

$$(\nabla^2 - \mu^2_{eff}) \ \Psi_d = - \frac{\mu'_s}{D} \ \Psi_{ri} + \frac{3}{4\pi} \int_{4\pi} \varepsilon_{ri} \ \hat{s} \ dw \qquad (I.2.14)$$

where $\mu^2_{eff} = 3 \ \mu_a \mu_{tr}$ = effective attenuation coefficient

and $\varepsilon_{ri} = \frac{\mu'_s}{4\pi} \int_{4\pi} L_{ri} \ dw'$

$D = (3 \ \mu_{tr})^{-1}$ = diffusion constant

If the parameters characterising the incident beam are defined, together with boundary conditions this equation can be solved in principle.

A few words have to be said about the definition of the reduced incident radiant energy $L_{ri}(\hat{r},\hat{z})$. According to Ishimaru (1978) and Van Gemert (1987), L_{ri} contains only the unscattered beam and therefore they receive a different "diffusion equation". Here we define L_{ri} as the unscattered + forward scattered beam, in agreement with Groenhuis (1983), Prahl (1986), because it is in practice not possible to distinguish between the unscattered and the purely forward scattered beam. The final result, which is the sum of the diffuse and the collimated parts, must of course be the same.

I.2.4 Boundary conditions.

The boundary conditions are determined by the tissue geometry; for a slab geometry they will have another form than for a spherical geometry. We will assume a slab geometry.

To derive the boundary conditions, consider the situation shown in fig I.2.2.

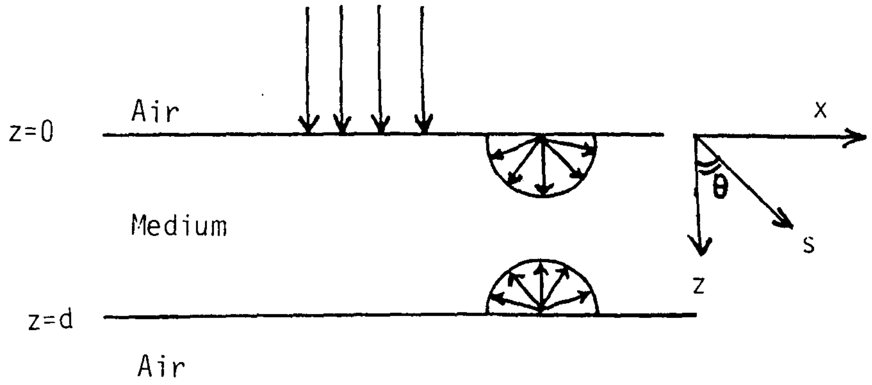

Fig. I.2.2. Model for diffuse reflection at the boundaries.

The boundary condition here is that the total diffuse flux directed inward the medium is equal to the reflected part of the total flux directed outward; thus if we define

$$\mu = \hat{s}.\hat{z} = \cos\theta$$

we find

$$\text{at } z=0 \int_{\substack{2\pi \\ \mu>0}} I_d(\hat{r},\hat{s})(\hat{s}.\hat{z})dw = \int_{\substack{2\pi \\ \mu<0}} r_d(\theta)I_d(\hat{r},\hat{s})(\hat{s}.\hat{z})dw \qquad \text{(I.2.15a)}$$

$$\text{at } z=d \int_{\substack{2\pi \\ \mu<0}} I_d(\hat{r},\hat{s})(\hat{s}.\hat{z})dw = \int_{\substack{2\pi \\ \mu>0}} r_d(\theta)I_d(\hat{r},\hat{s})(\hat{s}.\hat{z})dw \qquad \text{(I.2.15b)}$$

where $r_d(\theta)$ is the internal reflection coefficient for diffuse radiation; For convenience r_d is supposed to be constant; Later on we will correct for angle-dependance of r_d.

Again we devide the energy radiance $L(\hat{r},\hat{s})$ into two parts (eq. I.2.12), the reduced incident energy radiance $L_{ri}(\hat{r},\hat{z})$ and the diffuse energy radiance $L_d(\hat{r},\hat{s})$, and we define the diffuse energy fluence rate $\Psi_d(\hat{r})$ as (eq. I.2.13a).

$$\Psi_d(\hat{r}) = \frac{1}{4\pi} \int_{4\pi} L_d(\hat{r},\hat{s})dw \qquad \text{(I.2.13a)}$$

After some calculations Groenhuis [1983] arrived at the following boundary conditions for the slab geometry:

$$\text{at } z=0 \quad \Psi_d(\hat{r})-2Dh\frac{\partial}{\partial z}\Psi_d(\hat{r}) + \frac{1}{2\pi} h\,\hat{z}.\,Q(\hat{r}) = 0 \qquad \text{(I.2.16a)}$$

$$\text{at } z=d \quad \Psi_d(\hat{r})+2Dh\frac{\partial}{\partial z}\Psi_d(\hat{r}) + \frac{1}{2\pi} h\,\hat{z}.\,Q(\hat{r}) = 0 \qquad \text{(I.2.16b)}$$

$$\text{where } D = (3\mu_{tr})^{-1} \qquad \text{(I.2.17)}$$

$$h = (1+r_d)/(1-r_d) \qquad \text{(I.2.18)}$$

$$Q(r) = \frac{1}{\mu_{tr}} \int_{4\pi} \varepsilon_{ri}\,\hat{s}\,dw \qquad \text{(I.2.19)}$$

$$\varepsilon_{ri} = \frac{\mu'_s}{4\pi} \int_{4\pi} I_{ri}\,dw' \qquad \text{(I.2.20)}$$

These are the boundary conditions used by Groenhuis (1983), Reynolds (1975) and Prahl (1986). The internal reflection coefficient for diffuse radiation can be estimated using a curve fit proposed by Egan and Hilgeman [Egan and Hilgeman, 1979]:

$$r_d \simeq -1.4399\ n^{-2} + 0.7099\ n^{-1} + 0.6681 + 0.0636\ n$$

where n is the index of refraction of the medium.

In the derivation described above, the internal reflection coefficient r_d is assumed to be a constant. However, in a real situation the reflection coefficient r_d is angle-dependant; thus actually we have to consider the situation shown in fig. I.2.3.

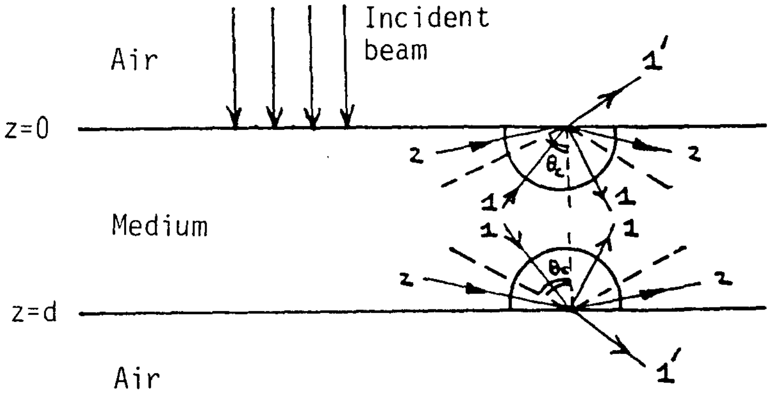

Fig. I.2.3. **Model for diffuse reflection at the boundaries including total reflection. θ_c is critical angle.**

Light which reaches the surface under an angle smaller than the critical angle for total reflection, thus $\theta<\theta_c$, is partly reflected and partly transmitted (beam 1). If, however, the angle is greater than θ_c, all the light is totally reflected.

The internal reflection coefficient r_d is related to the angle θ by Fresnel's laws:

$$r_d = \tfrac{1}{2}[R_{\parallel}^2 + R_{\perp}^2] \tag{I.2.21}$$

where

$$R_{\parallel} = \frac{n_{med} \cos\theta_{air} - n_{air} \cos\theta_{med}}{n_{med} \cos\theta_{air} + n_{air} \cos\theta_{med}} \tag{I.2.21a}$$

$$R_{\perp} = \frac{n_{med} \cos\theta_{med} - n_{air} \cos\theta_{air}}{n_{med} \cos\theta_{med} + n_{air} \cos\theta_{air}} \tag{I.2.21b}$$

The critical angle θ_c is determined by Snell's Law:

$$n_{med} \operatorname{Sin}\theta_{med} = n_{air} \operatorname{Sin}\theta_{air} \tag{I.2.22}$$

A plot of r_d as a function of θ is given in fig. I.2.4.

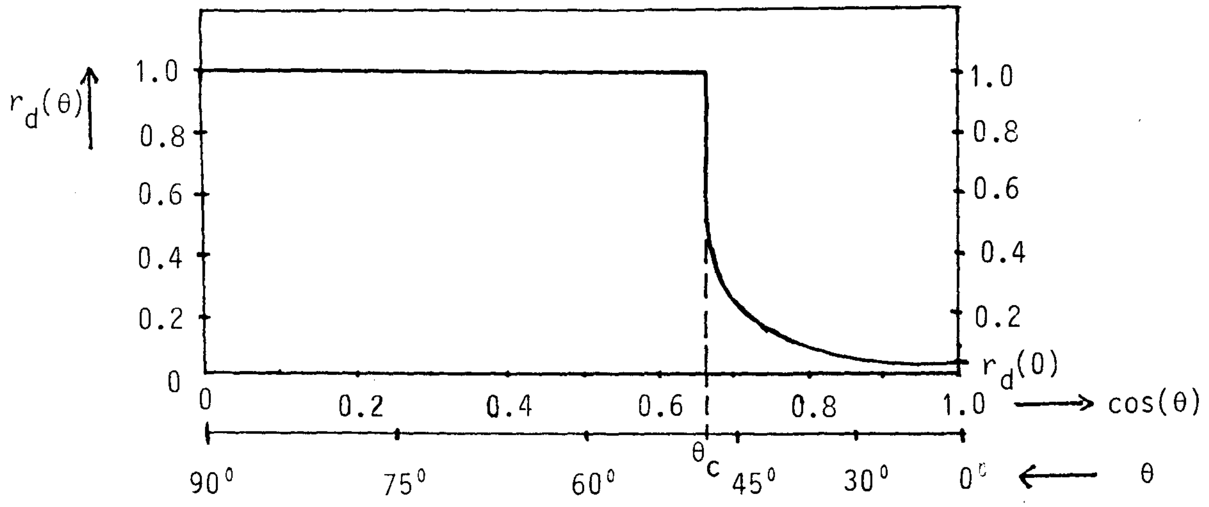

Fig. I.2.4. **Internal reflection coefficient $r_d(\theta)$ as a function of θ, based of eq. (I.2.21) and eq. (I.2.22).**

When $\theta = 0$, the reflection coefficient $r_d(0)$ is

$$r_d(0) = \frac{(n_{med} - n_{air})^2}{(n_{med} + n_{air})^2} \qquad (I.2.23)$$

This angle dependance of the internal reflection coefficient r_d has to be raken into account in eq. I.2.15.

This has been done by [M. Keyzer, 1986] and the result is (see also Appendix):

$$\text{at } z=0 \quad \Psi_d(\hat{r})-2DA\frac{\partial}{\partial z}\Psi_d(\hat{r}) + \frac{1}{2\pi}A\hat{z}.Q(\hat{r})=0 \qquad (I.2.24a)$$

$$\text{at } z=d \quad \Psi_d(\hat{r})+2DA\frac{\partial}{\partial z}\Psi_d(\hat{r}) + \frac{1}{2\pi}A\hat{z}.Q(\hat{r})=0 \qquad (I.2.24b)$$

where $D = (3\ \mu_{tr})^{-1}$

$$A = \left[\frac{2/[1-r_d(o)]-1+|\cos^3\theta_c|}{1-\cos^2\theta_c}\right] \qquad (I.2.25)$$

and $Q(\hat{r})$ is defined in eq. (I.2.19).

When we compare eq. I.2.24 with eq. I.2.16 we can see the strong resemblance between them, except that h has to be substituted by A.

We can make a plot of h and A versus the index of refraction n, shown in fig. I.2.5.

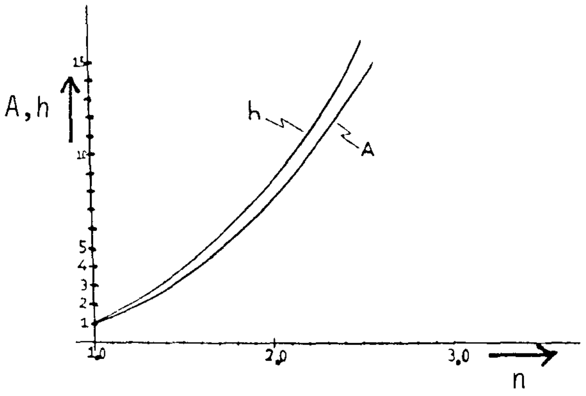

Fig. I.2.5: Values of h and A versus the index of refraction n.

For the indices of refraction of interest for photodynamic therapy ($1.48 < n_{white\ skin} < 1.52$) [Bruls, 1984] we find a difference between h and A of about 15%. It is not clear, however, how strong this difference affects the light distribution predictions.

I.3 Wide beam solution (see Ishimaru, p. 182).

Consider a parallel beam of monochromatic light with infinite diameter incident on a plane parallel scattering and absorbing medium. This beam can be described by:

$$L_{inc}(\hat{r},\hat{s}) = F_o \ \delta\ (\hat{s}-\hat{z}) \qquad (I.3.1)$$

where F_0 is a constant.

When the indices of refraction are different, F_o has to be multiplied by $1-[n_{med}-1)^2/(n_{med}+1)^2]$.

When we substitute eq. (I.3.1) in the diffusion equation, we find according to Ishimaru, p. 182:

$$\frac{\partial^2}{\partial z^2} \Psi_d(z) - \mu^2_{eff} \Psi_d(z) = - Q_o \exp(-\mu_t z) \qquad (I.3.2)$$

where $Q_o = [3\mu_s\mu_{tr} + 3g\mu_s\mu_t](F_o/4\pi)$

$\mu^2_{eff} = 3\mu_a\mu_{tr}$

$\mu_{tr} = \mu_a + (1-g)\mu_s$

The general solution of eq. (I.3.2) is the sum of a particular solution Ψ_{dp} and a complementary solution Ψ_{dc}.

For the particular solution we take

$$\Psi_{dp} = C_o \exp(-\mu_t z) \tag{I.3.3}$$

and for the complementary solution

$$\Psi_{dc} = C_1 \exp(+\mu_{eff} z) + C_2 \exp(-\mu_{eff} z) \tag{I.3.4}$$

Thus the general solution is:

$$\Psi_d(z) = C_1 \exp(+\mu_{eff} z) + C_2 \exp(-\mu_{eff} z) + C_o \exp(-\mu_t z) \tag{I.3.5}$$

The constants C_o C_1 and C_2 are determined by the boundary conditions. For a thin slab of medium all three terms are important [Star, 1986]. For a thick slab it can be shown that $C_1 \to 0$, [Ishimaru, 1978] and [Star, 1986]; thus the solution becomes:

$$\Psi_d(z) = C_o \exp(-\mu_t z) + C_2 \exp(-\mu_{eff} z) \tag{I.3.6}$$

where $\mu_t = \mu_a + \mu_s$

$\mu_{eff} = [3 \mu_a \mu_{tr}]^{\frac{1}{2}}$

Looking at the ratio of μ_{eff} and μ_t we find:

$$\frac{\mu_{eff}}{\mu_t} = [3(1-a)(1-ag)]^{\frac{1}{2}}$$

where $a = \mu_s / \mu_t$ = albedo

In the case that scattering dominates over absorption, thus a → 1 we find

$$\mu_{eff} \ll \mu t \qquad \text{if } a \to 1 \tag{I.3.8}$$

Returning to Eq. (I.3.6) we see both terms are important at the boundary, but deep inside only the last term differs from zero, and we find that deep inside the medium:

$$\Psi_d(z) = C_2 \exp(-\mu_{eff} z) \qquad \text{if } a \to 1 \ , \ z \gg \mu^{-1}_t \tag{I.3.9}$$

This situation occurs already beyond a depth of a few free optical path lengths μ_t^{-1} [Star, 1987].

The general light pattern inside the medium as a function of depth z will be like that shown in fig. I.3.1.

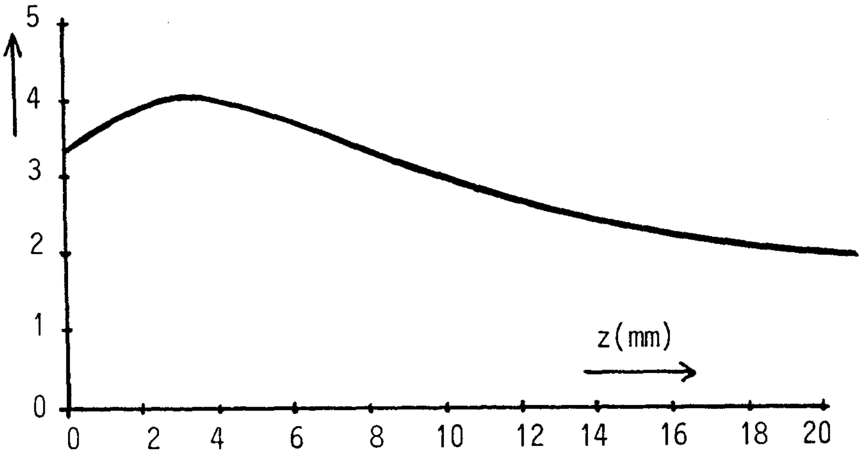

Fig. I.3.1: General light pattern inside the medium for an incident wide beam, with parameters μ_s = 1mm^{-1}, g = 0.7, μ_a = 1.3x10^{-10} mm^{-1}.

The position and value of the maximum of the curve depends on the boundary conditions.

I.4. Finite diameter solution.

In this paragraph we will discuss the solution for a beam with a finite diameter incident on a medium. Details of this derivation can be found in appendix B ; here we will give only a brief overview. The derivation is based on Reynolds [1975], Ishimaru [1978] and Prahl [1986].

Consider a parallel beam of monochromatic light with a finite diameter incident on a plane parallel scattering and absorbing medium. This beam can be described by:

$$L_{inc}(\hat{r},\hat{s}) = F_o B(r)\delta\,(\hat{s}-\hat{z}) \qquad (I.4.1)$$

where F_o is a constant

B(r) is the radial distribution of the incident light beam; here we assume:

$B(r) = 1$ if $0 \leq r \leq b$

$= 0$ if $r > b$

Substituting this incident beam in the diffusion equation (I.2.14) we find:

$$(\nabla^2 - \frac{\mu_a}{D})\,\Psi_d = \frac{\mu_s'}{4D}\,F_o B(r)\exp(-\,\mu_{tr}z) \qquad (I.4.2)$$

with boundary conditions (see ch. I.2.4)

$$\text{at } z = 0 \quad \Psi_d(\hat{r}) - 2DA\frac{\partial}{\partial z}\Psi_d(\hat{r}) = 0 \qquad (I.4.3a)$$

$$\text{at } z = d \quad \Psi_d(\hat{r}) + 2DA\frac{\partial}{\partial z}\Psi_d(\hat{r}) = 0 \qquad (I.4.3b)$$

Today these differential equations can be solved numerically; solutions are available from e.g. Keyzer [1986]. The differential equation (I.4.2) can also be solved analytically by using a Greens function approach; the latter function $G(\hat{r};\hat{r}')$ has to be a solution of the equation:

$$(\nabla^2 - \frac{\mu_a}{D})G(\hat{r};\hat{r}') = \delta\,(\hat{r};\hat{r}') \qquad (I.4.4)$$

with boundary conditions:

$$\text{at } z=0 \qquad G(\hat{r};\hat{r}') - 2DA\frac{\partial}{\partial z}G(\hat{r};\hat{r}') = 0 \qquad (I.4.5a)$$

$$\text{at } z=d \qquad G(\hat{r};\hat{r}') + 2DA\frac{\partial}{\partial z}G(\hat{R};\hat{r}') = 0 \qquad (I.4.5b)$$

The solution of this equation is (see appendix B):

$$\Psi d(r,z) = \frac{4\mu'_s}{D} F_o \sum_{n=1}^{\infty} \Gamma_n \sin(k_n z + \gamma_n) \frac{Z_n}{(k_n^2+\mu_{tr}^2)} R_n(\lambda_n r) \qquad (I.4.6)$$

where

$$\tan k_n d = \frac{2(DA)k_n}{(DA)^2 k_n^2 -1}$$

$$\gamma_n = \tan^{-1}(DAk_n)$$

$$\lambda_n^2 = k_n^2 + \frac{\mu_a}{D}$$

$$R_n(\lambda_n r) = \begin{cases} 1/\lambda_n^2\,[1-\lambda_n b I_o(\lambda_n r)K_1(\lambda_n b)] & r < b \\ b/\lambda_n\,[K_o(\lambda_n r)I_1(\lambda_n b)] & r > b \end{cases}$$

$I_n(\lambda_n r)$ and $K_n(\lambda_n r)$ are modified Bessel functions of the first kind of order n. Based on this solution a computer-programme is available [S.Prahl, 1986].

I.5 Point source solution.

To discuss the solution for a point source we have to distinguish between the situation that the point source is put directly inside the medium and the situation that the point source is put inside a sphere filled with water or a scattering medium. Both solutions will be discussed below.

I.5.1 Point source in an infinite medium.

Consider a point source placed inside an infinite medium. There is no external light source, thus $L_{inc} = 0$.

The point source can be expressed by [Ishimaru, 1978]:

$$\varepsilon\ (\hat{r},\hat{s}) = (P_o/4\ \pi)\ \delta(\hat{r}) \qquad (I.5.1)$$

and the diffusion equation becomes:

$$(\nabla^2 - \mu^2_{eff})\ \Psi_d(\hat{r}) = -(\frac{3}{4}\pi)\mu_{tr}P_o\ \delta(\hat{r}) \qquad (I.5.2)$$

The solution of this equation is [Ishimaru, 1978]

$$\Psi_d(\hat{r}) = (\frac{3}{4\pi}\ \mu_{tr}P_o)\ \frac{1}{4\pi\ r}\ \exp(-\ \mu_{eff}r) \qquad (I.5.3)$$

where P_o is the power of the point source.
and $\mu_{eff} = 3(\mu_a\mu_{tr})^{-1}$

This equation has also been used by Star [Star, 1986].

We like to remark already here that this solution is not valid near the point source itself, because there the diffusion approximation is not valid. Only at a distance of a few times μ^{-1}_t the equation (I.5.3) is valid.
The general light pattern inside the medium as a function of the radius r will be like that shown in fig. I.5.1.

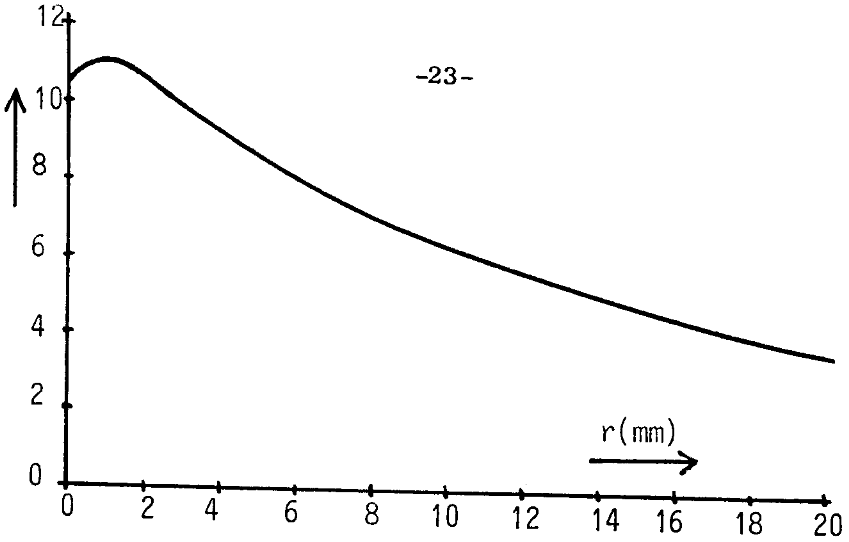

Fig. I.5.1: General light pattern inside the medium for a point source.

I.5.2 Point source inside a sphere.

Consider now a point source which is placed inside a sphere filled with air or clear water and placed in an infinite medium with absorbing and scattering properties (see fig. I.5.1).

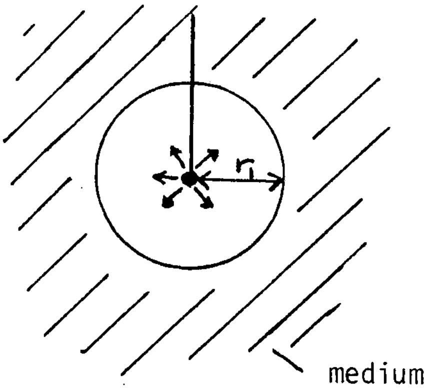

Fig. I.5.2: Point source inside a balloon with radius r_1, placed in an infinite medium.

A solution for this situation is available from Star [Star, 1986], and we find:

$$\Psi(r) = \frac{3}{4\pi}\left[\frac{\mu_{tr}\exp(-\mu_{eff}(r-r_1))}{(1+\mu_{eff}r_1)r} - \frac{2}{3}\,\frac{\exp-(\mu_t(r-r_1))}{r^2}\right] \qquad (I.5.4)$$

Note that light which is scattered out of the medium into the sphere re-enters the medium elsewhere. Because $\mu_{eff} \ll \mu_t$ (see eq. I.3.8), deep inside the medium only the first term remains.

II. Phantom materials.

II.1 Introduction.

In this chapter we will concentrate on determination of the optical properties of the media we have used. For this purpose part of the theory of the previous chapter will be used. Because biological tissues are often very irregular and inhomogeneous, we have chosen for a liquid tissue phantom which exists of a mixture of a purely absorbing medium and a scattering medium. Recent developments in the measurement of optical constants of biological tissues indicate that tissue scatters light strongly in the forward direction [Star, 1986]; therefore it is important to use a scattering medium which has also strongly forward scattering properties.

II.2 Intralipid and Evans Blue.

In search of a good phantom material one of the problems is to find a scattering medium which has the combination of, highly forward scattering, no absorption, availability and which can serve as an international standard. A first choice was styrene butadiene, but it appeared that its g-value was rather low ($g \simeq 0.4$), the availability was bad and that the material was not homogeneous [Splinter, 1987]. Therefore we have chosen for Intralipid (10%), which is very well available in every hospital, has highly forward scattering properties and low absorption, and is rather homogeneous (see chapter II.3).

As an absorber we used Evans Blue, dissolved in an isotonic phosphate buffer. The concentration was 515 mg/l.

II.3 Determination of optical parameters.

II.3.1 Homogeneity of Intralipid.

To examine for the homogeneity of Intralipid, the size of the particles was measured at the department of colloid chemistry at the Eindhoven University of Technology. The results are presented in figs. II.3.1 to II.3.4.

In figs. II.3.1 and II.3.2 we see the results for normal Intralipid. From the statistical analysis we can see that both measurements give virtually the same result for the mean particle size, namely 1.004 μm and 1.030 μm. The coefficient of variation, which is the ratio of the standard deviation and the mean value, is resp. 13.6% and 17.7%.

In figs. II.3.3 and II.3.4 we see the results for boiled Intralipid (boiled for 30 seconds at $100^{o}C$ and steered Intralipid (at 20.000 cpm). We can see that for boiled water Intralipid the mean size of the particles becomes smaller (about 0.84 μm) whereas for steered Intralipid the mean size of the particles becomes greater (about 1.4 μm). The coefficient of variation in both cases is less then 20%.

From the results we concluded that the homogeneity of normal Intralipid seems adequate for our purposes. We must take into account, however, that boiling or steering Intralipid can change the size of the particles and thus change the scattering properties of the particles.

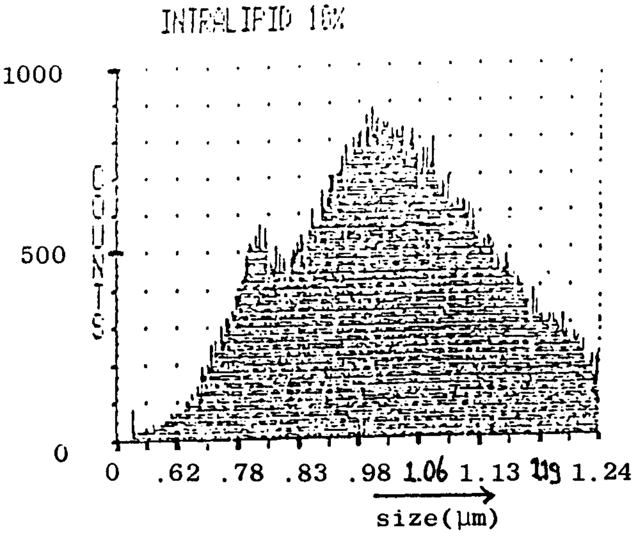

```
File: INTRALIPID 10%

                 Statistical analysis
                 ====================

          Calculation range: channel 1 to channel 256.
          Size scale: DIAMETER
           Weighting: None
          Calculations use the arithmetic mean.

          Mean size:    1.004 um
          Modal size:   1.001 um
          Median size:  1.021 um

          Variance:                 1.863E-2
          Standard deviation: 0.1365 um
          Coeff of variation: 13.59%

          Skewness: -0.6777
          Kurtosis: 0.4194

          Distribution is left-skewed and leptokurtic.

          Percentiles:
          ------------

             5   % above 1.201 um
            10   % above 1.170 um
            16   % above 1.141 um
            25   % above 1.105 um
            50   % above 1.021 um
            75   % above 0.9224 um
            84   % above 0.8601 um
            90   % above 0.8124 um
            95   % above 0.7593 um
```

Fig. II.3.1

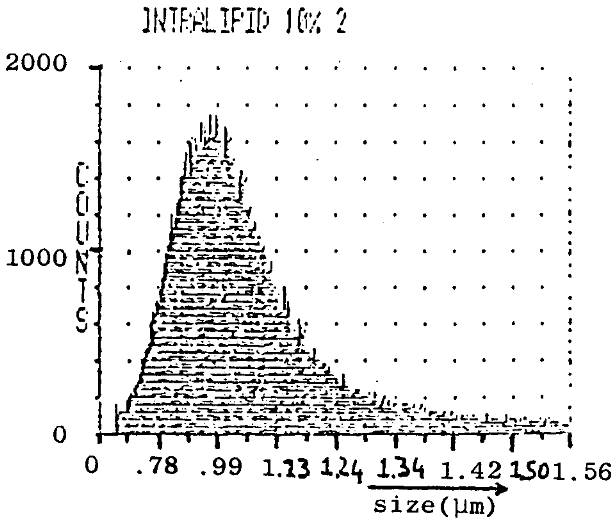

```
File: INTRALIPID 10% 2

                 Statistical analysis
                 ====================

          Calculation range: channel 1 to channel 256.
          Size scale: DIAMETER
           Weighting: None
          Calculations use the arithmetic mean.

          Mean size:    1.030 um
          Modal size:   0.9609 um
          Median size:  1.013 um

          Variance:                 3.306E-2
          Standard deviation: 0.1818 um
          Coeff of variation: 17.66%

          Skewness: 0.4312
          Kurtosis: 0.3800

          Distribution is right-skewed and leptokurtic.

          Percentiles:
          ------------

             5   % above 1.381 um
            10   % above 1.276 um
            16   % above 1.199 um
            25   % above 1.129 um
            50   % above 1.013 um
            75   % above 0.9105 um
            84   % above 0.8629 um
            90   % above 0.8187 um
            95   % above 0.7563 um
```

Fig. II.3.2

Measurement of the homogeneity of Intralipid from the St.Joseph Hospital; the vertical axis gives the relative amount of particles of a certain size, the horizontal gives the size of the particles in µm.

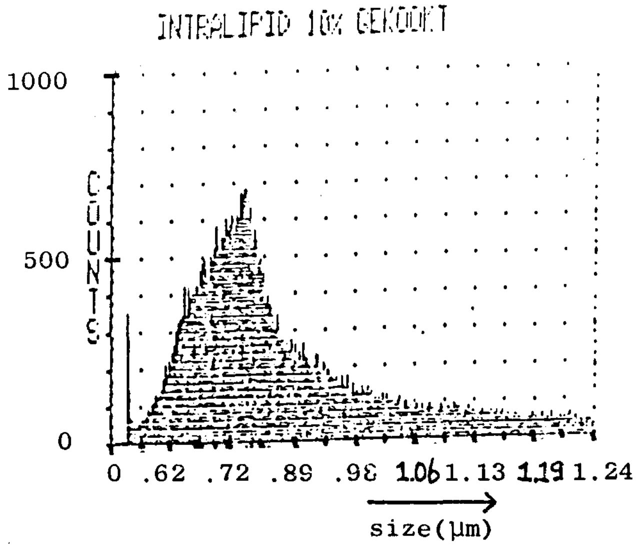

```
File: INTRALIPID 10% GEKOOKT

              Statistical analysis
              ====================

          Calculation range: channel 1 to channel 256.
          Size scale: DIAMETER
           Weighting: None
          Calculations use the arithmetic mean.

          Mean size:   0.8411 um
          Modal size:  0.8032 um
          Median size: 0.8170 um

          Variance:               2.687E-2
          Standard deviation: 0.1639 um
          Coeff of variation: 19.49%

          Skewness: 0.2615
          Kurtosis: 3.675E-2

          Distribution is right-skewed and leptokurtic.

          Percentiles:
          ------------

             5  % above 1.153 um
            10  % above 1.086 um
            16  % above 1.016 um
            25  % above 0.9396 um
            50  % above 0.8170 um
            75  % above 0.7371 um
            84  % above 0.6944 um
            90  % above 0.6563 um
            95  % above 0.6019 um
```

Fig. II.3.3.

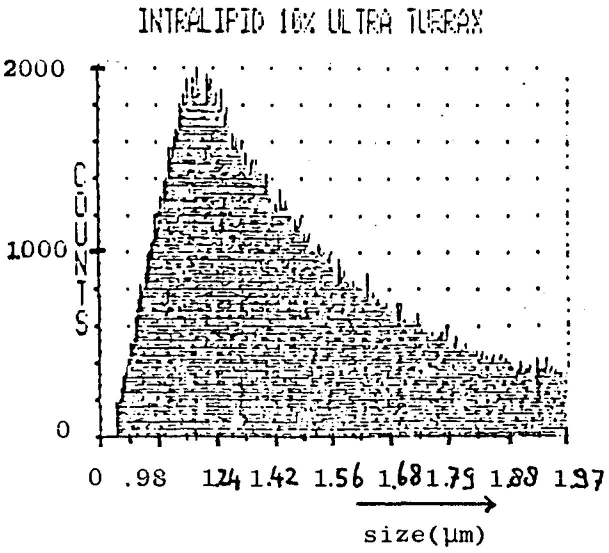

```
File: INTRALIPID 10% ULTRA TURRAX

              Statistical analysis
              ====================

          Calculation range: channel 1 to channel 256.
          Size scale: DIAMETER
           Weighting: None
          Calculations use the arithmetic mean.

          Mean size:   1.405 um
          Modal size:  1.176 um
          Median size: 1.394 um

          Variance:               8.257E-2
          Standard deviation: 0.2874 um
          Coeff of variation: 20.45%

          Skewness: 1.014E-2
          Kurtosis: -0.7178

          Distribution is right-skewed and platykurtic.

          Percentiles:
          ------------

             5  % above 1.885 um
            10  % above 1.809 um
            16  % above 1.729 um
            25  % above 1.626 um
            50  % above 1.394 um
            75  % above 1.190 um
            84  % above 1.109 um
            90  % above 1.037 um
            95  % above 0.9435 um
```

Fig. II.3.4

Measurement of the homogeneity of Intralipid from the St.Joseph Hospital; the vertical axis gives the relative amount of particles of a certain size, the horizontal axis gives the size of the particles in µm.

II.3.2 Determination of μ_a and μ_s.

A. To determine the absorption coefficient μ_a of Evans Blue, we used the experimental set-up shown in fig. II.3.5.

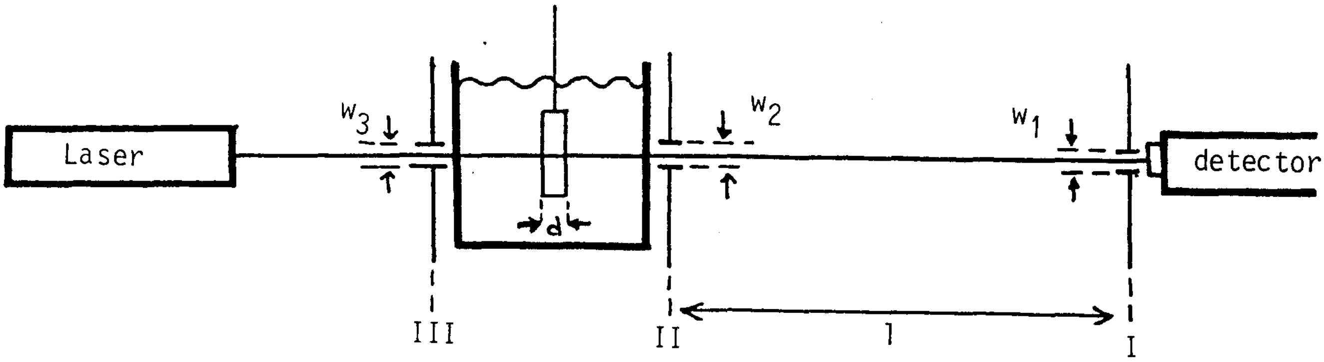

Fig. II.3.5: Experimental set-up for determination of μ_a and μ_s. I, II and III are pinholes with width w_1, w_2 and w_3.

A cuvet of diameter d is filled with the absorber and placed in a tank. The beam of e He-Ne laser is directed perpendicularly on the cuvet and the transmitted light is detected by a photodiode. This was repeated for several concentrations of Evans Blue and two cuvet-diameters.

To determine the absorption coefficient μ_a we used the "Beer-Lambert"-Law for substances which do not scatter:

$$\Psi = \Psi_o \exp(-\mu_a . c . d) \qquad \text{(II.3.1)}$$

where C is the concentration of the absorber.

Note that the absorption coefficient μ_a has here the dimension [length^{-1} concentration^{-1}]; the final value for μ_a has of course to be given for pure (100%) Evans Blue.

From this equation it is possible to calculate μ_a if μ_o and C are known. There was good evidence, however, that the sensitivity of the detector was not linear anymore when the detector was illuminated by the non-attenuated laser beam. Therefore we used:

$$\mu_a = -\frac{1}{d}\frac{\partial \ln \Psi}{\partial c} \tag{II.3.2.}$$

where d is the diameter of the cuvet

Ψ is the detected light intensity, which is proportional to the current of the detector.

c is the concentration of the absorber, where 100% is equal to 515 mg/l of Evans Blue.

The results are shown in fig. II.3.6.

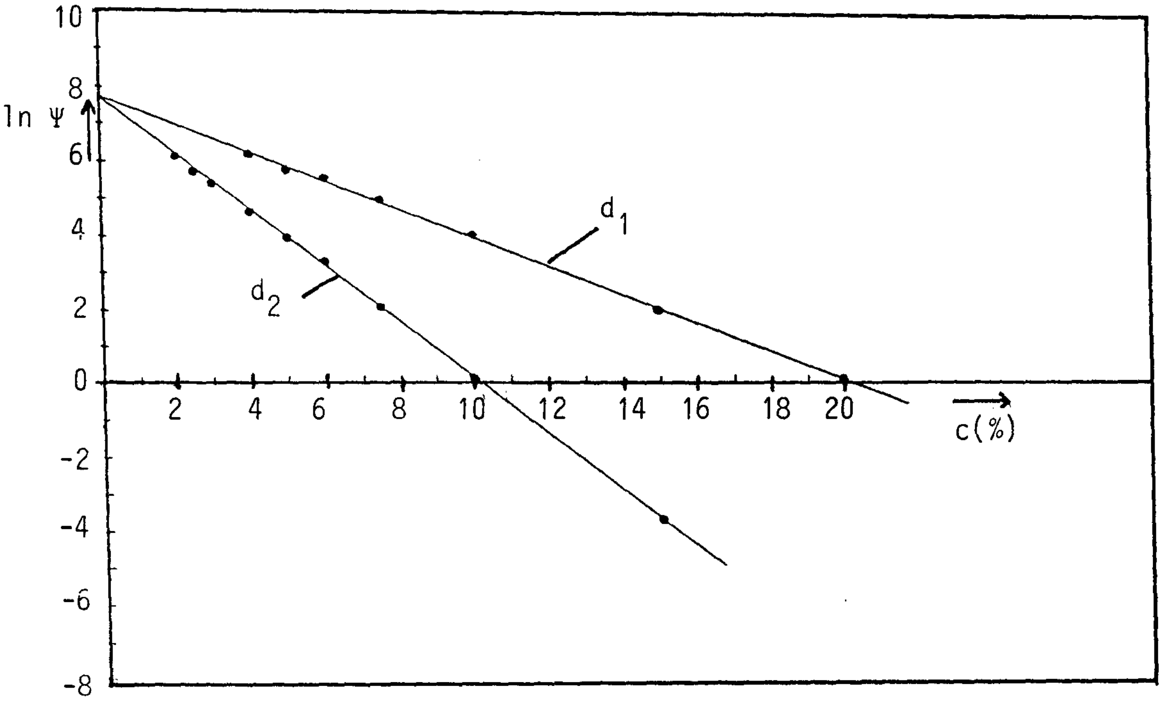

Fig. II.3.6: Logarithm of the detected light intensity as a function of the concentration of the absorber Evans Blue (515 mg/l) for two cuvets (d_1 = 0.5 cm and d_2 = 1.0 cm).

The slope $\frac{\partial \ln\Psi}{\partial c}$ was calculated by linear regression and the result for pure (100%) Evans Blue was:

for $d_1 = 0.5$ cm : $\mu_a = 7.654\ \mathrm{mm}^{-1}$

for $d_2 = 1.0$ cm : $\mu_a = 7.556\ \mathrm{mm}^{-1}$

so the average value, now taken for a solution of 1 ml per liter, is

$$\mu_a = (7.60 \pm 0.05) \times 10^{-3}\ \mathrm{mm}^{-1}\ \mathrm{ml}^{-1}\ \mathrm{l} \qquad (\mathrm{II}.3.3)$$

As a control experiment we made an absorption spectrum of Evans Blue. The result is presented in fig. II.3.7.

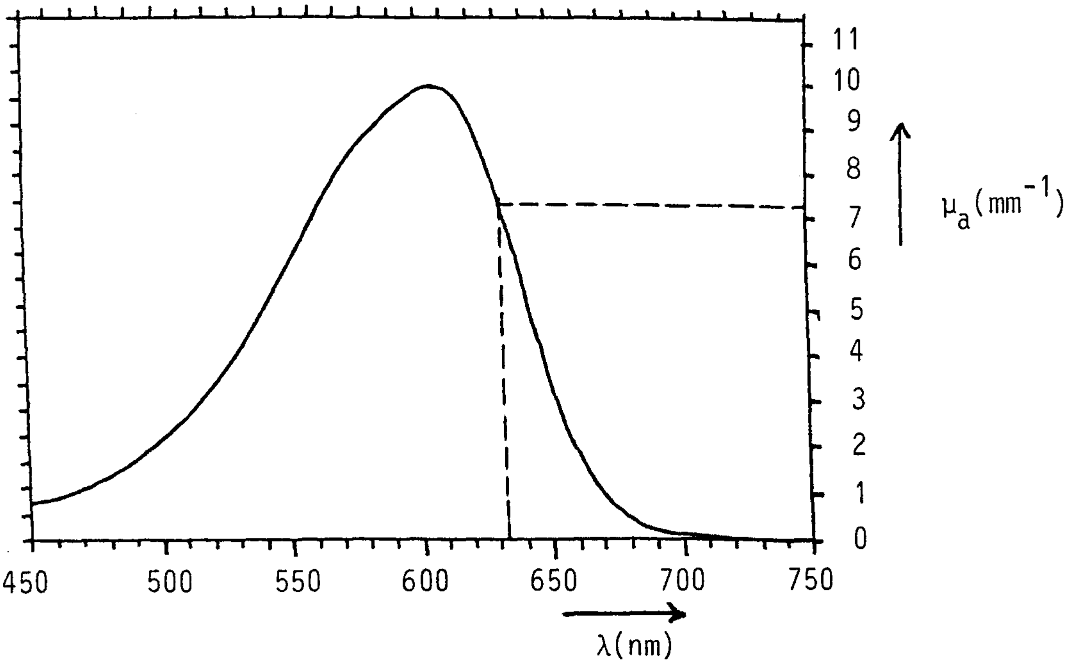

Fig. II.3.7: Absorption coefficient μ_a for pure Evans Blue as a function of the wavelength.

For the He-Ne laser wavelength ($\lambda = 632.8$ nm) we find:

$\mu_a = 7.4 \times 10^{-3}\ \mathrm{mm}^{-1}\mathrm{ml}^{-1}\mathrm{l}$

This result is in good agreement (within 2.6%) with the first result.

B. To determine the scattering coefficient μ_s of Intralipid, we used the same experimental set-up as in fig. II.3.5. Because Intralipid is strongly scattering, the whole cuvet can act as a light source; therefore it is necessary to measure the total attenuation (which is virtually equal to the scattering coefficient as absorption can be neglected with respect to scattering) under a very small angle and the combination of two pinholes I and II is now important (see fig. II.3.8).

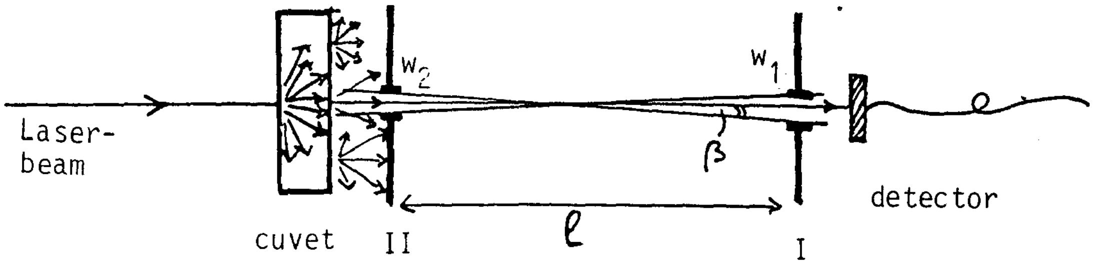

Fig. II.3.8: Measurement of μ_s with two pinholes with width w_1 and w_2 at distance l.

The angle β , which is half the opening angle, is given by (see appendix C):

$$\tan\beta = \frac{w_1+w_2}{2l} \qquad \text{(II.3.4)}$$

In this case we used pinholes with width $w_1 = 0.5$ mm and $w_2 = 1.1$ mm at length $l = 750$ mm, so $\beta = 1.0$ mrad.

To avoid multiple scattering we measured at low concentrations (up till a 1% solution). To measure μ_s we made the assumption that for low concentrations (single scattering) we may use

$$\Psi = \Psi_o \exp(-\mu_s . c . d) \tag{II.3.5}$$

or, because Ψ_o cannot be measured properly:

$$\mu_s = -\frac{1}{d}\frac{\partial \ln\Psi}{\partial c} \tag{II.3.6}$$

where d is diameter of the cuvet

Ψ is transmitted light, which is linear proportional to the current of the detector.

c is the concentration in percent, where 100% is non-diluted "Intralipid 10%".*)

Again we measured the transmitted light for several concentrations and two cuvet diameters. The results are shown in fig. II.3.9.

As a control experiment we repeated this measurement after a few weeks; these results are shown in fig. II.3.10.

---

*) Intralipid is available in bottles of "Intralipid 10%" and "Intralipid 20%"

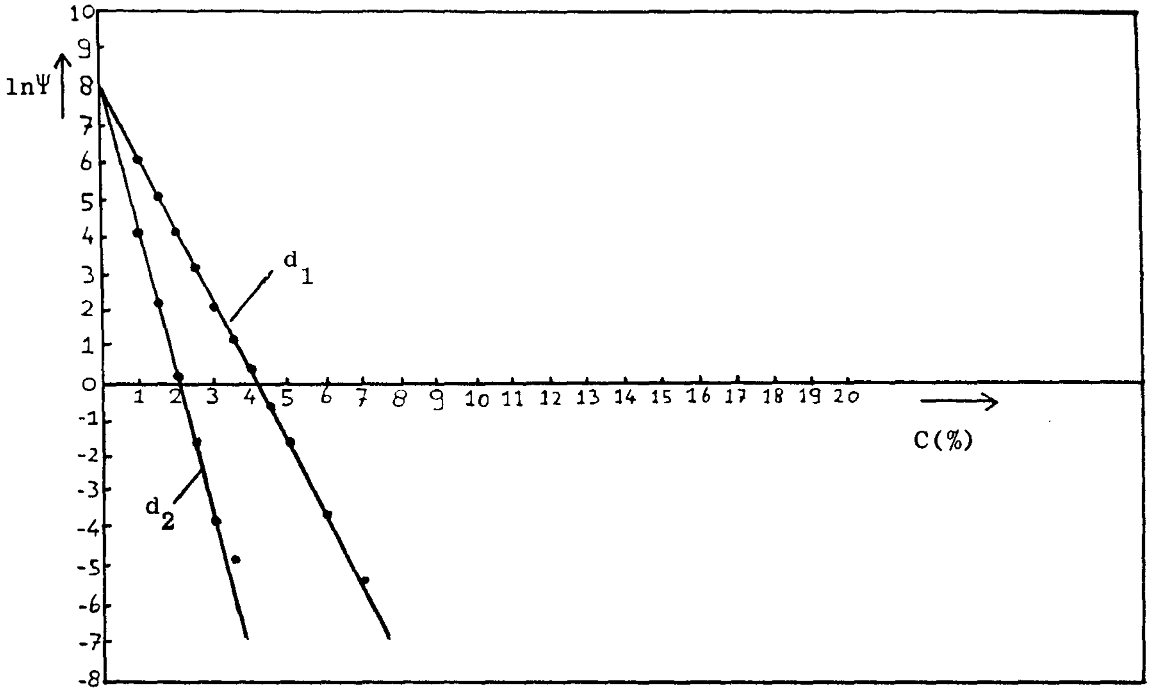

Fig. II.3.9: Logarithm of the detected light as a function of the concentration of Intralipid from the St.Joseph Hospital. (Discuvet diameter d_1 = 0.5 cm, d_2 = 1.0 cm).

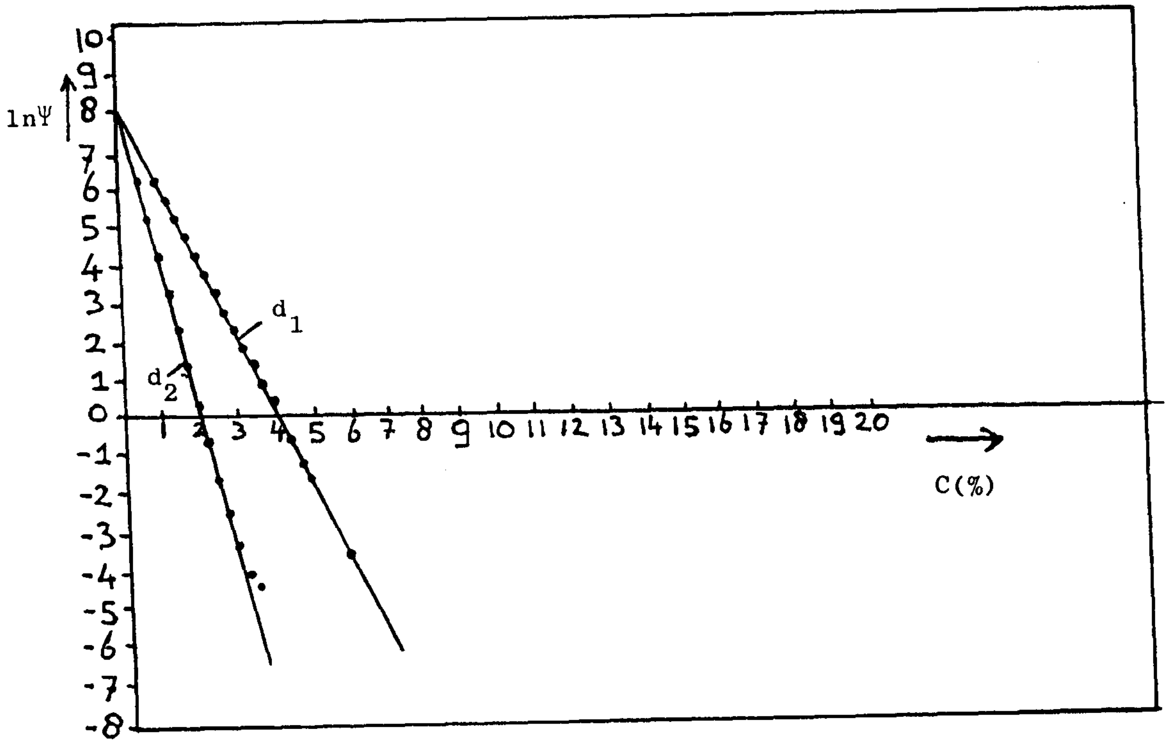

Fig. II.3.10: Logarithm of the detected light as a function of the concentration of Intralipid from the St.Joseph Hospital, measured after a few weeks.

Again the slope $\frac{\partial \ln\Psi}{\partial c}$ was calculated by linear regression and we find for fig. II.3.9 for pure Intralipid:

for $d_1 = 0.5$ cm : $\mu_s = 38.4\ \text{mm}^{-1}$

for $d_2 = 1.0$ cm : $\mu_s = 38.8\ \text{mm}^{-1}$

So the average value, now taken for a solution of 1 ml per liter, is

$$\mu_s = (38.6 \pm 0.2) \times 10^{-3}\ \text{mm}^{-1}\ \text{ml}^{-1}\ 1 \qquad \text{(II.3.7)}$$

For the control measurements in fig. II.3.10 we find:

for $d_1 = 0.5$ cm : $\mu_s = 38.6\ \text{mm}^{-1}$

for $d_2 = 1.0$ cm : $\mu_s = 37.8\ \text{mm}^{-1}$

So now the average value is

$$\mu_s = (38.2 \pm 0.4) \times 10^{-3}\ \text{mm}^{-1}\ \text{ml}^{-1}\ 1 \qquad \text{(II.3.8)}$$

which is within 1.0% from the value in II.3.7.

II.3.3. Determination of g.

To determine the asymmetry parameter g of Intralipid we had to use an indirect method; therefore we return to paragraph I.5.1. From eq. (I;5.3) we have the solution for a point source in an infinite medium:

$$\Psi(r) = \frac{c}{r} \exp(-\mu_{eff} r) \qquad \text{(II.3.9)}$$

where
$$\mu^2_{eff} = 3\,\mu_a\,\mu_{tr}$$
$$= 3\mu_a[\mu_a + (1-g)\mu_s] \qquad \text{(II.3.10)}$$

From eq. (II.3.9) we can determine μ_{eff} by

$$\mu_{eff} = -\frac{\partial}{\partial r}\ln(\Psi . r) \qquad \text{(II.3.11)}$$

which is the slope in a $\ln(\Psi \cdot r)$-r-diagram. From eq. (II.3.10) we can now calculate the g-value by:

$$g = 1 - \frac{\mu_a}{\mu_s}\left(\frac{\mu^2_{eff}}{3\,\mu^2_a} - 1\right) \qquad \text{(II.3.12)}$$

Note that with this method it is necessary to add absorber to the Intralipid to be able to calculate g.

For our experiments we used the experimental set-up shown in fig. II.3.11.

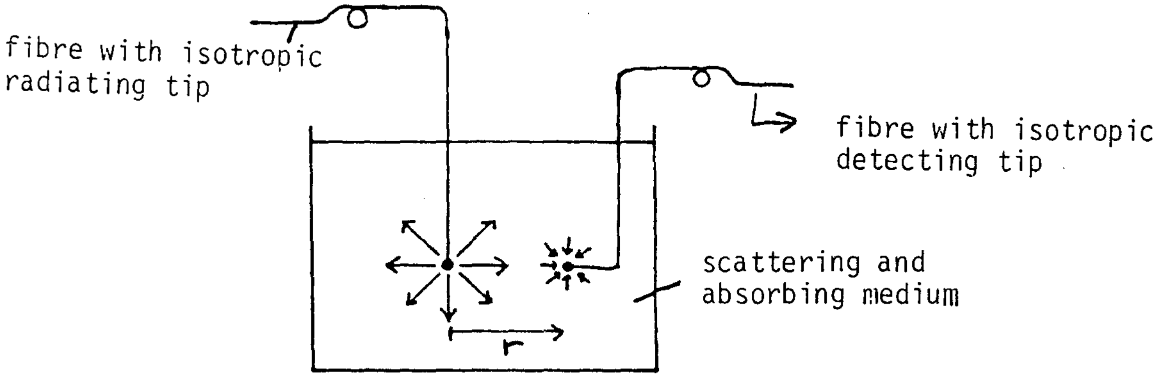

Fig. II.3.11: Experimental set-up for determination of μ_{eff}.

A fiber with an isotropic radiating tip is placed in a scattering and absorbing medium (containing Intralipid and Evans Blue) and the energy fluence rate Ψ is measured as a function of radius r with a fiber with an isotropic detecting tip.

The results are presented in figures II.3.12 and II.3.13. Measurements were carried out for two scattering coefficients and several absorption coefficients.

The slope which determines μ_{eff} was calculated by linear regression; the asymmetry parameter g was calculated by eq. (II.3.12). The results are presented in Table II.1.

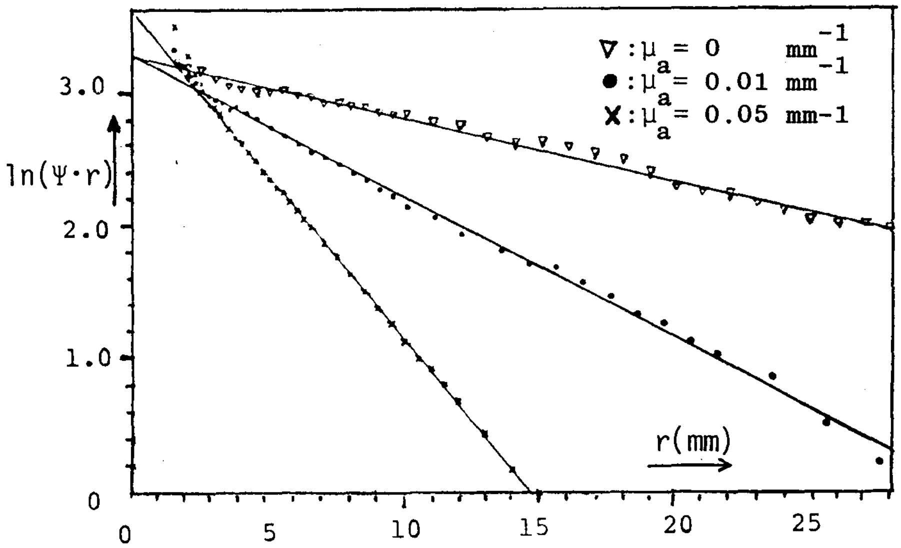

Fig. II.3.12: ln(Ψ .r)-r-diagram of the detected light intensity, for μ_s = 1 mm^{-1}. Used are mixtures of Intralipid from the St. Joseph Hospital and Evans Blue.

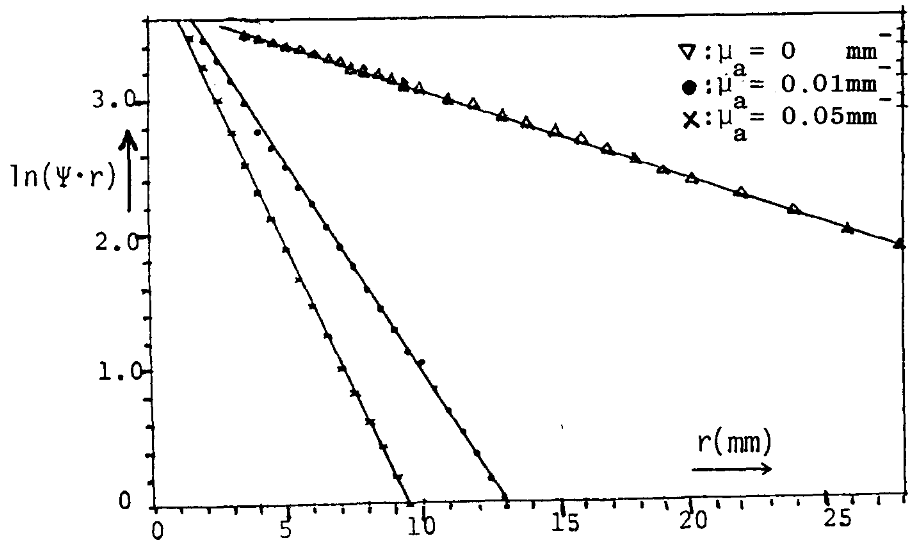

Fig. II.3.13: ln(Ψ .r)-r-diagram of the detected light intensity, for μ_s = 2 mm^{-1}. Used are mixtures of Intralipid from the St. Joseph Hospital and Evans Blue.

μ_s ($\pm$ 1%)	μ_a ($\pm$ 1%)	μ_{eff}	g
1 mm^{-1}	0 mm^{-1}	0.041 mm^{-1}	x
1 mm^{-1}	0.01 mm^{-1}	0.105 mm^{-1}	0.642
1 mm^{-1}	0.05 mm^{-1}	0.245 mm^{-1}	0.651
2 mm^{-1}	0 mm^{-1}	0.061 mm^{-1}	x
2 mm^{-1}	0.05 mm^{-1}	0.313 mm^{-1}	0.698
2 mm^{-1}	0.10 mm^{-1}	0.429 mm^{-1}	0.743

Table II.1: Results and calculated g-value for Intralipid from the St.Joseph Hospital.

From these values we can determine the average value for g with standard deviation, and we find:

$$\hat{g} = 0.68 \pm 0.05 \qquad (II.3.13)$$

We also measured pure Intralipid without addition of absorber (see table II.1); from the calculated μ_{eff}-values we can determine the absorbance of pure Intralipid μ_{ao}, from eq. (II.3.12) and we find for the two cases:

$$\mu_s = 1\ mm^{-1};\ \mu_{ao} = 6.7 \times 10^{-5}\ mm^{-1}\ ml^{-1}\ l$$

$$\mu_a = 2\ mm^{-1};\ \mu_{ao} = 3.7 \times 10^{-5}\ mm^{-1}\ ml^{-1}\ l$$

as an average value therefore we find:

$$\mu_{ao} = (5.2 \pm 1.5) \times 10^{-3}\ mm^{-1}\ ml^{-1}\ l \qquad (II.3.14)$$

This value cannot be neglected compared to the absorbance of Evans Blue in the media we have used (26 ml/1 and 52ml/1 of Intralipid); we have to add the absorbance of Intralipid to the absorbance of Evans Blue and recalculate the g-value. This gives the results shown in Table II.2, where g* is the corrected g-value (corrected for the absorption μ_{ao} of Intralipid).

μ_s	μ_a	μ_{eff}	g*
1 mm^{-1}	0.0113 mm^{-1}	0.105 mm^{-1}	0.685
1 mm^{-1}	0.0513 mm^{-1}	0.245 mm^{-1}	0.662
2 mm^{-1}	0.0526 mm^{-1}	0.313 mm^{-1}	0.716
2 mm^{-1}	0.0526 mm^{-1}	0.429 mm^{-1}	0.752

Table II.2: Corrected results and g*-value for Intralipid from the St.Joseph Hospital.

From these corrected g*-values we can determine the average and the standard deviation:

$$\hat{g}^* = 0.70 \pm 0.04 \qquad \text{(II.3.15)}$$

as the final result for the asymmetry parameter g.

II.4 Comparison with other results.

The results in paragraph II.3 of Intralipid were compared with the values found by other investigations. The results are shown in Table II.3.

	μ_s	μ_{ao}	g
Star W.M.1)	0.045	0.8×10^{-5}	0.83
Jacques S.L.2)	0.0417		0.55
Wilson B.C.3)	0.0384	1.6×10^{-5}	0.69
Moes C.J.M.	0.0386	5×10^{-5}	0.70

Table II.3: Comparison of the results of Intralipid; μ_s and μ_{ao} are in (mm^{-1} ml^{-1} 1).

1) R.R.T.I., Rotterdam, The Netherlands.

2) Harvard Medical School, Boston, U.S.A.

3) Hamilton Regional Cancer Centre, Ontario, Canada.

From Table II.3 we see that the values differ substantially, particulary the g-values, although the results of Wilson and ours show good agreement.

It was not clear, however, whether these differences were due to material differences or to a different method of measurement. As a control experiment all four groups therefore used Itralipid from the same bottle (from W.M. Star) to be sure to have the same material, and measured again, each one with his own method.

Our results are shown in figures II.4.1 and II.4.2. The method of measurement is exactly the same as explained in paragraph II.3.

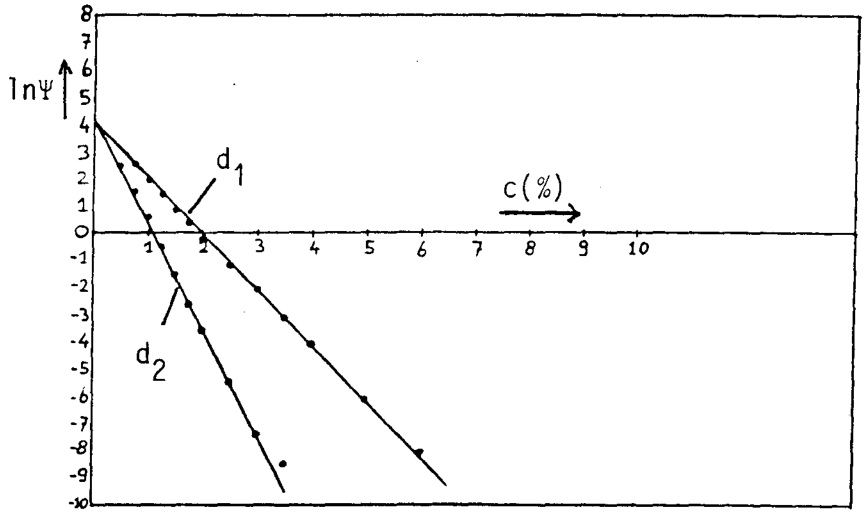

Fig. II.4.1: Determination of scattering coefficient μ_s of Intralipid from RRTI, Rotterdam conform the method in paragraph II.3.2 (d is cuvet diameter, $d_1 = 0.5$ cm, $d_2 = 1.0$ cm). Compare with figs. II.3.9 and II.3.10.

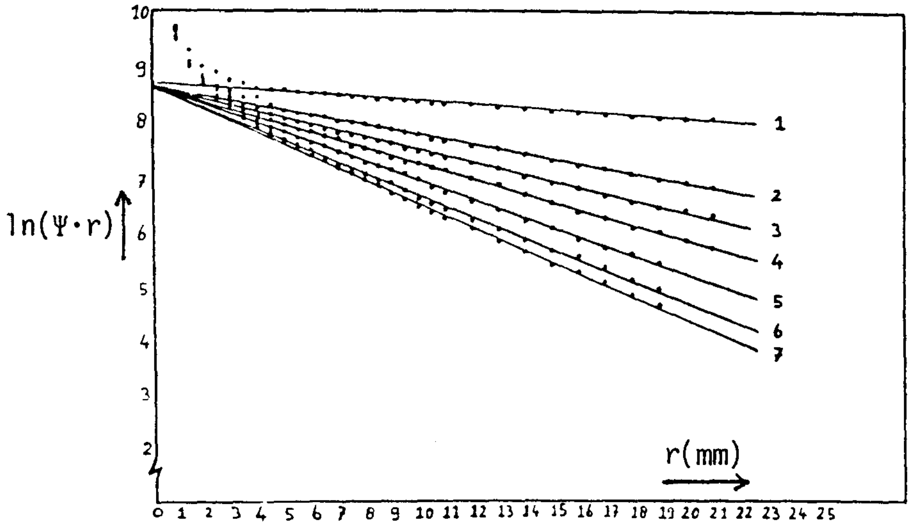

Fig. II.4.2: Determination of μ_{eff} conform the method in paragraph II.3.3. The numbers 1 to 7 indicate different absorption coefficients μ_a, the scattering coefficient $\mu_s = 1$ mm^{-1}. Used are mixtures of Intralipid from RRTI, Rotterdam and Evans Blue (compare with figs. II.3.12 and II.3.13).

From fig. II.4.1 we find for the scattering coefficient μ_s for pure Intralipid from RRTI, Rotterdam:

$$\mu_s = (40.0 \pm 0.2) \times 10^{-3} \quad mm^{-1}\ ml^{-1}\ l \qquad (II.4.1)$$

The angle between the pinholes was the same as in paragraph II.3.2, namely $\beta = 1.0$ mrad.

We see that the value for μ_s from RRTI, Rotterdam in eq. (II.4.1) is 3.5% larger than the value in paragraph II.3.2.

In fig. II.4.1 we see a diagram of ln (Ψ .r)-r where r is the radius, conform the method described in paragraph II.3.3. The numbers 1 to 7 indicate different absorption coefficients μ_a of Evans Blue.

From fig. II.4.1 we can determine μ_{eff} by linear regression and subsequently calculate the asymmetry parameter g from eq. (II.3.12). The results are shown in Table II.4.

no.	μ_s	μ_a	μ_{eff}	g
1	1 mm^{-1}	0 mm^{-1}	0.034 mm^{-1}	x
2	1 mm^{-1}	0.065 mm^{-1}	0.091 mm^{-1}	0.586
3	1 mm^{-1}	0.012 mm^{-1}	0.114 mm^{-1}	0.643
4	1 mm^{-1}	0.020 mm^{-1}	0.138 mm^{-1}	0.702
5	1 mm^{-1}	0.030 mm^{-1}	0.174 mm^{-1}	0.695
6	1 mm^{-1}	0.040 mm^{-1}	0.196 mm^{-1}	0.719
7	1 mm^{-1}	0.050 mm^{-1}	0.216 mm^{-1}	0.738

Table II.4: Results and calculated g-value for Intralipid from RRTI, Rotterdam. The numbers 1 to 7 refer to the curves in fig. II.4.2. (compare with Table II.1).

From Table II.4. we find for the average g-value:

$$\hat{g} = 0.68 \pm 0.05 \qquad (II.4.2)$$

Again we can use this value to determine the absorption μ_{ao} of Intralipid itself and we find:

$$\mu_{ao} = 5 \times 10^{-5} \ mm^{-1} \ ml^{-1} \ l \qquad (II.4.3)$$

Again this value cannot be neglected for the media we have used (25 ml/l of Intralipid) and we have to add this absorbance to the absorption coefficient μ_a in Table II.4. The corrected values and the corresponding corrected g*-values are summarized in Table II.5.

no.	μ_s	μ_a	μ_{eff}	g*
2	1 mm^{-1}	0.008 mm^{-1}	0.091 mm^{-1}	0.655
3	1 mm^{-1}	0.013 mm^{-1}	0.114 mm^{-1}	0.679
4	1 mm^{-1}	0.021 mm^{-1}	0.138 mm^{-1}	0.722
5	1 mm^{-1}	0.031 mm^{-1}	0.174 mm^{-1}	0.710
6	1 mm^{-1}	0.041 mm^{-1}	0.196 mm^{-1}	0.730
7	1 mm^{-1}	0.051 mm^{-1}	0.216 mm^{-1}	0.747

Table II.5: Corrected results and g*-values for Intralipid from RRTI, Rotterdam (compare with Table II.2).

From Table II.5 we can calculate the average g*-value, finding:

$$\hat{g}^* = 0.71 \pm 0.03 \qquad (II.4.4)$$

II.5 Summary of the results.

Finally we can compare these values with the values found by the other members mentioned in Table II.3. Because we all used the same Intralipid from RRTI, Rotterdam, all differences are due to a difference in the method of measurement. These results for Intralipid from the RRTI in Rotterdam are summarized in Table II.5, together with the results for Intralipid from the St. Joseph Hospital and which is used in all further experiments.

		μ_s	μ_{ao}	g
A.	Moes C.J.M.	$(38.6 \pm 0.2)x10^{-3}$	5×10^{-5}	0.70
B.	Star W.M.	$(40.0 \pm 0.1)x10^{-3}$	$1.2x10^{-5}$	0.67
	Jacques S.L.	*]		
	Wilson B.C.	*]		
	Moes C.J.M.	$40.0 \pm 0.2x10^{-3}$	5×10^{-5}	0.71

Table II.5: Comparison of the coefficients of Intralipid,
(μ_s and μ_{ao} are in mm^{-1} ml^{-1} 1).
A: Results for Intralipid from St. Joseph Hospital.
B: Results for Intralipid from RRTI in Rotterdam.

***] These results were not known at the moment of writing.**

III. Brain tissue phantom experiments.

III.1 Introduction.

In this chapter we will turn to a more clinical situation, namely the treatment of malignant brain tumours. The majority (up to 90%) of these malignant gliomas appear focal. About half of these gliomas show evidence of macroscopic invasion into the white matter of the brain; thus for these gliomas there is not a sharp separation between tumour and normal tissue, but there is a diffuse area where tumour cells are inbedded in normal tissue [Sandeman, 1986]. The conventional therapy has consisted of resection, where possible, followed by adjuvant radiotherapy and chemotherapy to treat residual tumour [Sandeman, 1986], see fig. III.1.1

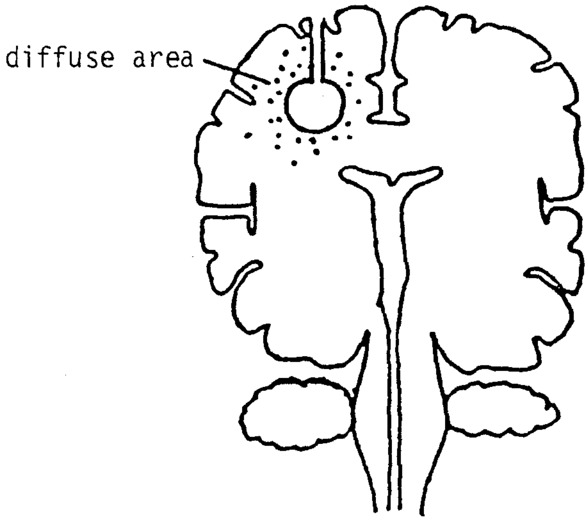

Fig. III.1.1: Model of the brain; part of the tumour is cut out.

The results, however, have been poor; in all treatments the two-year survival has been in the region of 10% or less, irrespective of the therapy [Salcman, 1980], see fig. III.1.2.

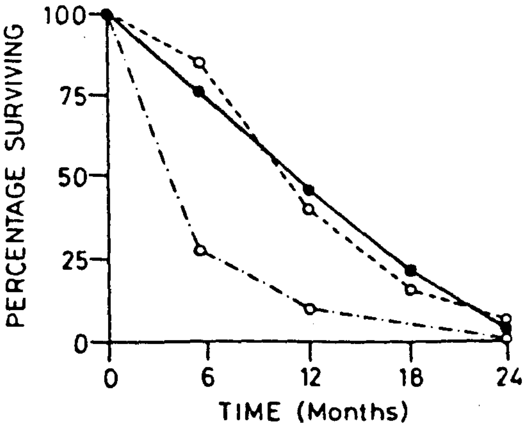

Fig. 1. Survival in glioblastoma. Results of a retrospective analysis by Salcman, 1980(4), published by kind permission of the Congress of Neurological Surgeons. O–·–O, surgery alone; O—–O, surgery + DXR; ●——●, surgery + DXR + chemotherapy.

Fig. III.1.2: Survival of glioblastoma.

It is clear that "present therapeutic methods for malignant gliomas are so ineffective in influencing longterm survival that all new potential treatment modalities should be fully evaluated" [Sandeman, 1986].

Therefore Photodynamic Therapy (PDT), described in the introduction of this report, can conceptually be a rather good method because tumour cells are more affected by this therapy then normal cells, which is very important in the brain. Besides there is good evidence that whereas the concentration-ratio of HpD for tumour-to-normal tissue is 2:1 or 3:1 for most tissues, it is in the order of 26:1 [Wharen, 1983] or 35:1 [Salcman, 1980] for the brain.

A time-depending graph of this concentration-ratio, measured by [Salcman, 1980], is shown in fig. III.1.3.

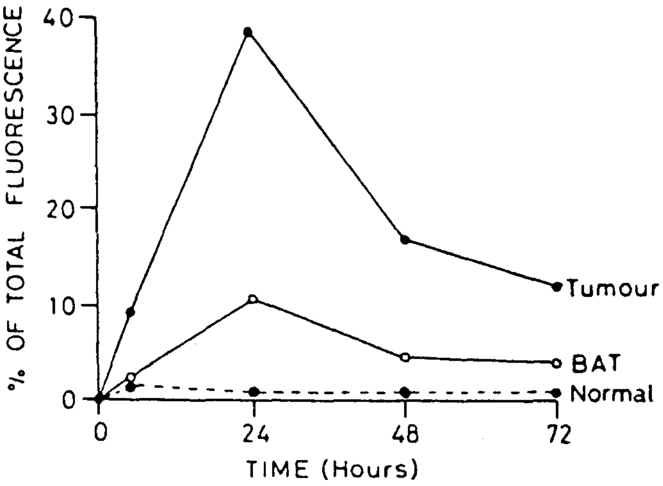

Fig. III.1.3: Fluorescence in the normal brain tumour, and the brain adjacent to tumour (BAT). From [Sandeman, 1986].

This makes PDT a very selective method for treatment of malignant gliomas.

An applied method for the follow-up is described by Wilson B.C. [Wilson, 1986]. The tumour cells can be selectively killed. In this method a rubber balloon is inserted inside the resected hole in the brain and filled with a purely scattering medium. After that a fibre is placed in the middle of the balloon and the light will be multiple scattered. With proper positioning of the fibre the balloon will act as an isotropic diffuse light source (see fig. III.1.4).

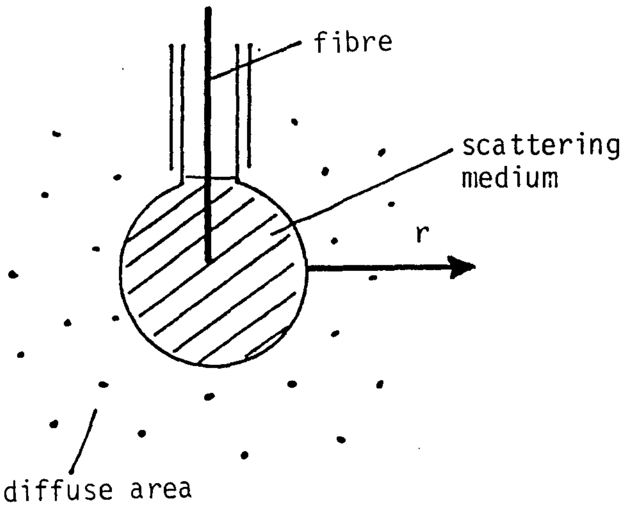

Fig. III.1.4: Diffuse light source for treatment of malignant brain tumour.

In this way the light can penetrate into the brain tissue and in combination with the photosensitizer HpD the tumour cells can be selectively killed.

However, when we look at the effective penetration depth of the light in the tissues as measured by B.C. Wilson, we see that the results are only in the order of 2 to 5 mm (see fig. III.1.5). The effective penetration depth ($= \mu^{-1}_{eff}$) is the depth required to reduce the irradiance in the tissue to 1/e or 37% and is given by the slope of the graph of $\ln(\Psi .r)$ against r (see fig. II.3.11).

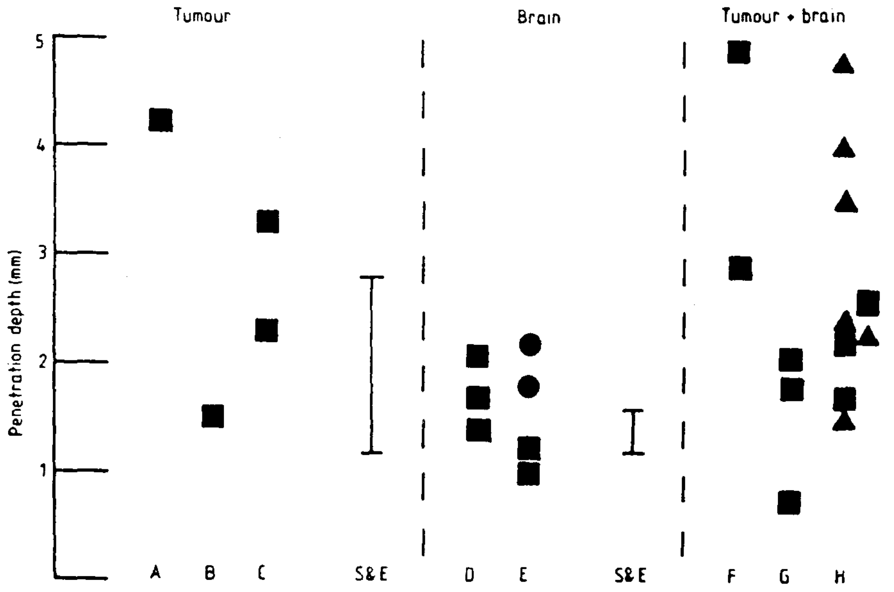

Figure 1. Penetration depths, as in table 1: ■, *in vivo*, post irradiation; ●, *in vivo*, pre irradiation; ▲, *in vitro*, pre irradiation; S & E, range of values from Svaasand and Ellingsen (1983, 1985), *in vitro*, pre irradiation.

Fig. III.1.5: Penetrations depths in brain tissue for irradiation with diffuse sphere.

A method to improve the penetration of light into the tissue is therefore clinically very relevant.

A first attempt was to compare this situation of diffuse illumination with collimated illumination, because the idea was that with collimated illumination we get deeper penetration of light compared with diffuse illumination (see fig. III.1.6).

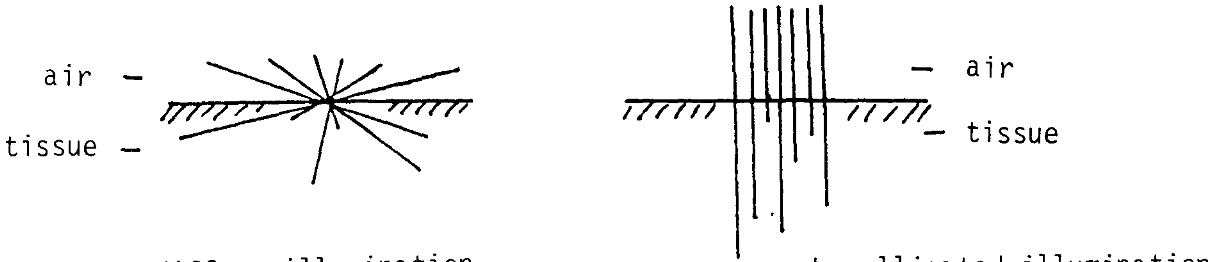

a diffuse illumination

b collimated illumination

Fig. III.1.6: Comparison of diffuse and collimated illumination; shown are the paths of the unattenuated photons before interaction with the tissue.

Therefore we used the light source shown in fig. III.1.7

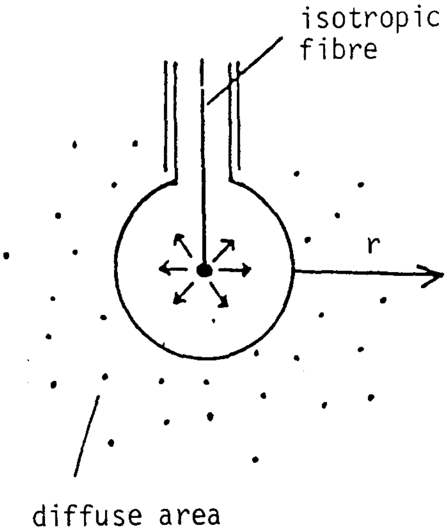

Fig. III.1.7: Isotropic irradiation: point source placed in the middle of the balloon with diameter d = 54 mm.

A fibre with an isotropic radiating tip is placed in the middle of the balloon (in this case consisting of glass instead of rubber). The balloon was filled with air, water or a scattering medium respectively.

The light distribution was measured by a fibre with an isotropic detecting tip; as a tissue phantom we used Intralipid ($\mu_s = 1 \text{ mm}^{-1}$, no absorbance added), (see fig. III.1.8).

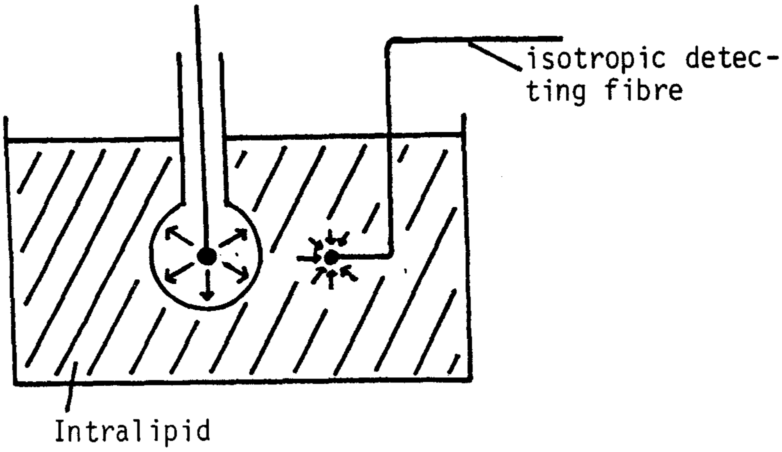

Fig. III.1.8

The results are shown is fig. III.1.9.

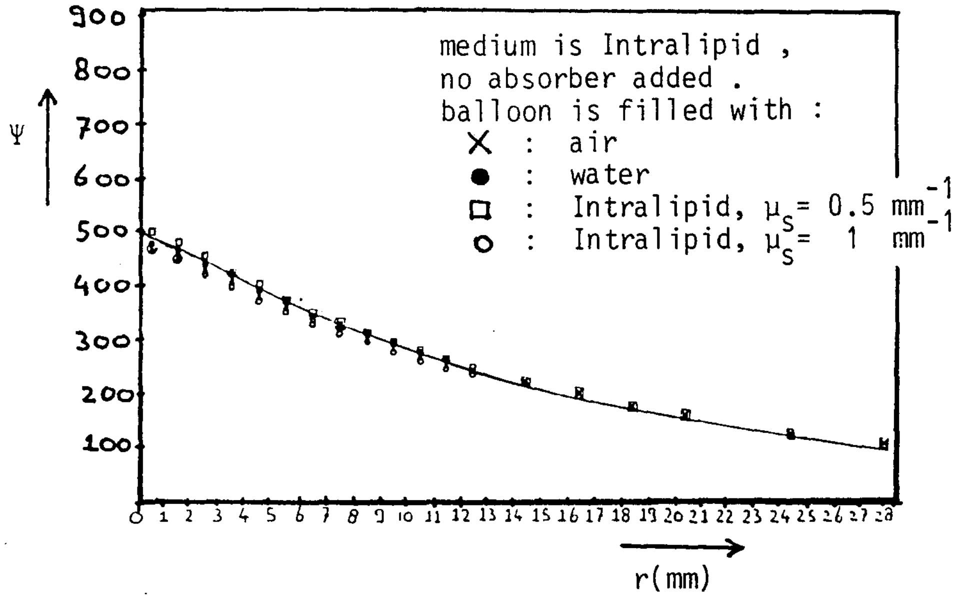

Fig. III.1.9: Light distribution inside the medium as a function of the distance r, measured from the surface of the balloon.

From the results it is clear that in this way it is hardly possible to influence the penetration of light; it makes no difference whether there is a scattering medium inside the balloon or not.

III.2 Modelling the light distribution.

The question which arises now is whether it is possible to realise deeper penetration of light in the tissue without creating an overdose of light at the edge of the tissue (this could be harmful because of possible heating effects).

From the previous paragraph it is clear that changing diffuse incident light into collimated incident light makes virtually no difference; therefore we have to look more closely to the predicted light distribution inside the medium.

What we like to have is a constant light intensity as a function of the distance r (measured from the surface of the balloon), inside the medium (see fig. III.2.1A). Ψ min is the minimum light fluence for necrosis of the tumour cells. What we obtain, however, is the pattern shown in fig. III.2.1B, which is the light distribution for a point source inside a balloon. This curve is described by eq. I.5.4, thus

$$\Psi \sim \frac{1}{r} \exp(-\mu_{eff} r) \qquad \text{(III.2.1)}$$

When we increase the light intensity there will be a deeper penetration of the light, but the edge of the tissue can receive an overdose of light (see fig. III.2.1C).

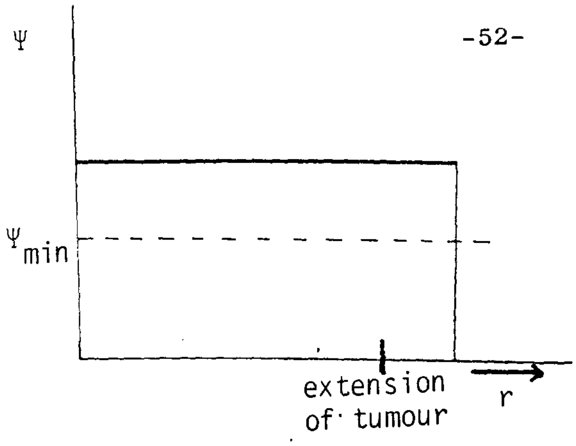

Fig. III.2.1A: Ideal light distribution.

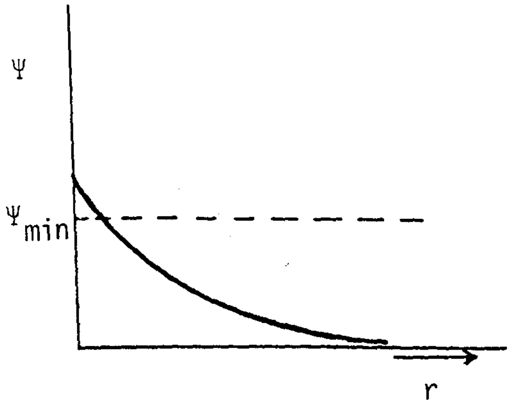

Fig. III.2.1B: Light distribution with isotropic irradiation, small intensity.

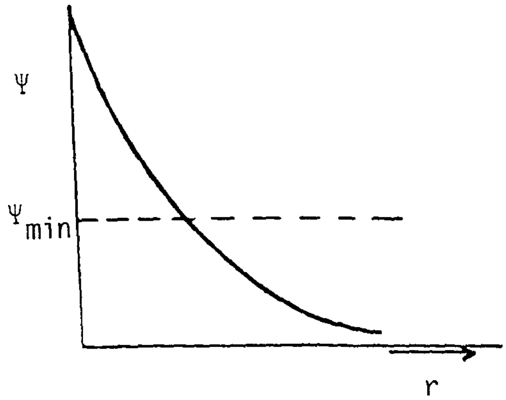

Fig. III.2.1C: Light distribution with isotropic irradiation, higher intensity.

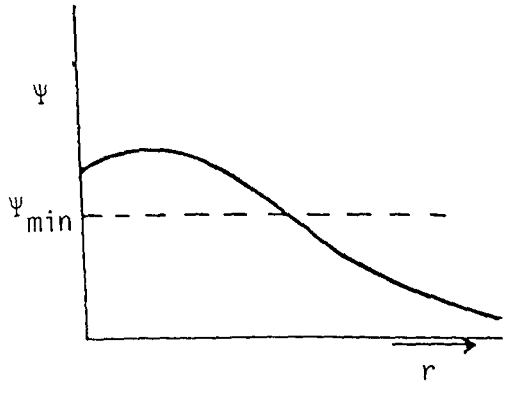

Fig. III.2.1D: Light distribution when irradiated with a forward directed wide beam

For a deeper penetration, another attempt is: irradiate with a forward directed wide beam. According to paragraph I.3 we can expect for a wide light beam roughly the pattern shown in fig. III.2.1D and beyond a few mean free paths the curve will behave according to eq. I.3.9, thus (when we make the transition from carthesian coordinates to spherical coordinates, and substitute z by r)

$$\Psi \sim \exp(-\mu_{eff}r) \qquad \text{(III.2.2)}$$

Comparing eq. (III.2.2) with eq. (III.2.1) it is clear that the decrease of the light intensity for a wide beam is smaller then for a point source.

Our suggestion therefore is to create a forward directed wide beam within the balloon. For this purpose half of the balloon was coated to make it a mirror (see fig. III.2.2A). Again the fibre with isotropic radiating tip was inserted, but now placed in the focus of the mirror instead of the centre.*) A forward directed wide beam will be the result.

Some other possible advantages of the system are that with a variation of the tip in horizontal direction there is the possibility for a diverging, parallel or focussed beam.

*) To avoid direct radiation, a little mirror was placed just behind the tip.

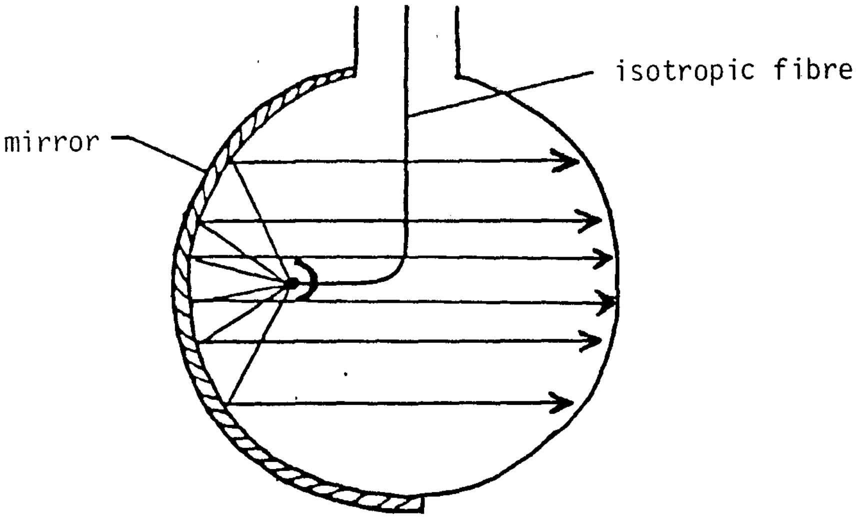

Fig. III.2.2A: System for wide beam experiment.

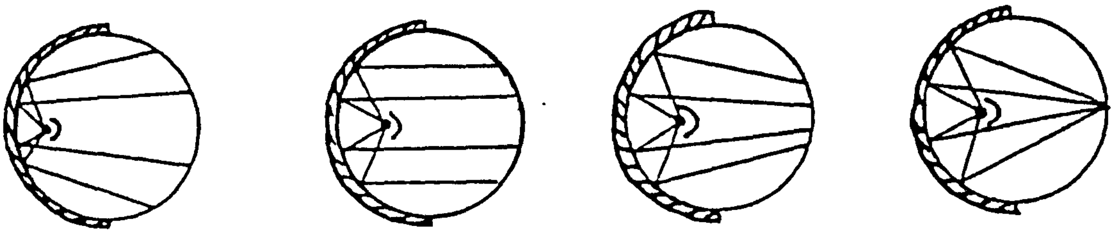

Variation in horizontal direction ⟷

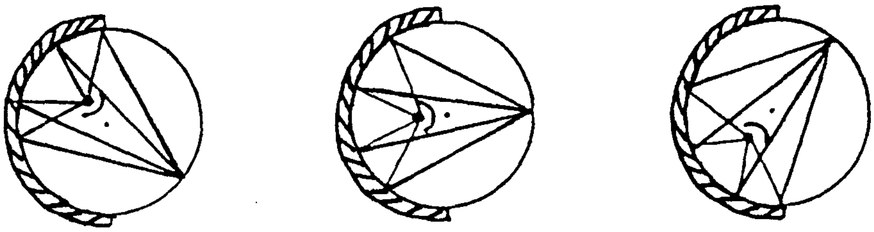

Variation in radial direction

Fig. III.2.2B: Possibilities for application.

III.3 Experimental results.

We carried out some experiments to compare the system with a mirror (see fig. III.2.2A) with the system of isotropic irradiation (see fig. III.1.7). In both cases the balloon was filled with water to realise index-matching. The measurements were carried out for a diverging, a parallel and two focussed beams (see fig. III.2.2B). As tissue phantoms we used three scattering and absorbing media with optical parameters $\mu_s = 1\ \mathrm{mm}^{-1}$, $g = 0.7$ and $\mu_a = 0\ \mathrm{mm}^{-1}$, $\mu_a = 0.01\mathrm{mm}$, $\mu_a = 0.05\ \mathrm{mm}^{-1}$ respectively. These parameters differ from the parameters of brain tissue which are in the order of $\mu_s = 5\ \mathrm{mm}^{-1}$, $g = 0.9$ and $\mu_a = 0.15\ \mathrm{mm}^{-1}$ [Splinter, 1987]. Nevertheless we have chosen for the first parameters to be able to measure also deeper indside the phantom.

In this paragraph we will present the measurements; the results will be discussed in paragraph III.4.

The experimental set-up we have used is shown in fig. III.3.1.

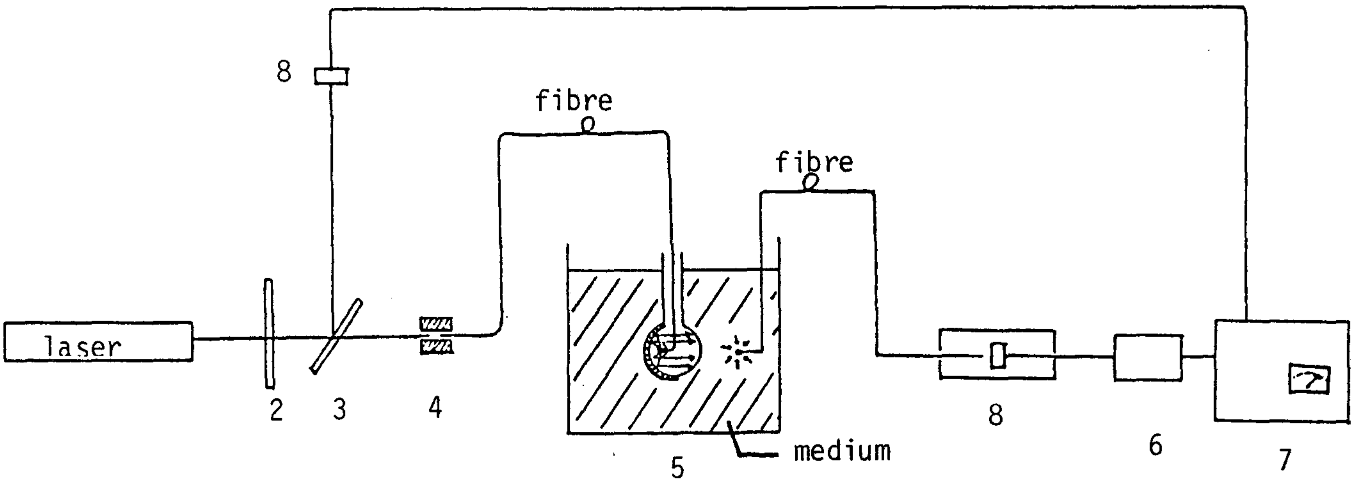

1. laser, 14 mW, 632.8 nm
2. chopper
3. beamsplitter
4. coupling
5. model for measurements
6. current-voltage converter
7. lock-in amplifier
8. diodes

Fig. III.3.1: Experimental set-up for brain tissue phantom experiments.

First of all we carried out measurements for the system of isotropic irradiation which we define, following Wilson [Wilson, 1986], as a point source inside a sphere filled with water (see fig. III.1.7); the results are presented in fig. III.3.2. The vertical axis gives the ratio of the energy fluence rate inside the medium and the incident energy fluence rate at the surface of the balloon; the horizontal axis is the distance r in mm measured from the surface of the balloon. The solid lines are the theoretical curves calculated with eq. I.5.4 and normalised at the incident energy fluence rate per mm^2 at the surface of the balloon.

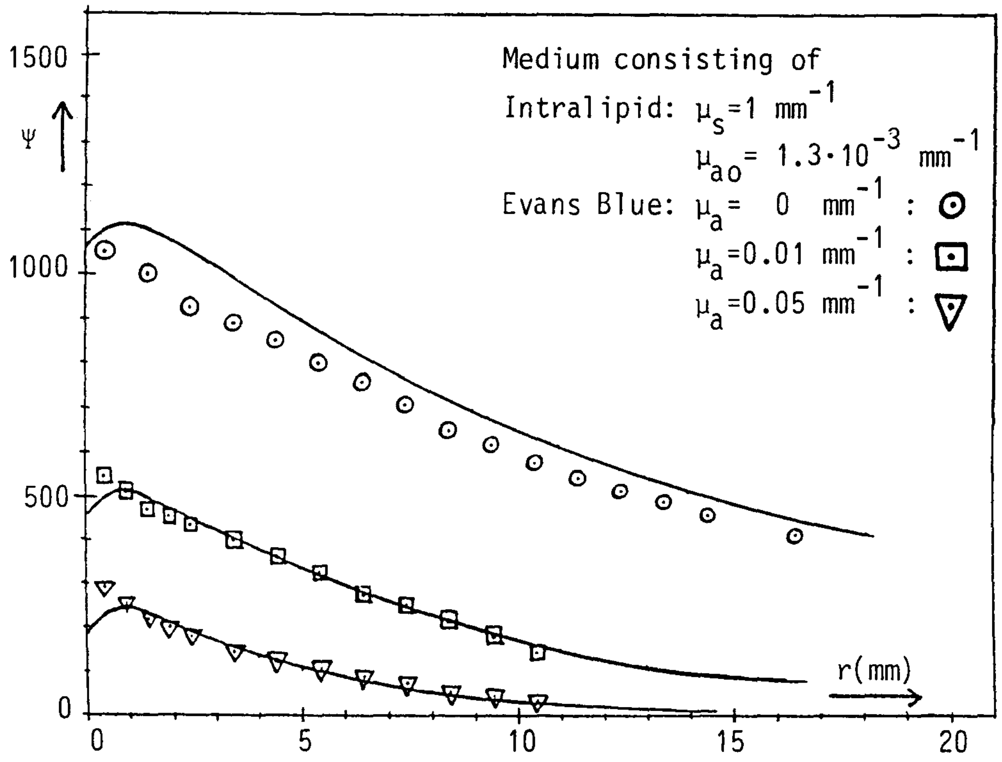

Fig. III.3.2: Results for isotropic irradiation (point source in a sphere filled with water, no mirror).

Second, we carried out measurements for the system with a mirror; these results are shown in figures III.3.3 to III.3.6. In fig. III.3.3 the pattern of the incident beam is shown for the balloon with mirror; for this purpose the medium was replaced by water (no scattering, no absorption). We measured in the x-directon at z = 0 (see fig. III.3.3).

In each picture of fig. III.3.3 the vertical axis at the left gives the energy fluence rate in arbitrary units. In each picture of fig. III.3.3 we also calculated the average value; this average value in each picture was called $I_{100\%}$ and is given at the vertical axis at the right side in each picture. By assigning $I_{100\%}$ in the case of a parallel beam the value I_o, we can compare the four patterns in fig. III.3.3 mutually. In the first three patterns in fig. III.3.3 we see a dip in the middle; this dip is caused by the little mirror just behind the isotropic radiating tip (see fig. III.2.2A). The two peaks in all of the first three patterns are caused by the fact that the mirror is a sphere and not a parabola what it should be to create a parallel beam (see also the discussion in paragraph III.4).

In figures III.3.4 to III.3.6 the measurements for the balloon with mirror in the case of a diverging, a parallel and a focussed beam are shown. For the mdium we used Intralipid and Evans Blue; the optical coefficients of each medium are given in the figures. The circle in each figure is the edge of the balloon, the medium is beneath it.

Next we have to compare the measurements of the system with the mirror with the system of isotropic irradiation. For this purpose we measured from the figures III.3.4 to III.3.6 the decrease in the energy fluence rate as a function of the distance r, measured from the surface of the balloon. To avoid measuring in the shadow caused by the dip of the incident beam (see also fig. III.3.3) we measured not along the vertical z-axis, but along the axis A-B shown in the figures. The results are shown in figurews III.3.7 to III.3.9. To be able to compare the system of isotropic irradiation with the system with mirror it is necessary to divide the results of fig. III.3.2 (isotropic irradiation) by a certain factor to equalize the results of both systems at the surface of the balloon, and thereafter look at the decrease of both systems inside the medium. This has been done for each picture in the figures III.3.7 to III.3.9. In each figure the vertical axis gives the relative energy fluence rate normalized to the incident fluence rate $I_{100\%}$ (see also fig. III.3.3), as a function of the distance r measured from the surface of the balloon.

Fig.III.3.3

Pattern of the incident beam. Both inside and outside the sphere is clear water, so there is neither scattering nor absorption.

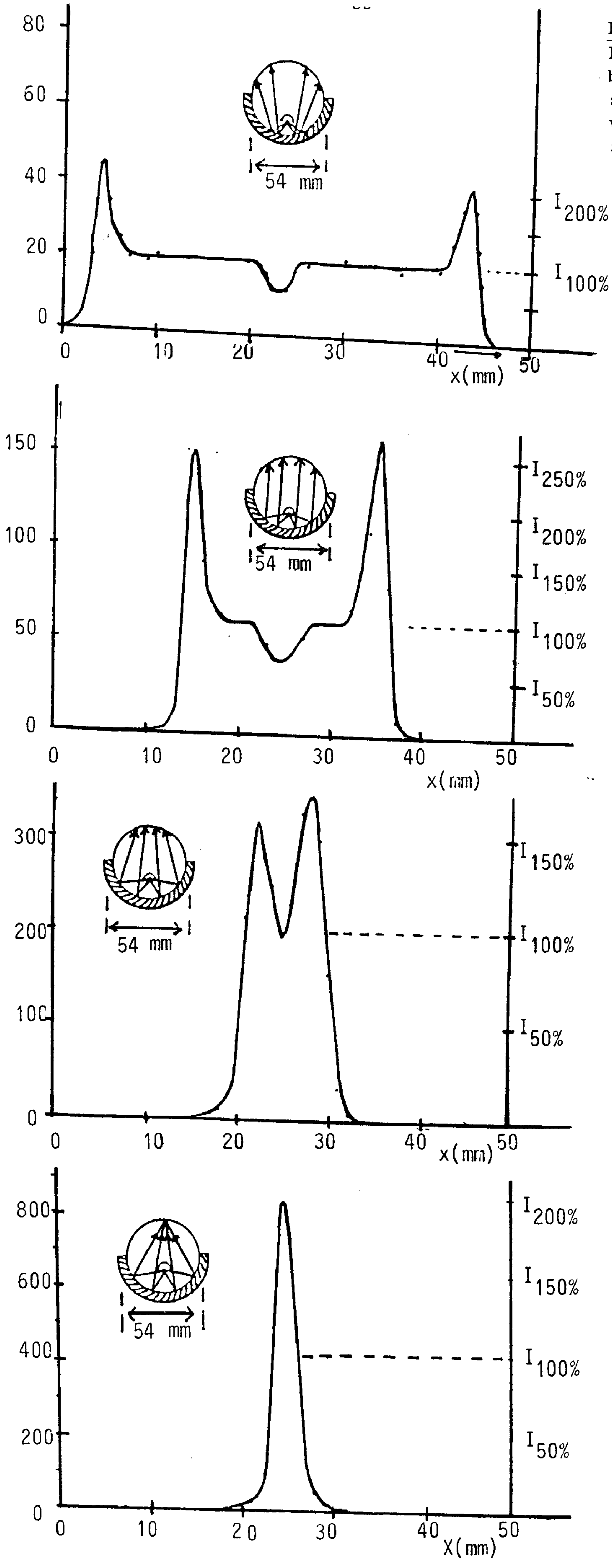

$I_{100\%} = 1/3\ I_0$

$I_{100\%} = I_0$

$I_{100\%} = 3.33\ I_0$

$I_{100\%} = 7\ I_0$

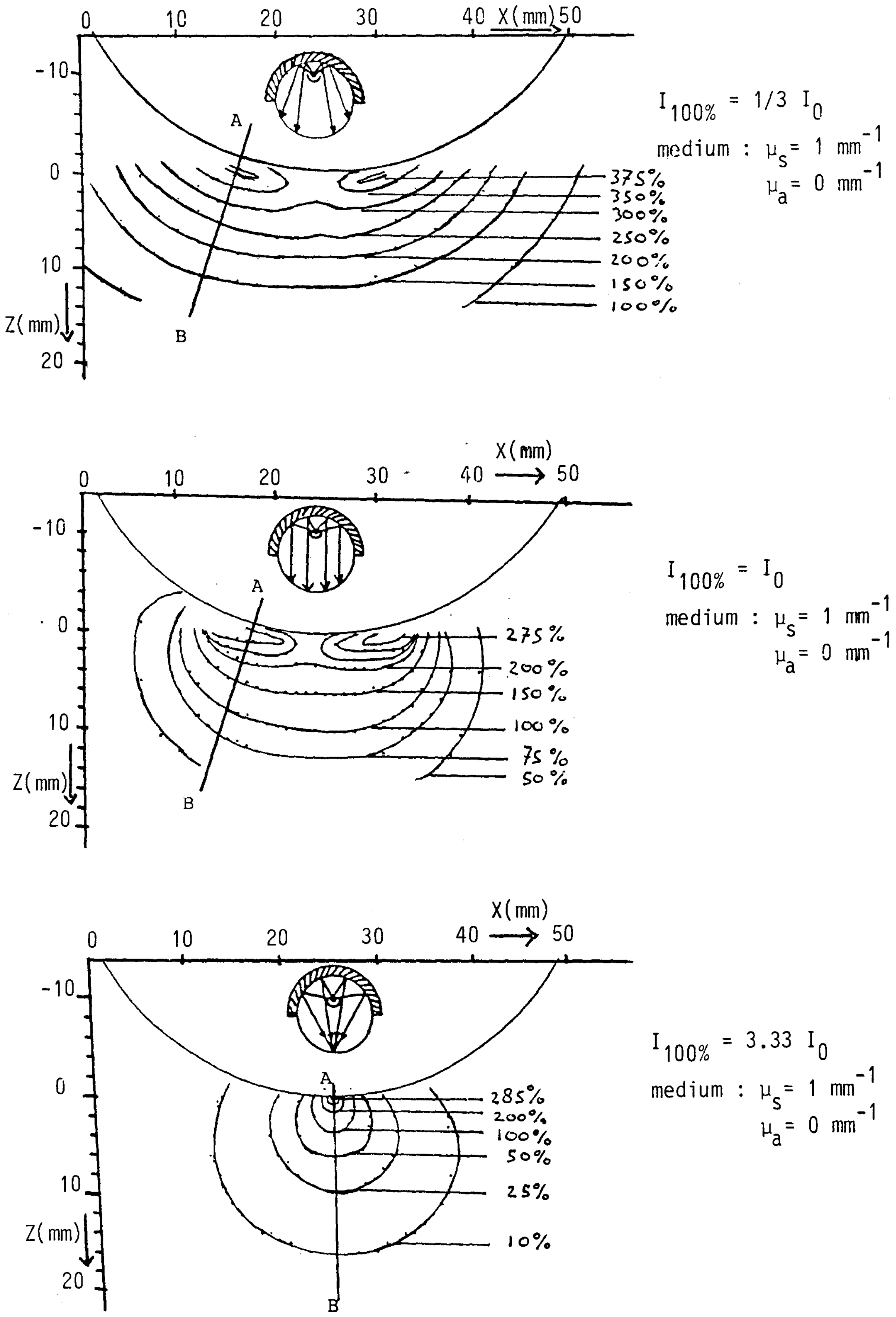

$I_{100\%} = 1/3\ I_0$

medium : $\mu_s = 1\ \text{mm}^{-1}$

$\mu_a = 0\ \text{mm}^{-1}$

$I_{100\%} = I_0$

medium : $\mu_s = 1\ \text{mm}^{-1}$

$\mu_a = 0\ \text{mm}^{-1}$

$I_{100\%} = 3.33\ I_0$

medium : $\mu_s = 1\ \text{mm}^{-1}$

$\mu_a = 0\ \text{mm}^{-1}$

Fig. III.3.4

Isodoses in a medium

scattering : $\mu_s = 1\ \text{mm}^{-1}$

no absorption : $\mu_a = 0\ \text{mm}^{-1}$

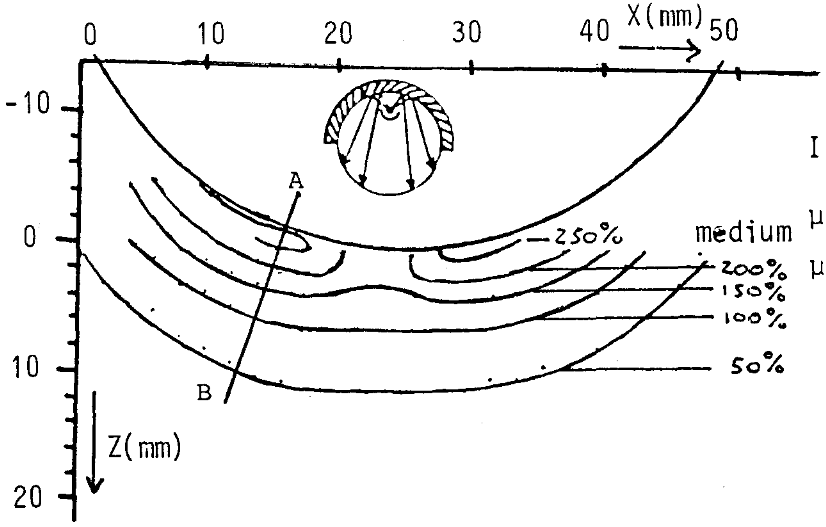

$I_{100\%} = 1/3\ I_0$

medium $\mu_s = 1\ mm^{-1}$

$\mu_a = 0.01\ mm^{-1}$

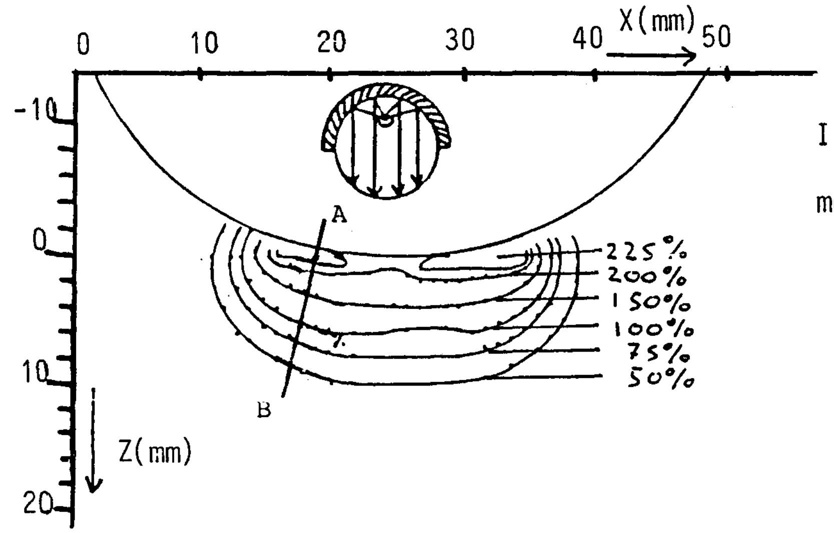

$I_{100\%} = I_0$

medium : $\mu_s = 1\ mm^{-1}$

$\mu_a = 0.01\ mm^{-1}$

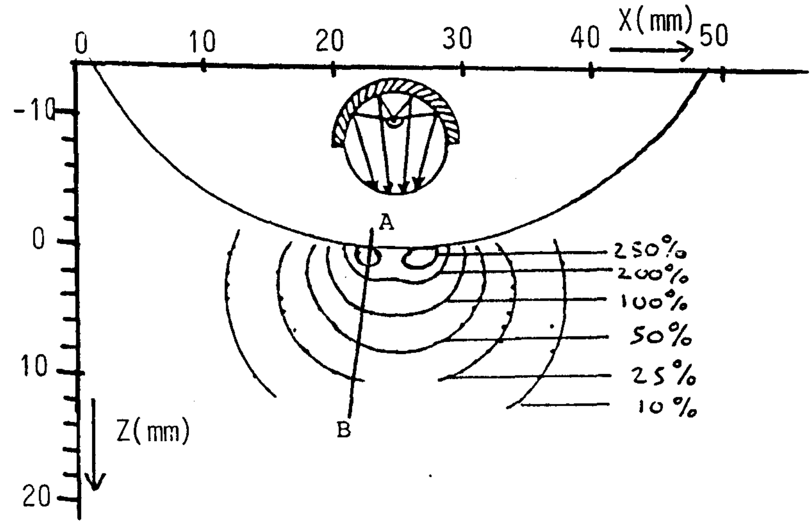

$I_{100\%} = 3.33\ I_0$

medium : $\mu_s = 1\ mm^{-1}$

$\mu_a = 0.01\ mm^{-1}$

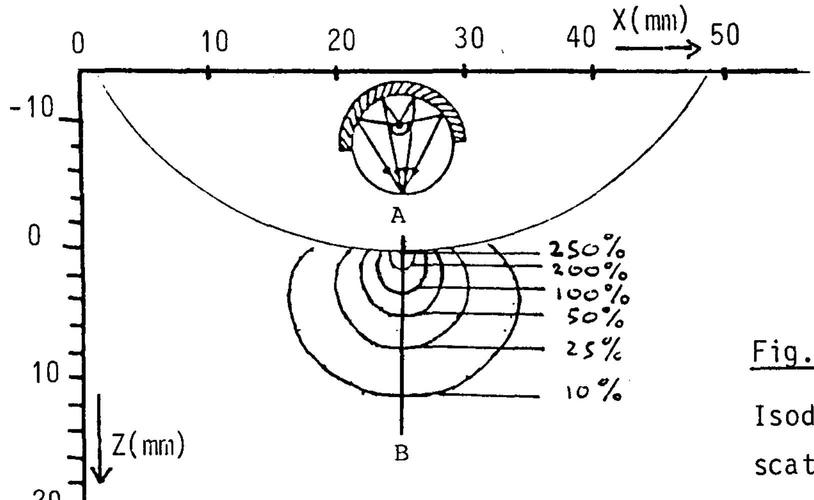

$I_{100\%} = 7\ I_0$

medium : $\mu_s = 1\ mm^{-1}$

$\mu_a = 0.01\ mm^{-1}$

Fig. III.3.5

Isodoses in a medium

scattering : $\mu_s = 1\ mm^{-1}$

little absorption : $\mu_a = 0.01\ mm^{-1}$

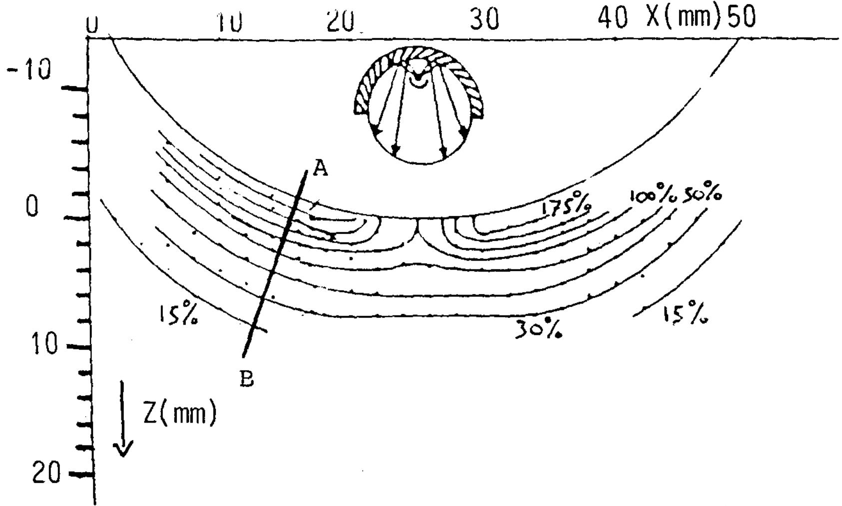

$I_{100\%} = 1/3\ I_0$

medium : $\mu_s = 1\ \mathrm{mm}^{-1}$

$\mu_a = 0.05\ \mathrm{mm}^{-1}$

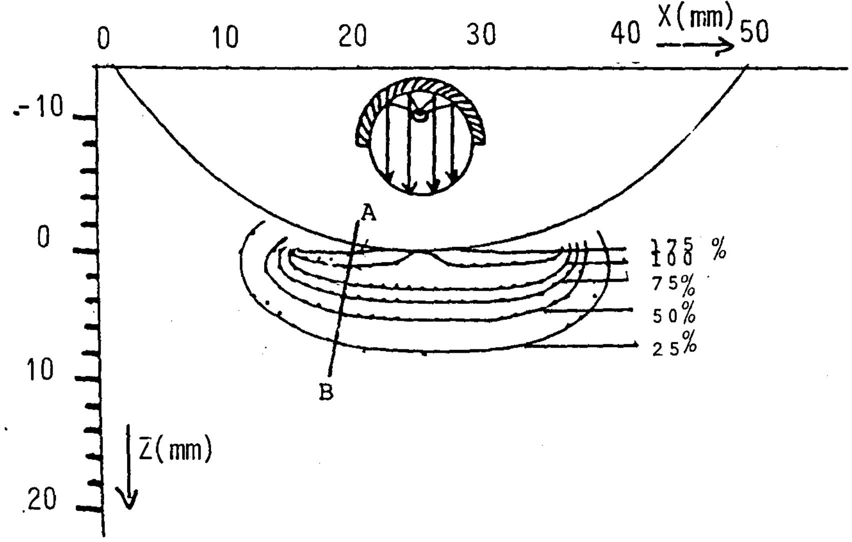

$I_{100\%} = I_0$

medium : $\mu_s = 1\ \mathrm{mm}^{-1}$

$\mu_a = 0.05\ \mathrm{mm}^{-1}$

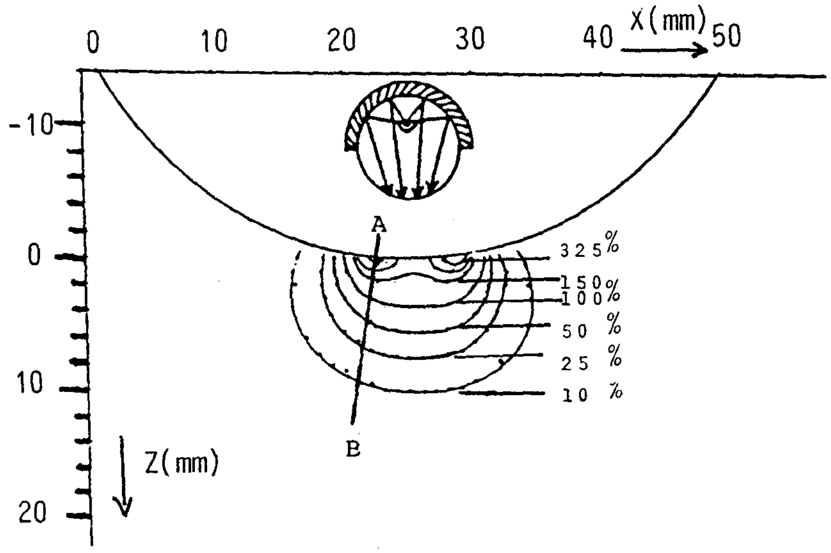

$I_{100\%} = 3.33\ I_0$

medium : $\mu_s = 1\ \mathrm{mm}^{-1}$

$\mu_a = 0.05\ \mathrm{mm}^{-1}$

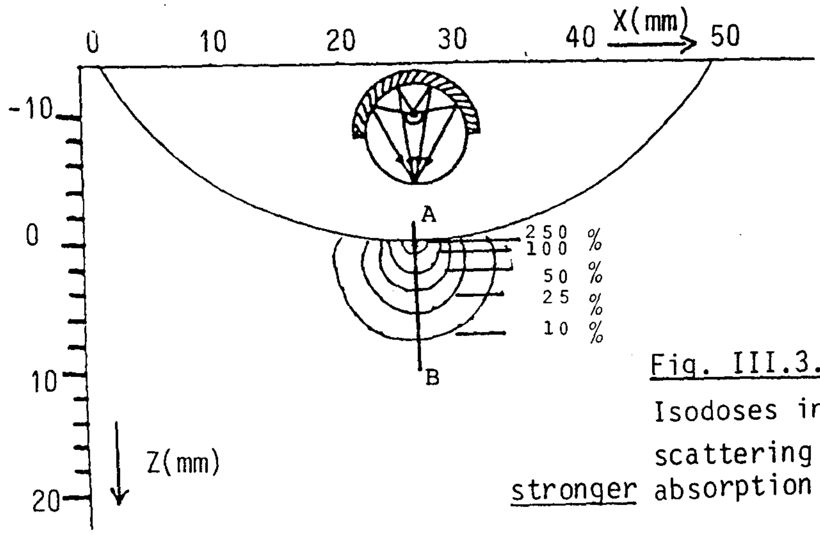

$I_{100\%} = 7\ I_0$

medium : $\mu_s = 1\ \mathrm{mm}^{-1}$

$\mu_a = 0.05\ \mathrm{mm}^{-1}$

Fig. III.3.6

Isodoses in a medium

scattering : $\mu_s = 1\ \mathrm{mm}^{-1}$

stronger absorption : $\mu_a = 0.05\ \mathrm{mm}^{-1}$

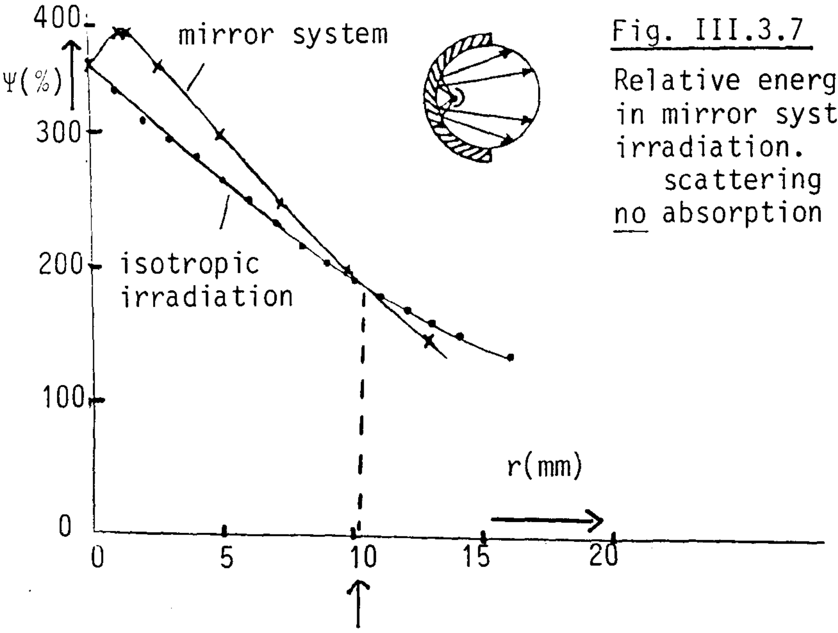

Fig. III.3.7

Relative energy fluence rate measured in mirror system compared with isotropic irradiation.

scattering : $\mu_s = 1\ \text{mm}^{-1}$

no absorption : $\mu_a = 0\ \text{mm}^{-1}$

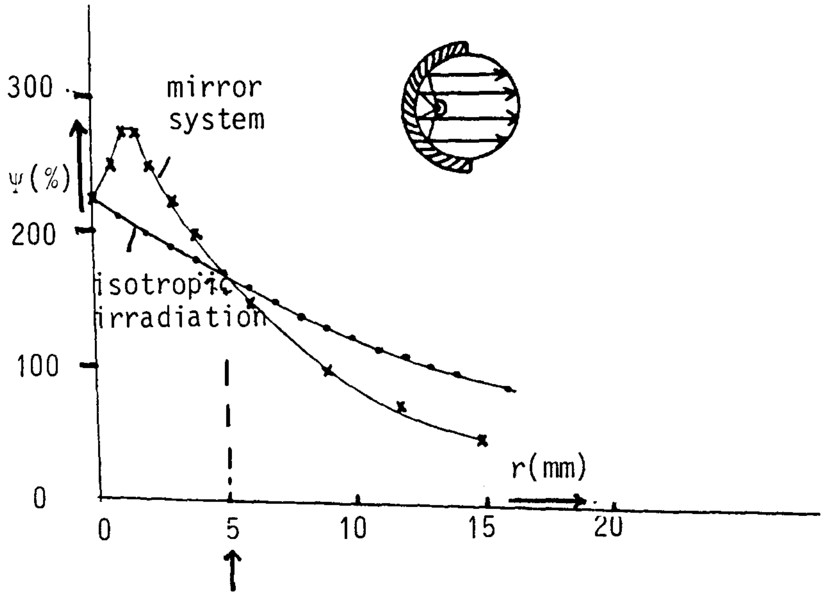

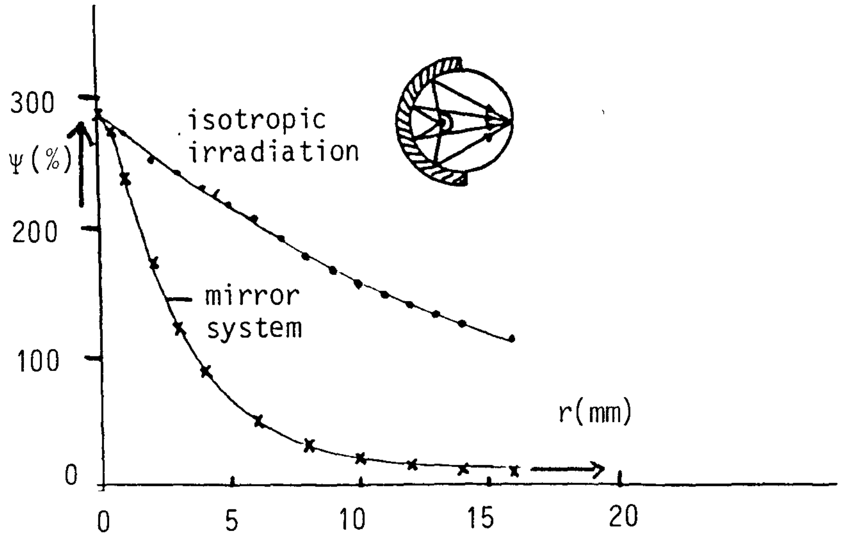

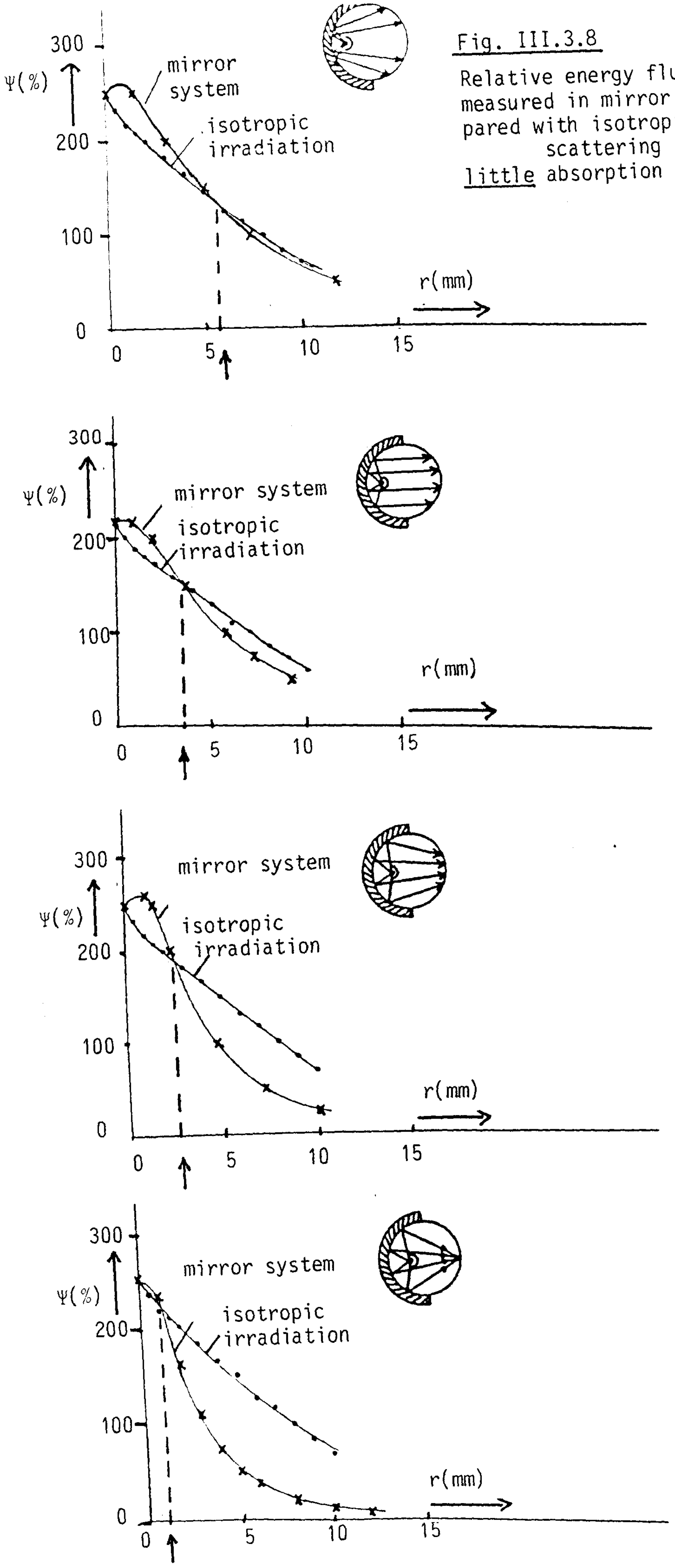

Fig. III.3.8

Relative energy fluence rate measured in mirror system compared with isotropic irradiation.
scattering : $\mu_s = 1\ \mathrm{mm}^{-1}$
little absorption : $\mu_a = 0.01\ \mathrm{mm}^{-1}$

Fig. III.3.9

Relative energy fluence rate measured in mirror system compared with isotropic irradiation.

scattering : $\mu_s = 1\ \mathrm{mm}^{-1}$

stronger absorption : $\mu_a = 0.05\ \mathrm{mm}^{-1}$

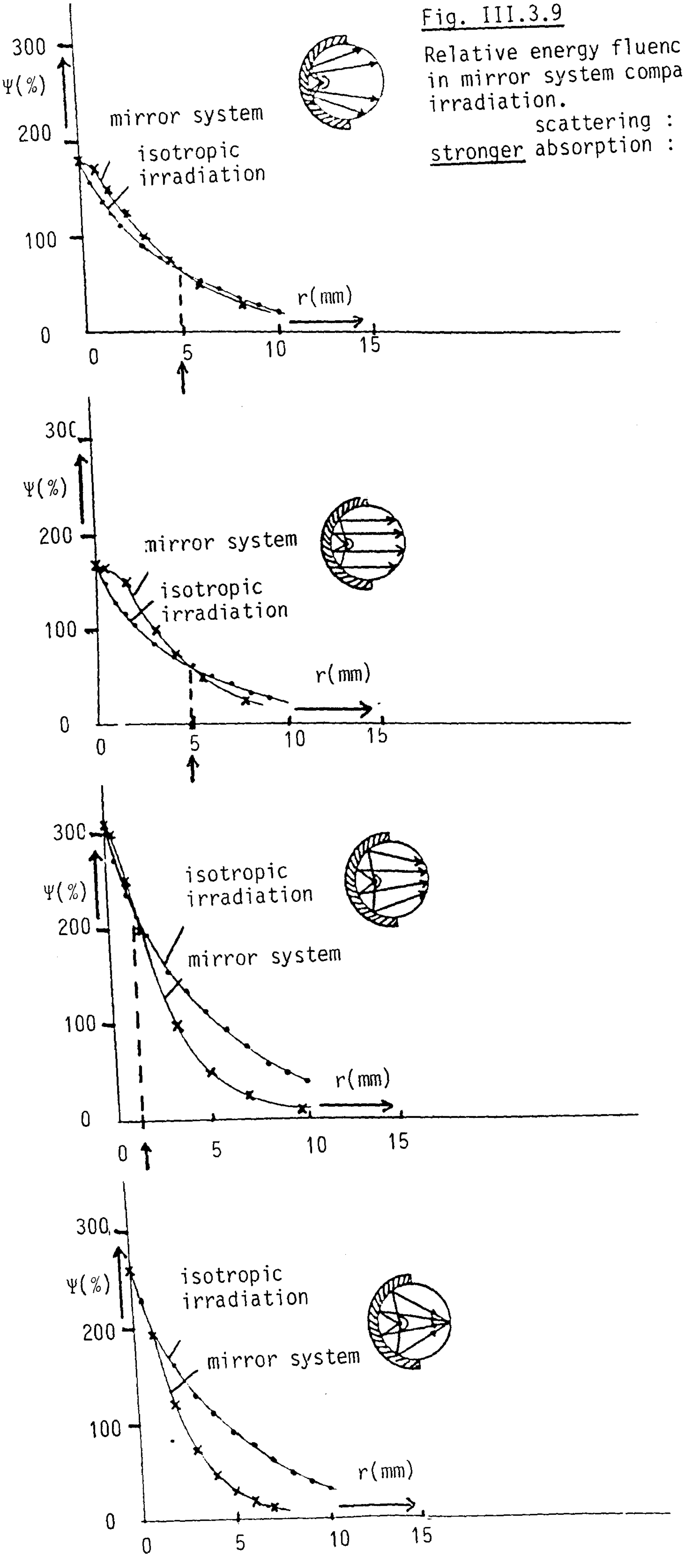

III.4 Discussion.

In this chapter we will discuss the results from the previous paragraph successively.

First we have to look to the results of the system with isotropic irradiation (see fig. III.3.2). We see that the measurements (single points) are in good agreement with the theoretical curve (solid line), except for the measurements with pure Intralipid ($\mu_s = 1\ \mathrm{mm}^{-1}$, no absorber added). This difference, however, can possibly be explained by a too big normalization factor for these measurements. Also we can notice the absence of a maximum which is predicted by the theory. This absence of a maximum is possibly due to the finite size of the isotropic tip of the detecting fibre; in fact this tip is a little sphere (radius r = 0.45 mm) which integrates over a certain area, and a rather subtile maximum could be spreaded out.

Second, we look at the patterns of the incident beams, shown in fig. III.3.3. To explain this pattern we have to look at fig. III.4.1.

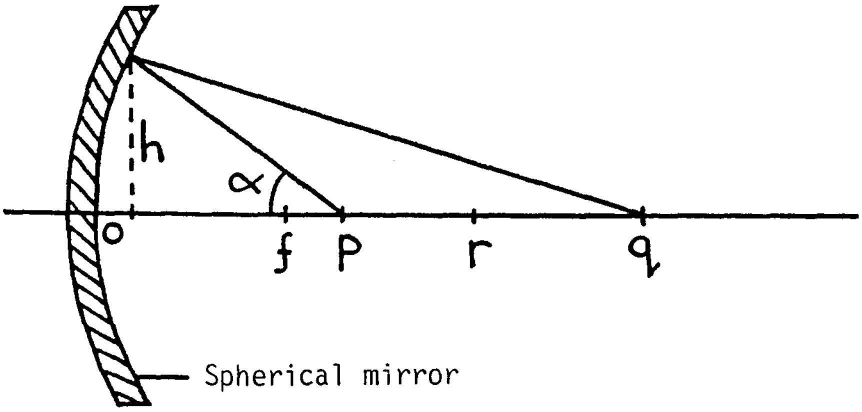

Fig. III.4.1: Reflection at a sphere.

$f = \frac{r}{2}$ = focus of the sphere.
p = object distance
= image distance
h = distance to the symmetry axis
= ptan α

Reflection at a spherical mirror can be expressed by the formula of Descartes:

$$\frac{1}{p} + \frac{1}{q} = \frac{2}{r} \qquad \text{(III.4.1)}$$

If a point source is placed in the focus, a parallel beam will be the result.

This formula, however, is only valid at small opening angles α ; at greater angles we have to make a correction and eq. (III.4.1) becomes [Alonso and Finn, vol. 3]:

$$\frac{1}{p} + \frac{1}{q} = \frac{2}{r} + \frac{h^2}{r}\left(\frac{1}{r} - \frac{1}{p}\right)^2 \qquad \text{(III.4.2)}$$

With eq. (III.4.2) the reflection at a spherical mirror can be simulated theoretically; the results are presented in fig. III.4.2.
Shown are the light rays from a point source in regular steps 10^{o}; the accessory light pattern was estimated by adding the number of rays per unit length of the x-axis. Comparing the theoretical results of fig. III.4.2 with the measured results of fig. III.3.3, we see a rather good agreement. Besides the similarity in the pattern there is also good agreement for the width of the beam, which in the case of the beam is approx. 20 mm. It is obvious that the small dip in the middle of the of the measured patterns is caused by the little mirror behind the isotropic radiating tip.

We must conclude that the difference in the pattern of the incident beam between a spherical mirror and a parabolical mirror is apparently substantial and can influence the final result.

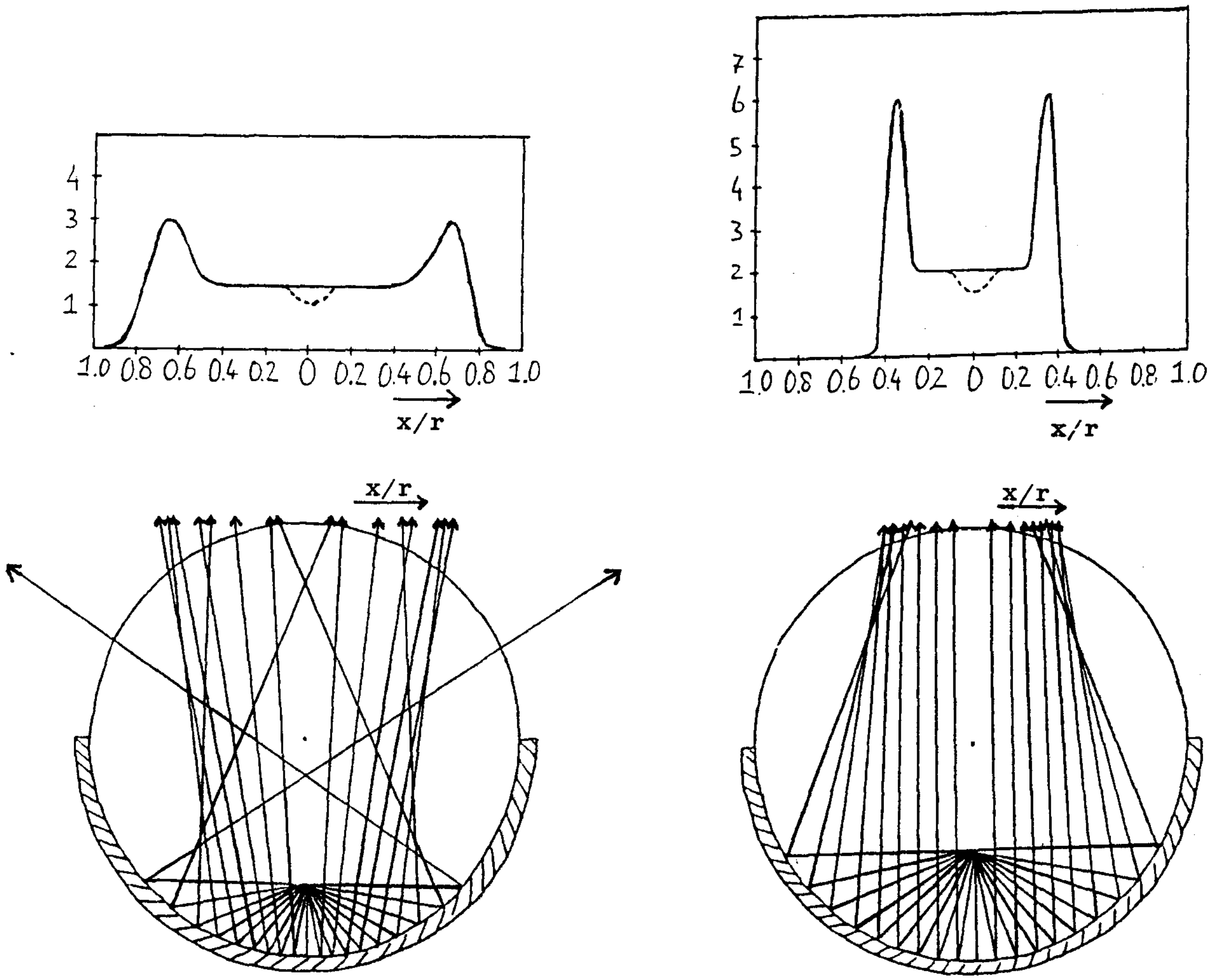

A diverging beam

B parallel beam

Fig. III.4.2: Theoretical construction of the incident light pattern of the mirror systrem (r = 27 mm).

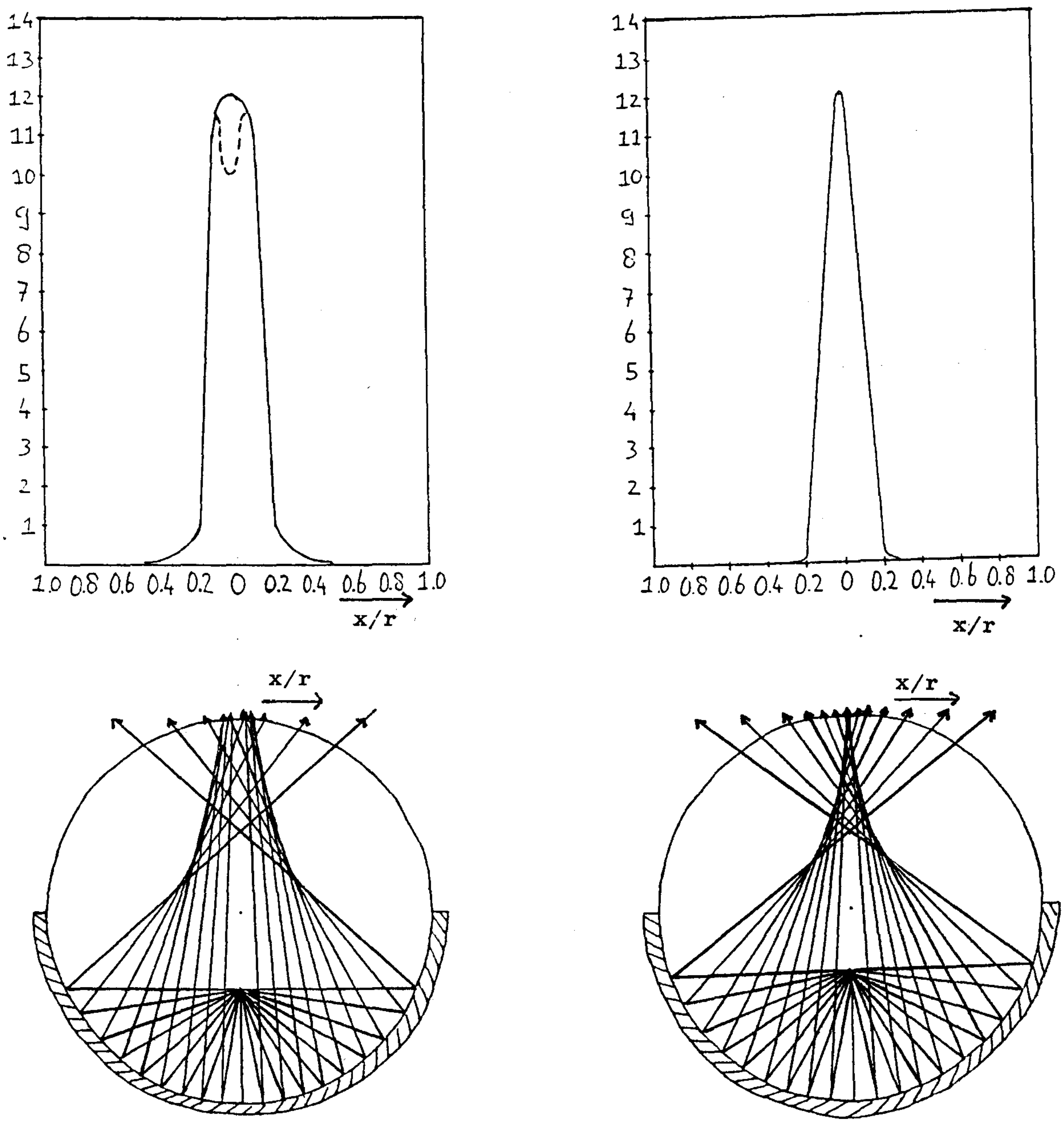

C focussed beam

D focussed beam

Fig. III.4.3: Theoretical construction of the incident light pattern of the mirror system (r = 27 mm).

Looking at the results for the mirror system placed in a scattering and absorbing medium in figures III.3.4 to III.3.6, we see that there are rather different resulting light patterns between the several incident beams. For a diverging and a parallel beam there exists a dip in the pattern which disappears for the focussed beam.

Finally we have to look at the comparison between the results for the mirror system and the isotropic irradiation system, shown in the figures III.3.7 to III.3.9.

For a medium with only scattering, no absorber added, the mirror system is better than the isotropic irradiation system only within a small distance.

The diverging beam is slightly better than the parallel beam, the focussed beam is worse everywhere.

Adding some absorber to the medium (figures III.3.8 and III.3.9) makes the result even worse, although again the diverging beam penetrates deeper than the focussed beam.

An interesting point is that the decrease of the mirror system is sharper at large radii than the decrease of the isotropic irradiation system, in contradiction with our expectations (par. III.2).

Apparently the wide beam approximation is not valid for this mirror system; a cause is probably the too small width of the incident beam in fig. III.3.3 (approx. 20 mm for the parallel beam). We have found strong evidence for this explanation in chapter IV, par.IV.4 .

The final conclusion with regard to the brain tissue phantom experiments is that with the developed instrument we cannot receive a deeper penetration of light inside the medium. Only at small distances we observe a higher energy fluence rate, but the decrease is sharper at larger radii than with the isotropic irradiation system.

IV. Penetration depths as a function of beam diameter: experiments and theory.

IV.1 Introduction.

In this chapter we will investigate the conditions for which the wide beam approximation is valid; in particular the influence of the beam diameter on the light penetration will be studied. This influence of beam diameter is of interest in PDT because it can strongly influence the penetration depth of the light in the tissue and consequently the result of the treatment.

Another point of interest is that these measurements together with well-defined optical parameters (see par. II.5) allow a comparison with the theoretical finite diameter solution of par. I.4.

Finally we will try to find evidence that the deviation of the results from the mirror-system (see chapter III) from the wide beam solution is caused by the fact that the beam diameter was too small, (the diameter was approx. 20 mm, see fig. III.3.3).

IV.2 Experimental set-up.

For our measurements we used the experimental set-up shown in fig. IV.2.1.

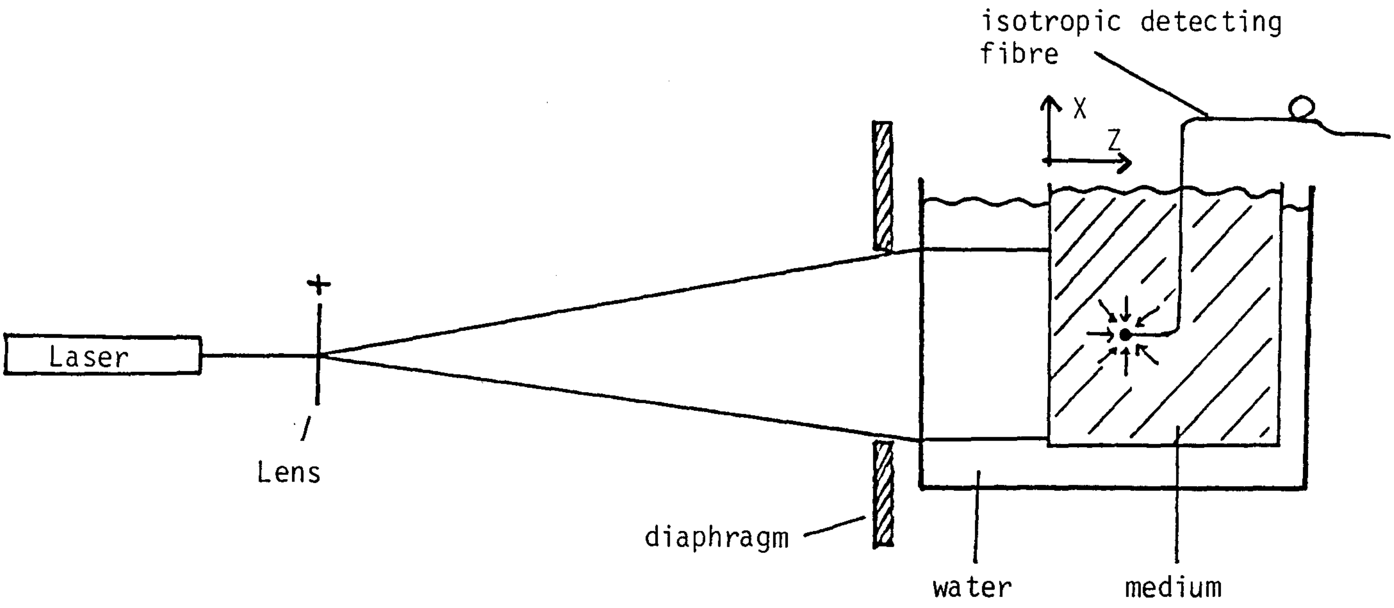

Fig. IV.2.1: Experimental set-up for finite diameter beam measurements.

A laser beam is directed to a microscope object-lens (f = 10 mm), diverged and after passing through a circular diaphragm directed to a tank filled with a scattering and absorbing medium. In part of our experiments this tank filled with medium was surrounded by a tank filled with water to realize index-matching (see fig. IV.2.2), in the other part of our experiments this was omitted to investigate the influence of the boundaries.

When the medium is irradiated by a beam of light, part of the energy flux will leave the medium in the negative z-direction (see fig. IV.2.2).
For a water-air boundary the critical angle for total reflection θc is 48°; the experimental set-up for index-matching was constructed in such a way that light leaving from the middle of the tank filled with medium under the critical angle θc reached the front of the watertank just in the corner (see fig. IV.2.2).

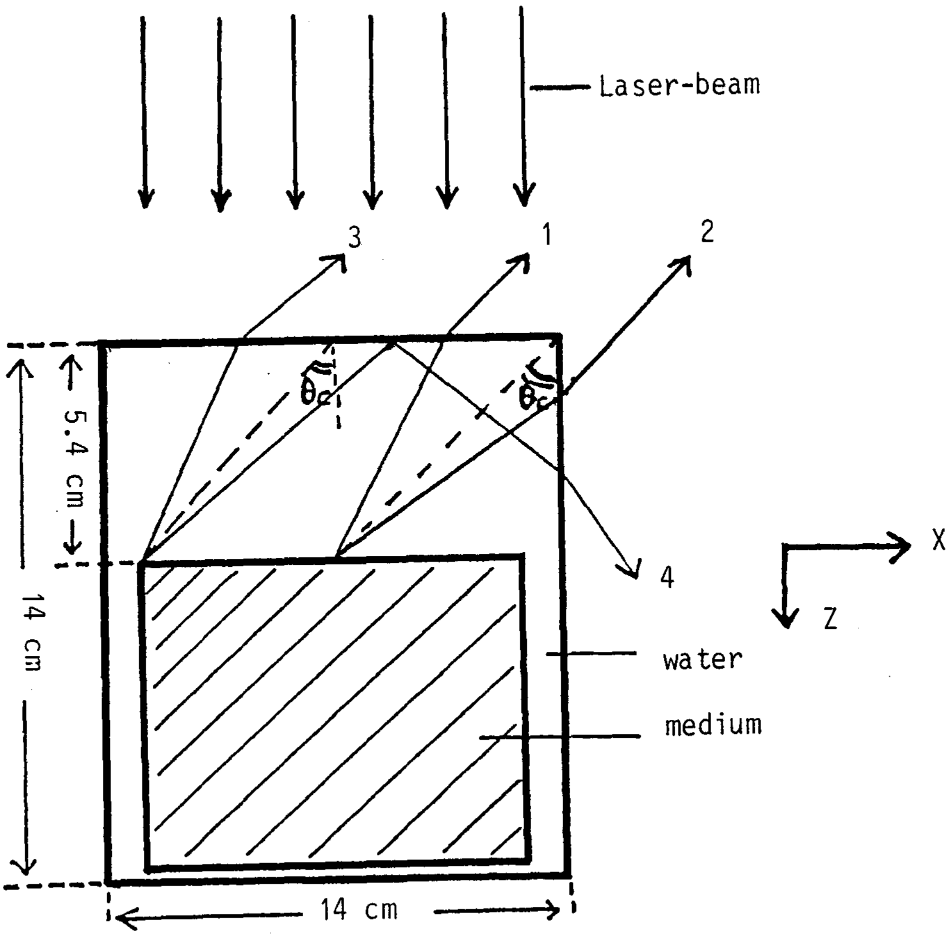

Fig. IV.2.2: Experimental set-up to realize index-matching.

Light beams leaving the medium and reaching the front under an angle smaller than the critical angle (e.g. beams 1 and 3) will be transmitted through the boundary; the reflected part is negligible (see also par. I.2.4, fig. I.2.4). Light beams leaving the medium at larger angles will reach the side of the watertank (directly like beam 2 or via total reflection at the front like beam 4) also at angles smaller than the critical angle θc and will likewise be transmitted.

In this way index-matching could be realized.

Another point of importance is that the finite beam solution was developed for a parallel incident beam, while we have a diverging beam (see fig. IV.2.3).

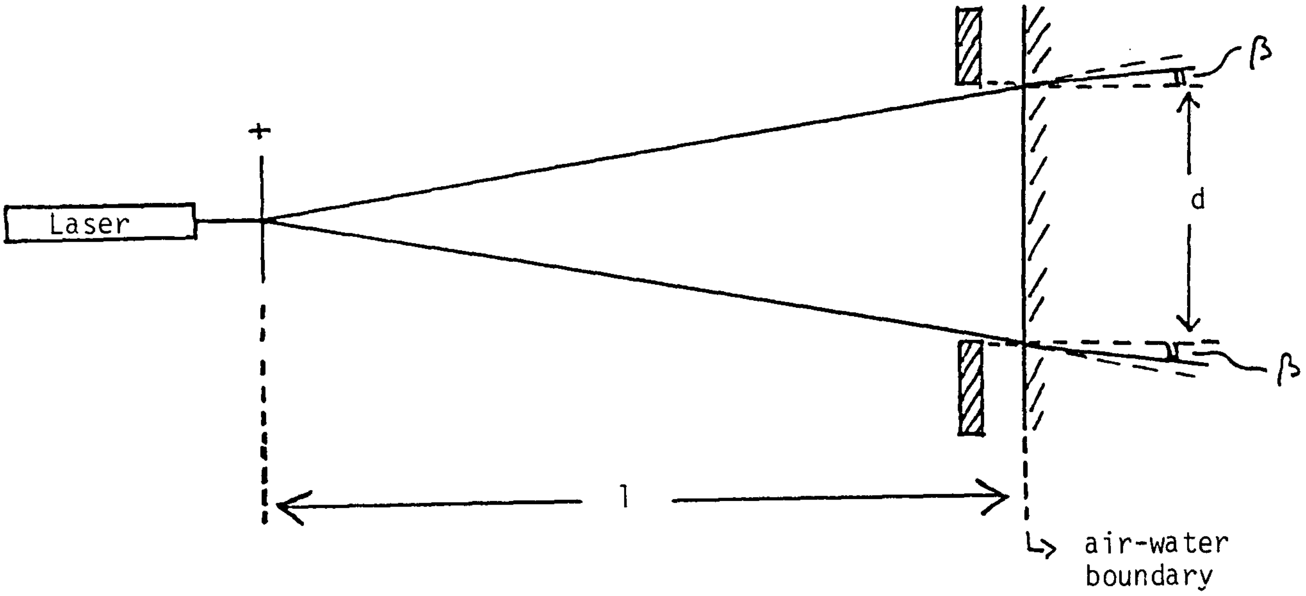

Fig. IV.2.3: Experimental set-up for construction of a parallel beam.

However, it can be shown by simple geometry that the maximum angle of deviation (β) from a parallel incident beam (see fig. IV.2.3) is given by:

$$\tan \beta = \frac{d}{2n_2 l} \qquad \text{(IV.2.1)}$$

where d is diameter of diaphragm

1 is distance between object-glass and air-water boundary (1 = 140 cm)

n_2 is index of refraction of the medium (for water n_2 = 1.33).

In the set-up we used the maximum diameter of the diaphragm was d = 9 cm, and the corresponding maximum deviation ange was $\beta_{max} = 1.4^{o}$, which is rather small. Therefore this experimental set-up was considered adequate for our purposes.

To reduce the amount of measurements we measured only in the middle of the beam from the medium-water boundary or medium-air boundary in the z-direction (see fig. IV.2.2).

IV.3 Results.

First we measured the profile of the incident beam in pure water; the results are shown in fig. IV.3.2.

In fig. IV.3.3 the results are shown from the finite beam diameter measurements in the case of index-matching, together with the results of computer calculations, based on the finite diameter solution of par. I.4, for several optical parameters.
The vertical axis gives the energy fluence rate inside the medium with respect to the incident energy fluence rate taken 100 per mm^2. The horizontal axis gives the depth z inside the medium in mm, measured from the boundary of the medium.
For the experiments we used mixtures of Intralipid from the St. Joseph Hospital and Evans Blue.
Fig. IV.3.4 gives the same measurements as those in fig. IV.3.3, but now in the case of a medium-air boundary.

A few words have to be said concerning the measurement of the energy fluence rate inside the medium with respect to the calibration measurements in water of the incident beam.
Consider the isotropic tip shown in fig. IV.3.1A, with surface area A.
In an ideal situation this whole surface area A will be illuminated. However, when the energy fluence rate inside the medium is measured experimentally, that part of the tip which is connected to the fibre with cross section a will not be illuminated (see fig. IV.3.1A).

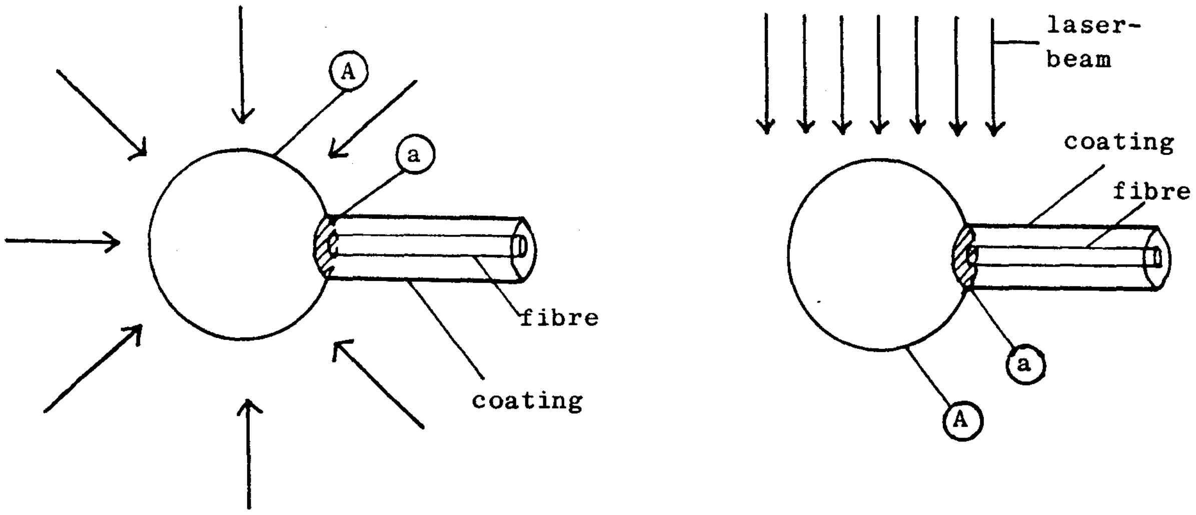

A. Energy fluence rate measurement

B. Calibration measurement

Fig. IV.3.1.

This disturbance caused by the connection of the tip to the fibre does not appear for the calibration measurements, because in this case the fibre is directed perpendicularly to the incident laser beam (see fig. IV.3.1B). So we have to adjust the relative energy fluence rate measurements inside the medium with a factor A/(A-a) to correct for this connection part.

In our case (with tip diameter d_{tip} = 0.9 mm and fibre diameter d_{fibre} = 0.65 mm) the correction factor is A/(A-a) ~ 1.15.

The results in figs. IV.3.3 and IV.3.4 were multiplied by this correction factor.

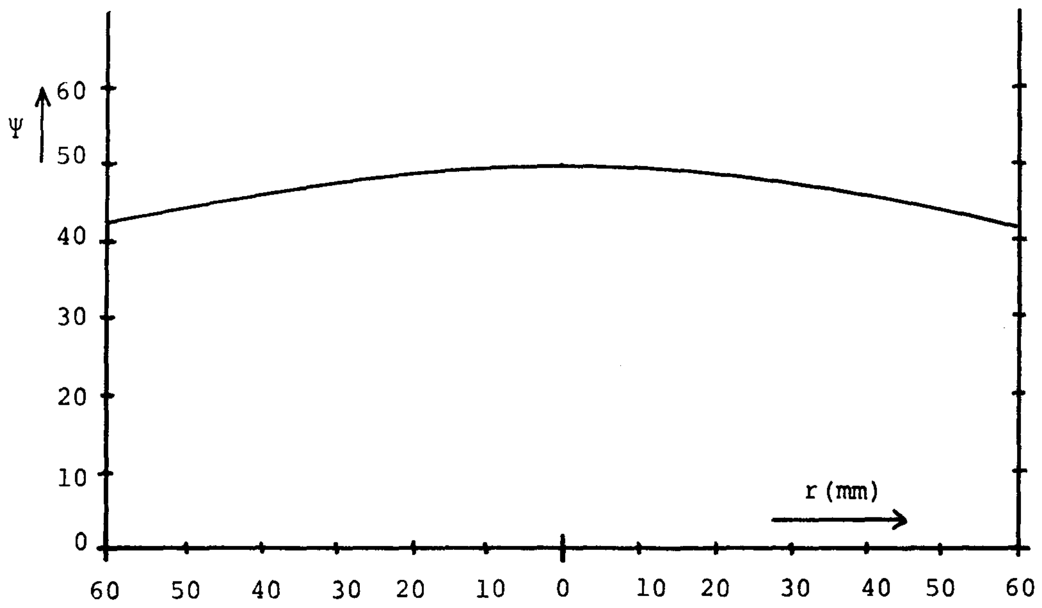

Fig.IV.3.2: Profile of the incident beam.

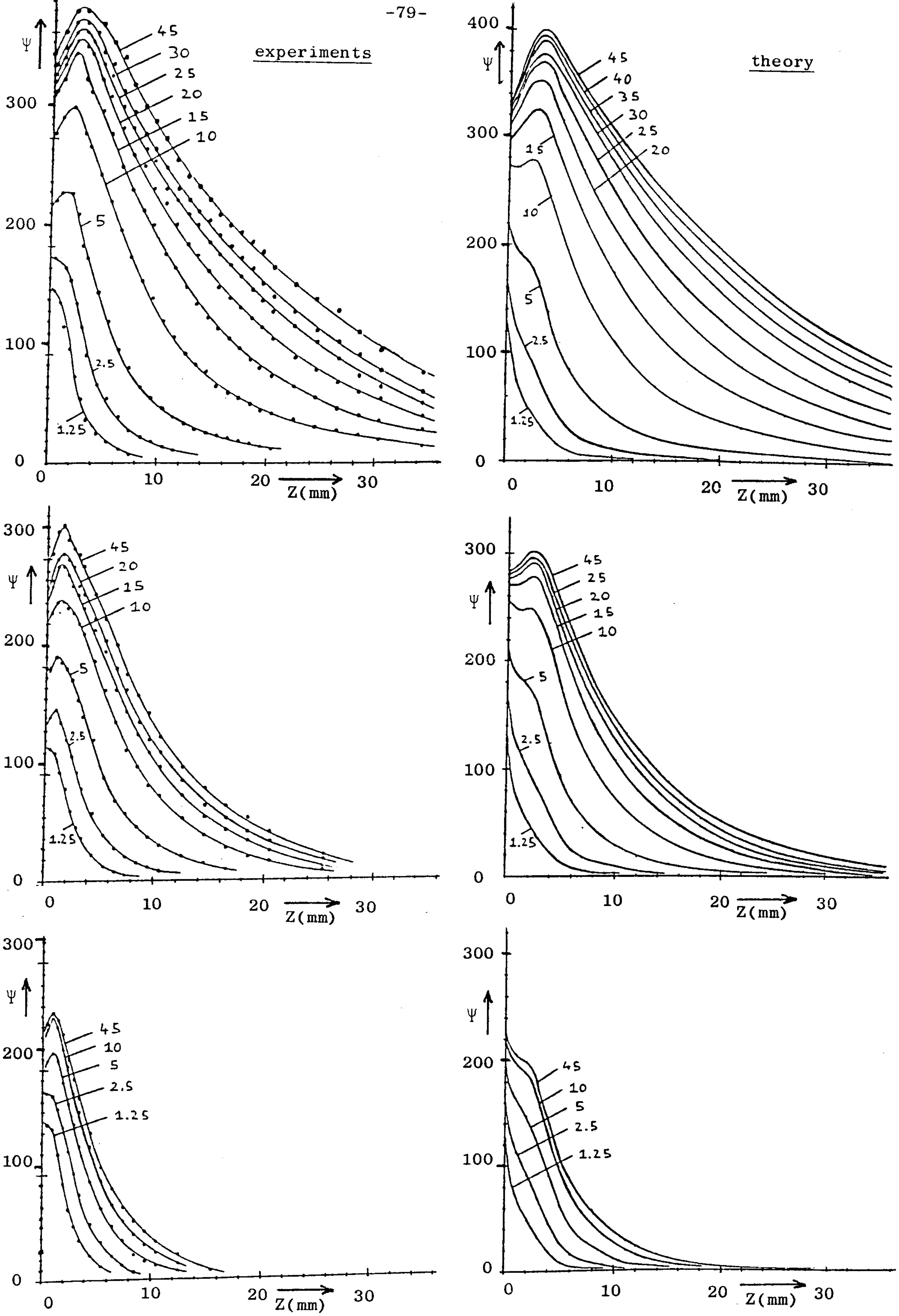

Fig. IV.3.3: Finite diameter beam measurements together with computer calculations in the case of index-matching for several radii of incident beams in mm; Ψ_{inc} = 100.
We used mixtures of Intralipid from the St.Joseph Hospital and Evans Blue.

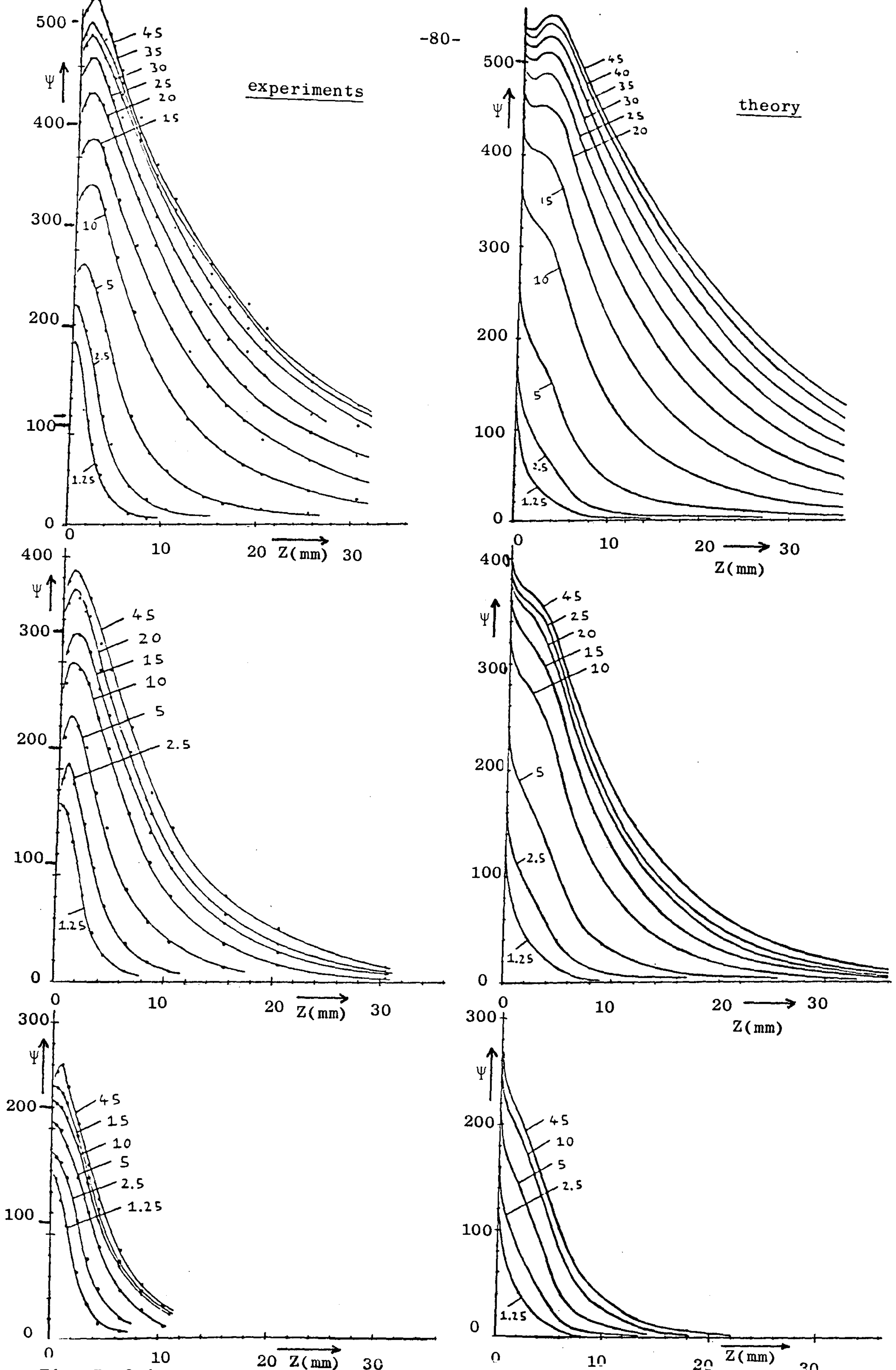

Fig. IV.3.4: Finite diameter beam measurements together with computer calculations in the case of a medium-air boundary for several radii of incident beams in mm; $\Psi_{inc} = 100$.
We used mixtures of Intralipid from the St.Joseph Hospital and

IV.4 Discussion.

When we look at the profile of the incident beam (fig. IV.3.2) we see that although the profile is Gaussian, the deviation from a uniform profile is small and therefore the profile was considered adequate for our purposes.

From the finite beam diameter measurements (figs. IV.3.3 and IV.3.4) we notice a good agreement between measurement and theory, although for small beam diameters there seems to be a deviation which possible can be explained by the fact that the beam diameter is in the order of the diameter of the isotropic detector (d_{tip} = 0.9 mm).
Comparing the results for index-matching (fig. IV.3.3) with those in the case of a medium-air boundary (fig. IV.3.4) we notice a larger energy fluence rate in the latter case; this is due to the diffuse back reflection in the case of a medium-air boundary, which consequently determines the boundary conditions (see par. I.2.4).
From all results it is clear that the size of the beam diameter has a large influence on the energy fluence rate inside the medium.
Looking at the results for an incident beam with a radius of 10 mm (comparable with the parallel beam of the mirror system in ch. III, see fig. III.3.3), we can notice a considerable deviation from the wide beam results (with a radius of 45 mm). Therefore it is likely correct to assume that the deviation from the wide beam solution for the mirror system in ch. III is caused by the too small beam diameter.

V. Proposal for a (semi-)invasive in-vivo determination of optical parameters.

V.1. Introduction.

One of the main problems in Photodynamic Therapy (PDT) is the prediction of the light distribution in the tissue (see the Introduction of this report). Essential for this prediction is knowledge of the tissue parameters, namely the absorption coefficient μ_a, scattering coefficient μ_s and asymmetry parameter g, assuming the diffusion approximation to be valid.

One of the methods for determination of all three parameters is the integrating sphere method [Splinter, 1987]. Other methods have been described by e.g. [Marijnissen and Star, 1987] and by [Wilson et al. 1987]. All these methods are in-vitro methods with the disadvantage that the optical parameters can change substantially with respect to in-vivo conditions.

V.2. Theory and discussion.

In chapter II we measured the optical parameters of Intralipid and Evans Blue separately; the method used in that chapter, however, cannot be used for tissues which possess both scattering and absorption. The method in chapter II concentrated on determination of μ_a, μ_s and g.

In chapter I, however, we defined optical parameters related to μ_a, μ_s and g, namely the linear attenuation coefficient μ_t, the linear transport coefficient μ_{tr} and the effective attenuation coefficient μ_{eff} (see also appendix A) where

$$\mu_t = \mu_a + \mu_s \tag{V.2.1}$$

$$\mu_{tr} = \mu_a + (1-g)\,\mu_s \tag{V.2.2}$$

$$\mu_{eff} = (3\,\mu_a\,\mu_{tr})^{\frac{1}{2}} \tag{V.2.3}$$

Conversely, μ_a, μ_s and g are given by

$$\mu_a = \frac{\mu^2_{eff}}{3\,\mu_{tr}} \tag{V.2.4}$$

$$\mu_s = \mu_t - \frac{\mu^2_{eff}}{3\,\mu_{tr}} \tag{V.2.5}$$

$$g = 1 - \frac{3\,\mu^2_{tr} - \mu^2_{eff}}{3\,\mu_t\,\mu_{tr} - \mu^2_{eff}} \tag{V.2.6}$$

Consequently, the optical parameters μ_a, μ_s and g can be found by determination of the parameters μ_t, μ_{tr} and μ_{eff}.

The linear transport coefficient μ_{tr} and the effective attenuation coefficient μ_{eff} can <u>both</u> be determined invasively by using the solution for a point source in an infinite (or bulk-)medium, (eq. I.5.3):

$$\psi\,(\hat{r}) = \frac{3\,\mu_{tr}P}{4\pi\,r}\exp(-\,\mu_{eff}r) \tag{I.5.3}$$

with $P = \frac{P_o}{4}$

Using eq. I.5.3, we find for μ_{eff}

$$\mu_{eff} = -\,\frac{\partial\,\ln(\,\psi\cdot r)}{\partial\,r} \tag{V.2.7}$$

which is the slope in a $\ln(\Psi \cdot r)$ versus r-diagram (see also par. II.3).

Once μ_{eff} is found, we can find μ_{tr} from eq. I.5.3 by

$$\mu_{tr} = \frac{1}{C_o} \left(\frac{\partial \ln \Psi}{\partial P}\right)_{r_o} \qquad (V.2.8)$$

$$\text{where } C_o = \frac{3}{4\pi} \frac{1}{r_o} \exp(-\mu_{eff} \cdot r_o) \qquad (V.2.9)$$

and r_o = distance to the point source.

Thus, μ_{tr} is determined by the slope of a $\ln \Psi$ versus P-plot at point r_o. In practice this means that in addition to determination of the energy fluence rate Ψ as a function of radius r to find μ_{eff}, at each radius inside the medium the incident power P must be varied to determine μ_{tr}. The advantage of this method is that both measurements can be done at the same time.

The last parameter μ_t still has to be found by an inlvitro method by using a slab of tissue and detecting the transmitted light (see also par. II.3.2B). For light transmitted through a scattering and absorbing slab of tissue of thickness d and detected under a small angle (see also fig. II.3.8) we may write

$$\Psi = \Psi_o \exp(-\mu_t d) \qquad (V.2.10)$$

where Ψ_o is incident fluence rate

Ψ is transmitted fluence rate

μ_t is total attenuation coefficient

$(\mu_t = \mu_a + \mu_s)$

d is thickness of the slab

From eq. (V.2.10) we can find μ_t by

$$\mu_t = \frac{1}{d} (\ln \Psi - \ln \Psi_o) \qquad (V.2.11)$$

If a method can be found to determine the total attenuation coefficient μ_t in vivo, this method could be fully invasive.

One of the problems of the method presented above is proper determination of the constant C_o (see eq. V.2.9), which is needed to determine μ_{tr}. Especially accurate detection of the related radius r_o is essential.
For brain tissue (with optical parameters in the order of $\mu_a = 0.15\ mm^{-1}$, $\mu_s = 5\ mm^{-1}$, $g = 0.7$ [Splinter, 1987] we find for a variation of 0.1 mm in the radius r_o a variation in C^{-1}_o (and consequently in μ_{tr}) of 10-15%. This accurate detection of r_o could possibly be a limitation of the method.

Appendix A

RECOMMENDED NOMENCLATURE FOR PHYSICAL QUANTITIES IN THE MEDICAL APPLICATIONS OF LIGHT

NAME OF QUANTITY	DEFINITION	SYMBOL	UNITS
(linear)absorption coefficient	probability of absorption per infinitesimal path length	μ_a	m^{-1}
(linear)scattering coefficient	probability of scatter per infinitesimal path length	μ_s	m^{-1}
(linear)attenuation coefficient	probability of interaction per infinitesimal path length $\mu_t = \mu_a + \mu_s$	μ_t	m^{-1}
differential scattering coefficient	probability of scatter through a specified angle θ per infinitesimal path length per unit solid angle	$d\mu_s/d\hat{\Omega}$	$m^{-1}sr^{-1}$
scattering phase function	$(2\pi / \mu_s)d\mu_s(\theta)/d\hat{\Omega}$	$S(\cos\theta)$	
single scattering albedo	μ_s/μ_t	a	
mean cosine of scattering angle	$\int_{-1}^{1} S(\cos\theta)\cos\theta d(\cos\theta)$	g	
mean free path	$1/\mu_t$	mfp	m
(linear transport coefficient	$\mu_{tr} = \mu_a + (1-g)\mu_s$	μ_{tr}	m^{-1}
diffusion constant	$D = (3\mu_{tr})^{-1}$	D	m
effective attenuation coefficient	$\mu_{eff} = (\frac{\mu_a}{D})^{\frac{1}{2}}$	μ_{eff}	m^{-1}

specular reflectance	fraction of incident light flux reflected by irradiated surface	R_{sp}
scattered reflectance	fraction of incident light flux scattered through irradiated surface	R_s
(total)reflectance	$R_t=R_{sp}+R_s$	R_t
primary transmittance	fraction of incident flux penetrating without interaction	T_p
scattered transmittance	fraction of incident light flux exiting a surface after scattering at least once	T_s
(total)transmittance	$T_t=T_p+T_s$	T_t
internal reflectance	fraction of light incident from within the tissue reflected back into the tissue	R_i

photon number	number of photons emitted transferred or received	N	
radiant energy	energy of photons emitted transferred or received = $h\nu N$		J
photon flux	dN/dt		s^{-1}
energy flux	$h\nu\, dN/dt$		w
photon fluence	dN/dA where dN photons are incident on a sphere of cross-sectional area dA	ϕ	m^{-2}
energy fluence	$h\nu\, dN/dA$	ψ	Jm^{-2}
photon fluence rate	$d\Phi/dt$	Φ	$m^{-2}s^{-1}$
energy fluence rate	$d\Psi/dt$	Ψ	Wm^{-2}
photon radiance	$d\phi/d$ where $d\phi$ is the photon fluence rate propagating in a specified direction within solid angle $d\Omega$		$m^{-2}s^{-1}sr^{-1}$
(energy)radiance	$d\Psi/d\Omega$	$L(\hat{r},\hat{s})$	$Wm^{-2}sr^{-1}$
photon exposure	dN/dA where dN photons are incident on a plane surface of area dA		m^{-2}
radiant exposure (dose)	$h\nu\, dN/dA$		Jm^{-2}
photon exposure rate (intensity)	$dN/dAdt$		$m^{-2}s^{-1}$
radiant exposure rate	$h\nu\, dN/dAdt$		Wm^{-2}

Appendix B.

We will present here the "transport theory" for the propagation of light in a medium and the diffusion approximation associated with this theory. Also a solution will be given for a beam with finite diameter incident on a medium. This solution was developed by Ishimaru (1978), Reynolds (1975), Groenhuis (1983) and Prahl (1986).

The transport theory is based on the "equation of transport" (Ishimaru, 1978, ch. 7):

$$(\hat{s}.\hat{\nabla})L(\hat{r},\hat{s}) = -\mu_t L(\hat{r},\hat{s}) + \frac{\mu_t}{4\pi} \int_{4\pi} S(\cos\theta)L(\hat{r},\hat{s}')dw' \qquad (B.1)$$

where

$L(\hat{r},\hat{s})$ = energy radiance in $\hat{r}$ in direction $\hat{s}$ ($Wm^{-2}sr^{-1}$)

μ_a = absorption coefficient (m^{-1})

μ_s = scattering coefficient (m^{-1})

$\mu_t = \mu_a + \mu_s$ = total attenuation coefficient (m^{-1})

dw' = element of solid angle (sr^{-1})

$\cos\Theta = \hat{s}.\hat{s}'$ = cosine of the angle between $\hat{s}$ and $\hat{s}'$.

$S(\cos\theta)$= phase function representing that part of the photon flux which is scattered from direction $\hat{s}'$ into $\hat{s}$.

In eq. (B.1) the left part is the net rate of change of L in the direction $\hat{s}$:

$$\frac{dL(\hat{r},\hat{s})}{ds} = (\hat{s}.\hat{\nabla})L(\hat{r},\hat{s})$$

The first term on the right side in eq. (B.1) represents the losses due to scattering and absorption, whereas the second term is the gain due to scattering from all directions $\hat{s}'$ into direction $\hat{s}$. This gain depends on the relative probability for scattering of a photon from direction $\hat{s}'$ into direction $\hat{s}$, called the "phase function" $S(\cos\theta)$. There excist many theoretical descriptions of the phase functions (see part I.2.2); we will use "isotropic scattering combined with forward peak":

$$S(\cos\theta) = a\,[(1-g)+2g\,\delta\,(1-\cos\theta)] \qquad (B.2)$$

where $a = \dfrac{\mu_s}{\mu_t}$ = albedo

and g = asymmetry parameter (see par. I.2.2).

Substituting eq. (B.2) into eq. (B.1) we find after some calculations:

$$(\hat{s}\cdot\hat{\nabla})L(\hat{r},\hat{s}) = -\mu_{tr}L(\hat{r},\hat{s}) + \frac{\mu_s'}{4\pi}\int_{4\pi} L(\hat{r},\hat{s}')\,dw' \qquad (B.3)$$

where

$\mu_s' = \mu_s(1-g)$ = reduced scattering coefficient

$\mu_{tr} = \mu_s'+\mu_a$ = transport coefficient

It is convenient to devide the energy radiance $L(\hat{r},\hat{s})$ into two parts, the reduced incident energy radiance $L_{ri}(\hat{r},\hat{z})$ and the remaining diffuse energy radiance $L_d(\hat{r},\hat{s})$, thus

$$L(\hat{r},\hat{s}) = L_{ri}(\hat{r},\hat{z}) + L_d(\hat{r},\hat{s}) \qquad (B.4)$$

Substituting eq. (B.4) into eq. (B.3) we find

$$\frac{d}{dz} L_{ri}(\hat{r},z) = - \mu_{tr} L_{ri}(\hat{r},z) \qquad (B.5a)$$

$$(\hat{s}.\hat{\nabla})L_d(\hat{r},\hat{s}) = - \mu_{tr} L_d(\hat{r},\hat{s}) + \frac{\mu'_s}{4\pi} \int_{4\pi} L_d(\hat{r},\hat{s}')dw'$$

$$+ \frac{\mu'_s}{4\pi} \int_{4\pi} L_{ri}(\hat{r},z)dw' \qquad (B.5b)$$

Note that L_{ri} containes unscattered plus purely forward scattered light (see par. I.2.3).

We will now consider the diffusion approximation, in which we assume that the diffuse part of the radiance consists of (nearly) diffuse radiation (see fig. B.1)

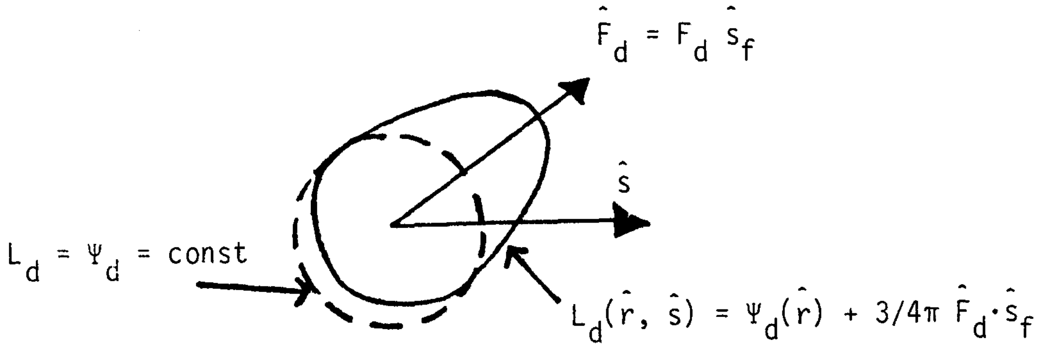

Fig. B.1: Diffuse radiance $L_d(\hat{r},\hat{s})$ for the diffusion approximation. $F_d(\hat{r})$ is the diffuse flux vector in the direction of unit vector $\hat{s}_f$.

For this purpose we define the diffuse energy fluence rate $\Psi_d(\hat{r})$, the reduced incident fluence rate $\Psi_{ri}(\hat{r})$ and the diffuse flux vector $\hat{F}_d(\hat{r})$ as:

$$\Psi_d(\hat{r}) = \frac{1}{4\pi} \int_{4\pi} L_d \, dw \tag{B.6}$$

$$\Psi_{ri}(\hat{r}) = \frac{1}{4\pi} \int_{4\pi} L_{ri} \, dw \tag{B.7}$$

$$\hat{F}_d(\hat{r}) = F_d(\hat{r}) \, \hat{S}_f = \int_{4\pi} L_d(\hat{r},\hat{s}) \, \hat{s} \, dw \tag{B.8}$$

Because Ld(r̂,ŝ) describes nearly diffuse radiation, we may expand it in a Taylor series and truncate it after the first two terms:

$$L_d(\hat{r},\hat{s}) = \Psi_d(\hat{r}) + c \, \hat{F}_d(\hat{r}).\hat{s} \tag{B.9}$$

Substitution of eq. (B.9) into (B.8) will give*):

$$c = \frac{3}{4\pi} \tag{B.10}$$

thus

$$L_d(\hat{r},\hat{s}) = \Psi_d(\hat{r}) + \frac{3}{4\pi} \hat{F}_d(\hat{r}).\hat{s} \tag{B.11}$$

We continue with the derivation of the diffusion equation on the basis of eq. (B.5b) by taking the following two steps:

---

*) For any vector $\hat{A}$ is $\int_{4\pi} \hat{s}(\hat{s}.\hat{A})dw = \frac{4\pi}{3} \hat{A}$

and $\int_{4\pi} \hat{s}[\hat{s}.\hat{\nabla}(\hat{A}.\hat{s})]dw = 0$

1. First, we integrate eq. (B.5b) over 4 of solid angle and together with eq. (B.6) and eq. (B.11) we obtain:

$$\hat{\nabla}\cdot\hat{F}_d(\hat{r}) = -4\pi\,\mu_a\,\Psi_d(\hat{r}) + 4\pi\,\mu_s'\,\Psi_{ri}(\hat{r}) \tag{B.12}$$

2. Second, we multiply eq. (B.5b) by $\hat{s}$ and integrate again over 4π of solid angle to obtain:

$$\nabla\Psi_d(\hat{r}) = -\frac{3}{4\pi}\,\mu_{tr}\,F_d(\hat{r}) + \frac{3}{4\pi}\int_{4\pi}\varepsilon_{ri}(\hat{r},\hat{s})\,\hat{s}\,dw \tag{B.13}$$

where

$$\varepsilon_{ri}(\hat{r},\hat{s}) = \frac{\mu_s'}{4\pi}\int_{4\pi} I_{ri}(\hat{r},z)\,dw' \tag{B.14}$$

Combination of eq. (B.12) and eq. (B.13) and elimination of $F_d(\hat{r})$ yields the "time-independent diffusion equation" for the diffuse energy fluence rate $\Psi_d(\hat{r})$:

$$(\nabla^2 - \mu_{eff}^2)\,\Psi_d(\hat{r}) = -\frac{\mu_s'}{D}\,\Psi_{ri} + \frac{3}{4\pi}\,\nabla\cdot\int_{4\pi}\varepsilon_{ri}\,\hat{s}\,dw \tag{B.15}$$

where

$\mu_{eff}^2 = 3\,\mu_a\,\mu_{tr}$ = effective attenuation coefficient

$D = (3\,\mu_{tr})^{-1}$ = diffusion constant

So far we have neglected the nature of the incident light. Here we will derive a solution for a collimated light beam of finite width perpendicular to the surface of the medium in the z-direction; the beam can be described by:

$$L_{inc}(\hat{r},\hat{s}) = L_o B(r)\ \delta\ (\hat{w}-\hat{z}) \tag{B.16}$$

where L_o = incident irradiance (Wm^{-2})

$B(r)$ = radial distribution of the incident light beam; here we assume

$$B(r) = 1 \quad \text{if} \quad 0 < r < b$$
$$= 0 \quad \text{if} \quad r > b$$

When the indices of refraction are different, L_o has to be multiplied by a factor $1-[(n_{med}-1)^2/(n_{med}+1)^2]$.

We now return to eq. (B.5a) to calculate the reduced incident beam L_{ri}:

$$\frac{d}{dz} L_{ri}(\hat{r},\hat{z}) = -\mu_{tr} L_{ri}(\hat{r},\hat{z}) \tag{B.17}$$

with boundary condition:

$$L_{ri}(\hat{r},\hat{z})\Big|_{z=0} = L_{inc}(\hat{r},\hat{s}) \tag{B.18}$$

The solution of eq. (B.5a) becomes:

$$L_{ri}(\hat{r},\hat{s}) = L_o B(r)\exp(-\mu_{tr}z)\ \delta\ (\hat{w}-\hat{z}) \tag{B.19}$$

Substituting eq. (B.19) in Ψ_{ri} (eq. (B.7)) and ε_{ri} (Eq. (B.14)) we find:

$$\Psi_{ri} = \tfrac{1}{4}\, L_o B(r)\ \exp(-\mu_{tr}z) \tag{B.20}$$

$$\Psi_{ri} = \frac{\mu_s'}{4} L_o B(r)\ \exp(-\mu_{tr}z) \tag{B.21}$$

and

$$\int_{4\pi} \varepsilon_{ri}(\hat{r},\hat{s})\hat{s}\ dw = 0 \tag{B.22}$$

so

$$Q(\hat{r}) = \frac{1}{\mu_{tr}} \int_{4\pi} \varepsilon_{ri}(\hat{r},\hat{s})\hat{s}\, dw = 0 \tag{B.23}$$

Substituting these equations in the diffusion equation (B.15) and in the boundary conditions [eq. (I.2.16), see par. I.2.4] we find for this incident beam:

$$(\nabla^2 - \mu^2_{eff})\, \Psi_d(\hat{r}) = -\frac{\mu'_s}{4D} L_o B(r)\exp(-\mu_{tr} z) \tag{B.24}$$

with boundary conditions:

$$\text{at } z=0 \quad \Psi_d(\hat{r}) - 2DA \frac{\partial}{\partial z} \Psi_d(\hat{r}) = 0 \tag{B.25a}$$

$$\text{at } z=d \quad \Psi_d(\hat{r}) + 2DA \frac{\partial}{\partial z} \Psi_d(\hat{r}) = 0 \tag{B.25b}$$

The differential equation (B.24) can be solved analytically, by using a Greens functions approach. The Greens function $G(\hat{r};\hat{r}')$ has to be a solution of the equation:

$$(\nabla^2 - \mu^2_{eff})\, G(\hat{r},\hat{r}') = \delta(\hat{r}-\hat{r}') \tag{B.26}$$

with boundary conditions

$$\text{at } z=0 \quad G(\hat{r};\hat{r}') - 2DA \frac{\partial}{\partial z} G(\hat{r};\hat{r}') = 0 \tag{B.27a}$$

$$\text{at } z=d \quad G(\hat{r};\hat{r}') + 2DA \frac{\partial}{\partial z} G(\hat{r};\hat{r}') = 0 \tag{B.27b}$$

In cylindrical coordinates eq. (B.26) becomes

$$\left(\frac{1}{r}\frac{\partial}{\partial r}\, r\, \frac{\partial}{\partial r} + \frac{\partial^2}{\partial z^2} - \mu_{eff}^2\right) G(\hat{r};\hat{r}') = \frac{1}{2\pi r}\, \delta\,(\hat{r}-\hat{r}')\delta\,(z-z') \qquad (B.28)$$

The Greens function defined by eq. (B.28) and subject to boundary conditions (B.27) is (see Reynolds, 1975 and Prahl, 1986):

$$G(\hat{r};\hat{r}') = \frac{2}{\pi} \sum_{n=1}^{\infty} \Gamma_n \rho_n(-z)\, \rho_n(z')\, g_n(r;r') \qquad (B.29)$$

where

$$\Gamma_n = k_n/[2k_n d + \sin 2\,\gamma_n - \sin\, 2(k_n d + \gamma_n) \qquad (B.30)$$

$$\rho_n(z) = \sin(k_n z + \gamma_n) \qquad (B.31)$$

$$g_n(r;r') = \begin{cases} I_o(\lambda_n r)K_o(\lambda_n r') & r'>r \\ K_o(\lambda_n r)I_o(\lambda_n r') & r'<r \end{cases} \qquad (B.32)$$

where I_o and K_o are modified Bessel functions.

The eigenvalues k_n are solutions of

$$\tan k_n d = \frac{2(DA)k_n}{(DA)^2 k_n^2 - 1} \qquad (B.33)$$

the function γ_n is

$$\gamma_n = \tan^{-1}(DAk_n) \qquad (B.34)$$

and λ_n is given by

$$\lambda_n^2 = k_n^2 + \mu_{eff}^2 \qquad (B.35)$$

We now consider the following case.

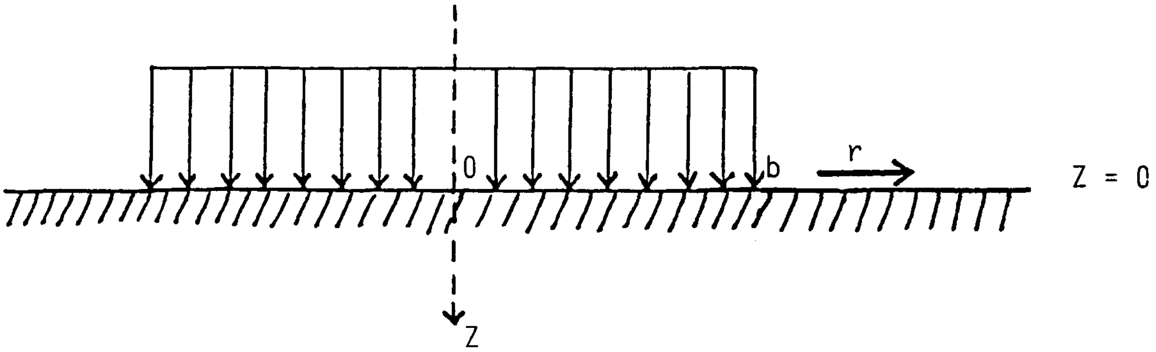

Fig. B.2: Incident beam at z=0

Mathematically we can describe this incident beam as (see fig. B.16):

$$L_{ri} = L_o\, B(r') \exp(-\, \mu_{tr} z') \qquad (B.$$

where $B(r') = \begin{matrix} 1 & \text{if} & 0<r<b \\ 0 & \text{if} & r>b \end{matrix}$

or

$$B(r') = [H(r') - H(r'-b)] \qquad (B.36)$$

with $H(r'-b) = \begin{matrix} 1 & \text{if } r'<b \\ 0 & \text{if } r'>b \end{matrix}$

and H denotes the heaviside step function.

Together with eq. (B.24) and eq. (B.29) we can write:

$$\Psi_d(r,z) = \int_{v'} -\left(\frac{\mu_s'}{4D}\right) L_o B(r')\, G(\hat{r};\hat{r}')\, dv' \qquad (B.37)$$

Using equations (B.29) to (B.35) we can calculate the integral (B.37):

$$\Psi_d(r,z) = L_o\left(\frac{\mu_s'}{4D}\right) \cdot \frac{2}{\pi} \sum_{n=1}^{\infty} \Gamma_n \rho_n(z)$$

$$\int_0^{2\pi} d\theta' \int_0^{d} \rho_n(z') \exp(-\mu_{tr} z')\, dz'$$

$$\int_0^{\infty} [H(r')-H(r'-b)]\, g(r;r')\, r'dr' \qquad (B.38)$$

The first integral gives 2π, the second integral gives

$$\int_0 \sin(k_n z' + \gamma_n) \exp(-\mu_{tr} z')\, dz =$$

$$= z_n[k_n^2 + \mu_{tr}^2]^{-1} \qquad (B.39)$$

where

$$z_n = \sin\gamma_n[\mu_{tr} + \exp(-\mu_{tr} d)(k_n \sin k_n d - \mu_{tr} \cos k_n d) +$$
$$+ \cos\gamma_n[k_n - \exp(-\mu_{tr} d)(\mu_{tr} \sin k_n d + k_n \cos k_n d) \qquad (B.40)$$

The third integral gives:

$$R_n(\lambda_n r) = \begin{cases} \dfrac{1}{\lambda_n^2}[1-\lambda_n b I_o(\lambda_n r) K_1(\lambda_n b)] & \text{if } r<b \\[2ex] \dfrac{b}{\lambda_n}[K_o(\lambda_n r) I_1(\lambda_n b)] & \text{if } r>b \end{cases} \qquad (B.41)$$

Combining equations (B.29) and (B.38) to (B.41) finally gives:

$$\Psi_d(r,z) = \left(\frac{4\mu_s'}{D}\right) L_o \sum_{n=1}^{\infty} \Gamma_n \sin(k_n z + \gamma_n)$$

$$\frac{z_n}{(k_n^2 + \mu_{tr}^2)} R_n(\lambda_n r) \qquad (B.42)$$

where $$\tan k_n d = \frac{2(DA)k_n}{(DA)^2 k_n^2 - 1} \qquad \text{(B.43)}$$

$$\gamma_n = \tan^{-1}(DAk_n) \qquad \text{(B.44)}$$

$$\lambda_n^2 = k_n^2 + \mu^2_{eff} \qquad \text{(B.45)}$$

$$D = (3\,\mu_{tr})^{-1} \qquad \text{(B.46)}$$

Equation (B.42) is in agreement with Reynolds (1975), Ishimaru (1978) and Groenhuis (1983).

Based on this solution a computerprogram is available from S. Prahl (1986).

Appendix C.

Opening angle for two pinholes c and d at distance l.

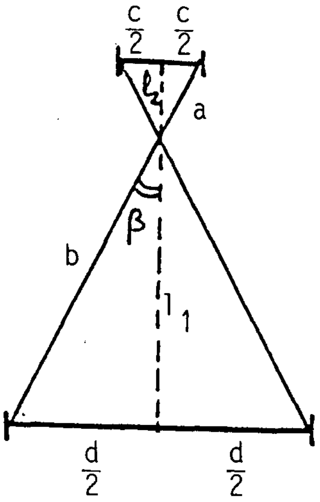

Fig. C.1

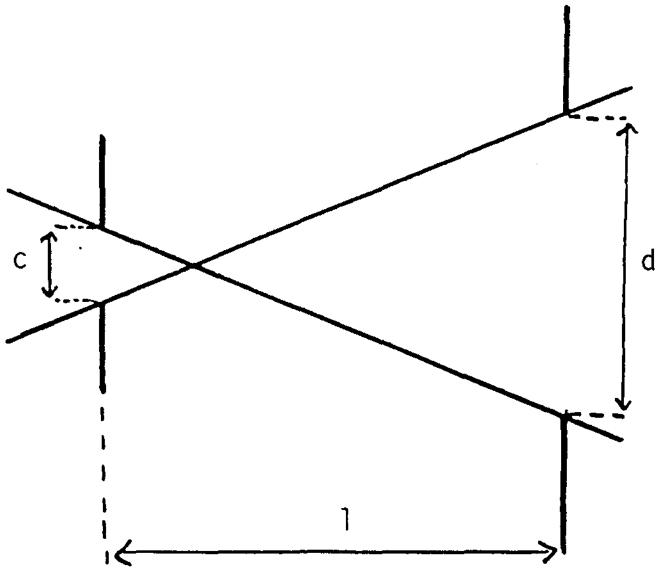

Fig. C.2

In fig. C.1 is

$$\frac{a}{b} = \frac{c}{d} \Rightarrow \quad b = a \cdot \frac{d}{c} \tag{C.1}$$

and

$$\sin\beta = \frac{\frac{1}{2}c}{a} \Rightarrow a = \frac{c}{2\sin\beta} \tag{C.2}$$

$$l_2 = \sqrt{a^2 - \tfrac{1}{4}c^2} \quad \text{and } l_1 = \sqrt{b^2 - \tfrac{1}{4}d^2}$$

$$= \sqrt{a^2 \frac{d^2}{c^2} - \tfrac{1}{4}d^2}$$

$$= \frac{d}{c}\sqrt{a^2 - \tfrac{1}{4}c^2} \tag{C.3}$$

thus

$$l = l_1 + l_2 = \left(1 + \frac{d}{c}\right) \sqrt{a^2 - \tfrac{1}{4} c^2} \tag{C.4}$$

$$= \frac{c+d}{2c} \sqrt{\frac{c^2}{\sin^2\beta} - c^2}$$

$$= \frac{c+d}{2\sin\beta} \sqrt{1-\sin^2\beta} \qquad = \frac{c+d}{2\tan\beta}$$

thus

$$\boxed{\tan\beta = \frac{c+d}{2l}} \tag{C.5}$$

LITERATURE.

1. Berns MW, Wilson M, Rentzepis P, Burns R, Wile A. Cell Biology of Hematoporphyrin Derivative (HpD). Lasers Surg. Med. (1983), vol. 2, 261-266.

2. Bown SG, Tralau CJ, Coleridge Smith PD, Akdemir D, Wieman TJ. Photodynamic Therapy with porphyrin and phthalocyanine sensitisation. Br. J. Cancer (1986), 54, 43.52.

3. Bruls WAG. Optical properties of Human Epidermis. Elinkwijk b.v., Utrecht, (1984), (dissertation).

4. Davison B. Neutron Transport Theory. Oxford: Clarendon Press, (1957).

5. Egan WG, Hilgeman TW. Optical Properties of Inhomogeneous Materials. Academic, New York, (1979).

6. Gemert MJC van, Schets GACM, Bishop MS, Cheong WF, Welch AJ. Optics of tissues in a multi-layer slab geometry. Lasers Life Sci., 2 (1), (1987), 1-18.

7. Gemert MJC van, Boon TA. Toepassingen van lasers in de geneeskunde. Samsom Stafleu, Alphen a/d Rijn, (1987).

8. Groenhuis RAJ, Ferwerda HA, Ten Bosch JJ. Scattering and absorption of turbid materials determined from reflection measurements I and II. Appl. Opt., vol. 22, (1983), 2456-2467.

9. Hulst HC v.d. Multiple Light scattering. vol. 1 and 2, Academic Press, New Yrok, (1980).

10. Ishimaru, A. Wave propagation in Random Meda, vol. 1, Academic Press, New York, (1978).

11. Keyzer M. Distributions of low-energy photons in highly scattering media. Faculty of Mathematics, Delft University of Technology, The Netherlands, (1986), (M.S. Thesis).

12. Prahl S. Multiple light scattering, finite diameter solution, (1986), (private communication).

13. Marijnissen JPA, Star WM. Quantitative light dosimetry in vitro and in vivo. Lasers Med. Sci., vol. 2, 235-242, (1987).

14. Profio AE. Laser excited fluorescence of hematoporphyrin dervative for diagnosis of cancer. IEEE J. Quant.Electr., vol. QE-20, no. 12, 1502-1507.

15. Reynolds LO. Optical diffuse reflectance and transmittance. University of Washington, (dissertation), (1975).

16. Reynolds LO, Johnson C, Ishimaru A. Diffuse reflectance from a finite

blood medium. Appl.Opt., vol. 15, no. 9, 2059-2067, (1976).

17. Salcman M. Survival in glioblastoma: Historical perspective. Neurosurgery, vol. 7, 435-439, (1980).

18. Sandeman DR. Photodynamic Therapy in the management of malignant gliomas: a review. Lasers Med. Sci., vol. 1, 163-174, (1986).

19. Splinter R. Light distribution in tissue. Eindhoven University of Technology, Faculty of Physics, The Netherlands, (1987), (M.S. Thesis).

20. Star WM, Marijnissen JPA, Gemert MJC van. Light dosimetry: Status and Prospects. J. Photochem.Photobiol., b Biology, no. 1, 149-167, (1987).

21. Star WM, Marijnissen JPA, Gemert MJC van. Light dosimetry in optical phantoms and in tissues: multiple flux and transport theory, Part I, in press in Phys.Med.Biol., (1988).

22. Star WM, Marijnissen JPA, Berg-Blok AE vd, Treurniet-Donker AD, Reinhold HS. Fotodynamische therapie van maligne tumoren. Klinische Fysica, (1985), 80-88.

23. Svaasand LO, Ellingsen R. Optical properties of Human Brain. Photochem. Photobiol., vol. 38, no. 3, 293-299, (1983).

24. Svaasand LO, Ellingsen R. Optical penetration in Human Intracranial Tumours. Photochem. Photobiol., vol. 41, no. 1, 73-76, (1985).

25. Weishaupt KR, Gomer CJ, Dougherty TJ. Identification of singlet oxygen as the cytotoxic agent in photo-inactivation of a murine tumour. Cancer Res., 36, 2326, (1976).

26. Wharen RE, Anderson RE, Laws ER. Quantitation of Hematoporphyrin Derivative in Human gliomas etc. Neurosurgery, vol. 12, no. 4, 446-450, (1986).

27. Wilson BC, Muller PJ, Yanch JC. Instrumentation and light dosimetry for intra-operative photodynamic therapy of malignant brain tumours. Phys. Med. Biol., vol. 31, no. 2, 125-133, (1986).

28. Wilson BC, Muller PJ. An up-date on the penetration depth of 630 nm light in normal and malignant human brain tissue in vivo. Phys.Med.Biol., vol. 31, no. 11, 1295-1297, (1986).

29. Wilson BC, Patterson MS, Flock ST. Indirect versus direct techniques for the measurement of the optical properties of tissues. Photochem.Photobiol., vol. 46, 601-608, (1987).

C.J.M. Moes

Bijlage

- In de tabellen II.1 , II.2, II.4 en II.5 staan afgeronde getallen ; gerekend is steeds met meerdere getallen achter de komma .

- In eq. II.3.14 moet staan $\mu_a = (5.2 \pm 1.5) \times 10^{-5}\ \mathrm{mm}^{-1}\mathrm{ml}^{-1}\ \mathrm{l}$

- In Table II.2 moet staan 0.0111 mm^{-1} i.p.v. 0.0113 mm^{-1} op regel 1
  en 0.1027 mm^{-1} i.p.v. 0.0526 mm^{-1} op regel 4

- In table II.4 moet staan 0.0065 mm^{-1} i.p.v. 0.065 mm^{-1} op regel 2
  en 0.113 mm^{-1} i.p.v. 0.114 mm^{-1} op regel 3

- In par. II.3,blz. 38 is in het iteratie-proces ter bepaling van de gecorrigeerde g*-waarde feitelijk één iteratie-stap uitgevoerd. Bij volledige uitvoering van het iteratie-proces blijken vier iteratie-stappen èen correcte waarde op te leveren voor $\hat{g}^*$. Het uiteindelijke resultaat voor g* wijkt daardoor iets af en we vinden:

$$\hat{g}^* = 0.71 \pm 0.03 \qquad \text{(II.3.15)}$$

- Dezelfde argumenten m.b.t. het iteratie-proces, zoals hierboven beschreven gelden uiteraard voor par. II.4, blz. 42 . Na vier iteratie-stappen vinden we voor de correcte g* :

$$\hat{g}^* = 0.71 \pm 0.03 \qquad \text{(II.4.4)}$$

hetgeen in overeenstemming is met het eerste resultaat .

- Als gevolg van dit iteratie-proces worden de getallen in tabellen nu :
  in tabel II.3 moet staan 5.6×10^{-5} i.p.v. 5×10^{-5} voor μ_{ao} op regel 4
  en 0.71 i.p.v. 0.70 voor g op regel 4
  in tabel II.6 moet staan 5.2×10^{-5} i.p.v. 5×10^{-5} voor μ_{ao} op regel 5
  en 0.71 i.p.v. 0.70 voor g op regel 1

- Eq. I.2.5 t/m eq. I.2.7 moet zijn :

$$b_n = \tfrac{1}{2} \int_{-1}^{1} S(\cos\theta)P_n(\cos\theta)\,d(\cos\theta) \qquad (I.2.5)$$

Normalisation requires that the integral of $S(\cos\theta)$ over all directions equals a , so

$$b_0 = \tfrac{1}{2} \int_{-1}^{1} S(\cos\theta)\,d(\cos\theta) = a \qquad (I.2.6)$$

because $P_0 = 1$, and because $P_1(\cos\theta) = \cos\theta$ we obtain for b_1 :

$$b_1 = \tfrac{1}{2} \int_{-1}^{1} S(\cos\theta)\cos\theta\ d(\cos\theta) = ag \qquad (I.2.7)$$

Thus b_1 is the mean cosine of the scattering angle and equals ag , where g is usually called the asymmetry parameter (v.d. Hulst, 1980) .